

Generated using the official AMS L<sup>A</sup>T<sub>E</sub>X template v6.1. This work has been submitted for publication. Copyright in this work may be transferred without further notice, and this version may no longer be accessible. This content has not been peer reviewed.

## An Analytic Model for the Clear-Sky Longwave Feedback

Daniel D.B. Koll<sup>a</sup>, Nadir Jeevanjee<sup>b</sup>, Nicholas J. Lutsko<sup>c</sup>

<sup>a</sup> *Laboratory for Climate and Ocean-Atmosphere Studies, Dept. of Atmospheric and Oceanic Sciences; Peking University; Beijing; China*

<sup>b</sup> *Geophysical Fluid Dynamics Laboratory; Princeton, NJ; USA*

<sup>c</sup> *Scripps Institution of Oceanography; La Jolla, CA; USA*



*Corresponding author:* Daniel D.B. Koll, [dkoll@pku.edu.cn](mailto:dkoll@pku.edu.cn)

1

**Early Online Release:** This preliminary version has been accepted for publication in *Journal of the Atmospheric Sciences*, may be fully cited, and has been assigned DOI 10.1175/JAS-D-22-0178.1. The final typeset copyedited article will replace the EOR at the above DOI when it is published.

ABSTRACT: Climate models and observations robustly agree that Earth's clear-sky longwave feedback has a value of about  $-2 \text{ W m}^{-2} \text{ K}^{-1}$ , suggesting that this feedback can be estimated from first principles. In this study, we derive an analytic model for Earth's clear-sky longwave feedback. Our approach uses a novel spectral decomposition that splits the feedback into four components: a surface Planck feedback, and three atmospheric feedbacks from  $\text{CO}_2$ ,  $\text{H}_2\text{O}$ , and the  $\text{H}_2\text{O}$  continuum. We obtain analytic expressions for each of these terms, and the model can also be framed in terms of Simpson's Law and deviations therefrom. We validate the model by comparing it against line-by-line radiative transfer calculations across a wide range of climates. Additionally, the model qualitatively matches the spatial feedback maps of a comprehensive climate model. For present-day Earth, our analysis shows that the clear-sky longwave feedback is dominated by the surface in the global mean and in the dry subtropics; meanwhile, atmospheric feedbacks from  $\text{CO}_2$  and  $\text{H}_2\text{O}$  become important in the inner tropics. Together, these results show that a spectral view of Earth's clear-sky longwave feedback elucidates not only its global-mean magnitude, but also its spatial pattern and its state-dependence across past and future climates.

**SIGNIFICANCE STATEMENT:** The climate feedback determines how much our planet warms due to changes in radiative forcing. For more than 50 years scientists have been predicting this feedback using complex numerical models. Except for cloud effects the numerical models largely agree, lending confidence to global warming predictions, but nobody has yet derived the feedback from simpler considerations. We show that Earth's clearsky longwave feedback can be estimated using only pen and paper. Our results confirm that numerical climate models get the right number for the right reasons, and allow us to explain regional and state variations of Earth's climate feedback. These variations are difficult to understand solely from numerical models but are crucial for past and future climates.

## 1. Introduction

Earth's climate sensitivity is a crucial factor in understanding and predicting climate change. While uncertainty in climate sensitivity is dominated by cloud feedbacks, the magnitude of climate sensitivity is largely set by the clear-sky longwave feedback,  $\lambda_{LW}$ . Early studies estimated  $\lambda_{LW}$  to be  $-2.2$ - $2.3 \text{ W m}^{-2} \text{ K}^{-1}$  (Manabe and Wetherald 1967; Budyko 1969). These estimates were impressively close to the current best estimates from climate models and observations, which agree on a fairly narrow range for  $\lambda_{LW}$  of about  $-1.8$  to  $-2.2 \text{ W m}^{-2} \text{ K}^{-1}$  (Andrews et al. 2012; Chung et al. 2010; Kluft et al. 2019; Zhang et al. 2020; Zelinka et al. 2020). By contrast, the recent Sherwood et al. (2020) assessment estimated the total cloud feedback to be both smaller in magnitude and less certain at  $+0.45 \pm 0.33 \text{ W m}^{-2} \text{ K}^{-1}$ .

The robustness of the clear-sky longwave feedback suggests that one should be able to understand and describe its governing physics in fairly simple form. A simple model for  $\lambda_{LW}$  would provide definitive support for the value of  $-2 \text{ W m}^{-2} \text{ K}^{-1}$  derived from observations and climate models. It would also allow us to understand the state-dependence of  $\lambda_{LW}$ : at warm enough temperatures Earth's atmosphere transitions to a runaway state, in which  $\lambda_{LW}$  becomes zero or even changes sign, but it is unclear how  $\lambda_{LW}$  varies between today's value and the runaway limit. Similarly, there is a long-standing interest in using paleoclimate proxies to constrain present-day climate sensitivity (Tierney et al. 2020), but this effort suffers from uncertainty regarding the state-dependence of climate feedbacks (Meraner et al. 2013; Bloch-Johnson et al. 2015). Finally, geographic variation in feedbacks and their importance for the so-called pattern effect is an ongoing topic of research

(Armour et al. 2013; Andrews et al. 2015, 2018) , but if  $\lambda_{LW}$  has state-dependence then that dependence should also influence the spatial pattern of  $\lambda_{LW}$ . For example, if the global-mean  $\lambda_{LW}$  was different in past climates due to changes in the global-mean surface temperature, then present-day  $\lambda_{LW}$  should show regional variation due to Earth’s surface temperature pattern, suggesting a close link between state-dependence and spatial-dependence of  $\lambda_{LW}$ .

One of the earliest models for  $\lambda_{LW}$  was proposed by Simpson (1928a), who found that an atmosphere that is optically thick due to water vapor would have a clear-sky longwave feedback that is approximately zero, suggesting Earth should be in a runaway greenhouse. Although this early model was abandoned by Simpson (1928b) as being overly simplistic, Ingram (2010) resolved the Simpsonian “paradox” by separating out the parts of Earth’s outgoing radiation spectrum that are optically thick due to water vapor (and for which  $\lambda_{LW}$  is approximately zero) from the optically thin “window” region. Koll and Cronin (2018) subsequently quantified Ingram’s argument: using fixed relative humidity (RH), single-column calculations they argued that for present-day Earth the clear-sky longwave feedback is dominated by the surface:

$$\lambda_{LW} \approx \lambda_{\text{surf}}. \quad (1)$$

Here  $\lambda_{\text{surf}}$  is the surface Planck feedback, which is smaller than a blackbody’s feedback because greenhouse gases block the surface’s emission outside the spectral window. Meanwhile, the atmosphere itself contributes less to  $\lambda_{LW}$  in the present climate, and so to first order its contribution can be ignored. It follows that atmospheric feedback terms which are often the focus of climate model or observational analyses – the atmospheric component of the Planck feedback, the lapse-rate feedback and the water vapor feedback – roughly cancel (Koll and Cronin 2018; Jeevanjee et al. 2021a).

The match between  $\lambda_{LW}$  and the surface Planck feedback  $\lambda_{\text{surf}}$  in Equation 1 is not exact, however. Follow-up work found that  $\lambda_{\text{surf}}$  only accounts for 50-90% of  $\lambda_{LW}$  in different regions, with about 60% in the global mean (Raghuraman et al. 2019; Feng et al. 2022), implying a gap in the argument of Koll and Cronin (2018). Similarly, Seeley and Jeevanjee (2021) showed that in hot, high-CO<sub>2</sub> climates  $\lambda_{\text{surf}}$  becomes negligible yet  $\lambda_{LW}$  does not go to zero. As the surface warms the atmosphere is still able to increase its emission to space in spectral regions that are dominated by CO<sub>2</sub>. This emission mostly comes from the upper atmosphere, and gives rise to a

spectral CO<sub>2</sub> “radiator fin” feedback. The existence of a CO<sub>2</sub> feedback means  $\lambda_{LW}$  must depend on CO<sub>2</sub> concentration, and thus must have CO<sub>2</sub> state-dependence. Moreover, the CO<sub>2</sub> feedback has to depend on the atmospheric lapse rate: if the atmosphere was isothermal with zero lapse rate, CO<sub>2</sub>’s forcing and feedback would both have to be zero, in line with previous work which tried to quantify the dependence of CO<sub>2</sub> forcing on the lapse rate (Huang and Bani Shahabadi 2014; Dufresne et al. 2020), even if the details of the forcing mechanism are still disputed (Seeley 2018; Romps et al. 2022). So while the “surface-only” feedback picture from Koll and Cronin (2018) gives a reasonable first-order approximation to  $\lambda_{LW}$ , more terms are needed to describe  $\lambda_{LW}$  quantitatively.

In this study, we aim to derive a simple model of Earth’s feedback that can quantitatively capture the magnitude of  $\lambda_{LW}$  as well as its state-dependence and regional variations. The model decomposes  $\lambda_{LW}$  into the surface Planck feedback ( $\lambda_{surf}$ ) plus three atmospheric terms: a CO<sub>2</sub> band feedback ( $\lambda_{CO_2}$ ), a non-Simpsonian water vapor band feedback ( $\lambda_{H_2O}$ ), and a destabilizing water vapor continuum feedback ( $\lambda_{cnt}$ ). Although these feedbacks are less familiar, they represent the different substances through which Earth gives longwave radiation off to space, and how each substance changes its emission under surface warming. As shown below, expressions can be derived for each spectral feedback term starting from the basic equations of radiative transfer. These expressions can be interpreted as a global-mean model for  $\lambda_{LW}$  or in terms of local feedbacks (Feldl and Roe 2013; Armour et al. 2013; Bloch-Johnson et al. 2020). That is, each atmospheric column is treated as an isolated 1D system whose longwave feedback depends on its local surface temperature. We validate the model (and the utility of the spectral decomposition) by comparing it against calculations with a line-by-line radiation code.

Our model of  $\lambda_{LW}$  is based on spectroscopic thinking and hence represents a different perspective than the conventional decomposition which breaks the clear-sky longwave feedback into Planck, Lapse-rate and Water Vapor feedbacks (e.g., Soden et al. 2008; Sherwood et al. 2020; Zelinka et al. 2020). The conventional decomposition has been an important tool for understanding  $\lambda_{LW}$  and for diagnosing the physics governing outgoing longwave radiation in climate models. However, it also obscures large cancellations between the atmospheric part of the Planck feedback, the Lapse-rate feedback and the Water Vapor feedback (Held and Shell 2012; Koll and Cronin 2018; Jeevanjee et al. 2021a). By obscuring these cancellations the conventional decomposition can give a false

impression of the uncertainty of climate models. The same cancellations also make it difficult to understand the state-dependence of  $\lambda_{LW}$  – Planck, Lapse-rate and Water Vapor feedbacks all increase in a warmer climate, but it is far from obvious how these changes add up to affect  $\lambda_{LW}$  (Meraner et al. 2013). Building on previous discussions of spectral feedbacks (e.g., Huang et al. 2010, 2014; Koll and Cronin 2018; Pan and Huang 2018; Seeley and Jeevanjee 2021; Jeevanjee et al. 2021a; Kluft et al. 2021; Feng et al. 2022), our goal in this paper is to show that the issues that arise in the conventional decomposition can be resolved by viewing  $\lambda_{LW}$  in terms of its spectral components instead.

The layout of the rest of this paper is as follows. Section 2 discusses several preliminaries which are necessary for the main derivations: an idealized Clausius-Clapeyron relation, an analytic approximation for moist lapse rates and idealized band models for H<sub>2</sub>O and CO<sub>2</sub> spectroscopy. Section 3 lays out our spectral framework and introduces the emission-level approximation, our spectral decomposition of  $\lambda_{LW}$  and a description of the numerical line-by-line calculations. Section 4 derives analytic expressions for Earth’s emission temperature in different parts of the spectrum, which are then used in Section 5 to derive analytic feedbacks. Our expressions compare favorably against the state-dependence of  $\lambda_{LW}$  from line-by-line calculations. Next, Section 6 uses these results to understand the spatial pattern of Earth’s clear-sky longwave feedback. We generate global maps of Earth’s clear-sky longwave feedback using a radiative kernel and climate model data. We then show that our analytic expressions recover qualitatively similar feedback patterns, which implies that the spatial pattern of  $\lambda_{LW}$  can be largely understood using our analytic model. Breaking  $\lambda_{LW}$  up into surface versus atmospheric terms, we find that the surface dominates  $\lambda_{LW}$  in the global-mean as well as in the dry subtropics, with a spatial pattern set by the pattern of atmospheric relative humidity, while atmospheric feedbacks become significant in the inner tropics, with spatial patterns that are set by regional lapse rate changes under warming. The manuscript closes in Section 7 with a conclusion and broader discussion of the results.

## 2. Preliminaries

Our goal is to derive the longwave feedback of a cloud-free vertical column of atmosphere. The column’s state can be specified using five parameters:  $T_s$ ,  $\gamma_r$ , RH,  $q_{CO_2}$  and  $T_{strat}$ . Here  $T_s$  is the surface temperature,  $\gamma_r \equiv d\ln T/d\ln p$  is the temperature lapse rate, RH is the relative humidity,

$q_{\text{CO}_2}$  is the CO<sub>2</sub> mass mixing ratio and  $T_{\text{strat}}$  is the stratospheric temperature. We idealize the state of the column by treating  $\gamma_{\text{lr}}$ , RH, and  $q_{\text{CO}_2}$  as vertically uniform; all are defined more precisely below. Similarly, we approximate the stratosphere as isothermal.

*a. Clausius-Clapeyron*

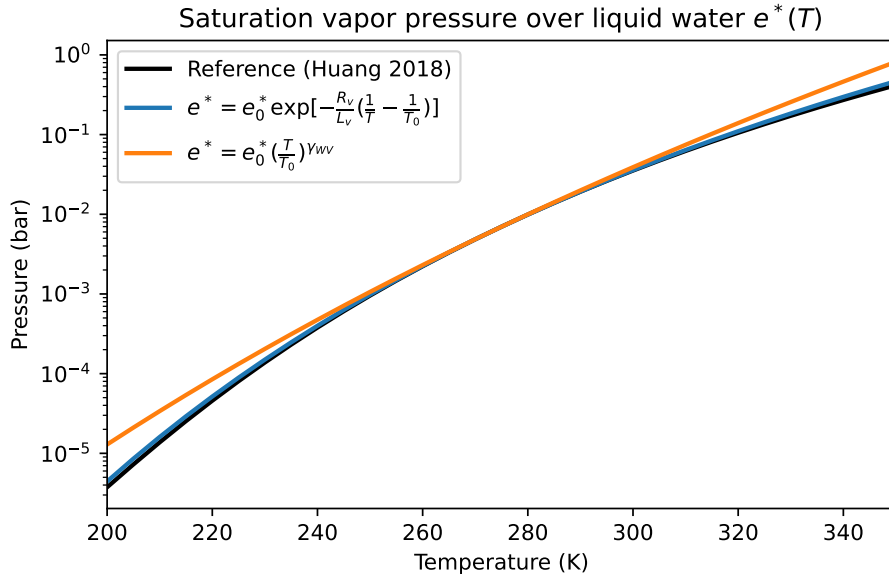


FIG. 1. Different approximations to the Clausius-Clapeyron relation. Black: fit based on experimental data (Huang 2018). Blue: the commonly-used quasi-exponential approximation. Orange: the power law approximation used in this work. The saturation vapor pressure is with respect to liquid water. In this plot  $(T_0, e_0^*)$  are set equal to the triple point values of H<sub>2</sub>O, so  $\gamma_{\text{wv}} = 19.8$ .

The Clausius-Clapeyron relation governs the temperature-dependence of the saturation vapor pressure  $e^*(T)$  and is an essential element of our analytic model. The Clausius-Clapeyron relation is often solved by ignoring the temperature-dependence of the latent heat of vaporization,  $d \ln e^* / d \ln T = L_v(T) / (R_v T) \approx L_v(T_0) / (R_v T)$ , which leads to the quasi-exponential approximation

$$e^* \approx e_0^*(T_0) \exp \left[ -\frac{L_v(T_0)}{R_v} \left( \frac{1}{T} - \frac{1}{T_0} \right) \right]. \quad (2)$$

This quasi-exponential form does not lead to closed-form analytic expressions in the equations of radiative transfer, however, so we require a simpler form of the Clausius-Clapeyron rela-

tion. We obtain this by approximating the Clausius-Clapeyron relation further as  $d \ln e^* / d \ln T = L_v(T)/(R_v T) \approx \text{const}$ , which leads to a simple power law between temperature and saturation vapor pressure (Koll and Cronin 2019),

$$e^* \approx e_0^*(T_0) \left( \frac{T}{T_0} \right)^{\gamma_{\text{wv}}}, \quad (3)$$

where

$$\gamma_{\text{wv}} \equiv \frac{L_v(T_0)}{R_v T_0}. \quad (4)$$

Here  $T_0$  is an arbitrary reference temperature around which we are approximating the saturation vapor pressure as a power law. We emphasize that  $T_0$  is effectively a thermodynamic constant and does not change with surface warming. The non-dimensional power law exponent is large and reflects the steep rise of  $e^*$  with temperature; at Earth-like temperatures,  $\gamma_{\text{wv}} \approx 20$ . The fractional increase in saturation vapor pressure per unit warming is  $d \ln e^* / dT = \gamma_{\text{wv}} / T \sim 7\% / \text{K}$ , in line with other Clausius-Clapeyron approximations.

Figure 1 compares the approximations in Equations 2 and 3 against a fit based on experimental data (Huang 2018). Considering that a typical tropical atmospheric column spans the vertical temperature range 200 – 300 K, the quasi-exponential approximation is very accurate, whereas our power law approximation only matches to roughly a factor of two. Nevertheless, as shown below, this accuracy is good enough to match numerical calculations.

### *b. Bulk moist lapse rate*

The vertical temperature-pressure profile of an atmospheric column can be specified via the lapse-rate exponent

$$\gamma_{\text{lr}} = d \ln T / d \ln p, \quad (5)$$

where  $p$  is pressure. For a dry adiabat the lapse rate exponent is vertically uniform,  $\gamma_{\text{lr}} = R_d / c_p \approx 2/7$ . For a moist atmosphere  $\gamma_{\text{lr}}$  varies both as a function of temperature and pressure, but due to the latent heat release in a convecting parcel it is generally smaller than the dry lapse rate:  $\gamma_{\text{lr}} \leq R_d / c_p$ .

In order to obtain analytically tractable expressions we would like to treat  $\gamma_{\text{lr}}$  as constant in the vertical even for a moist column, so we diagnose a bulk  $\gamma_{\text{lr}}$  using the surface and tropopause values



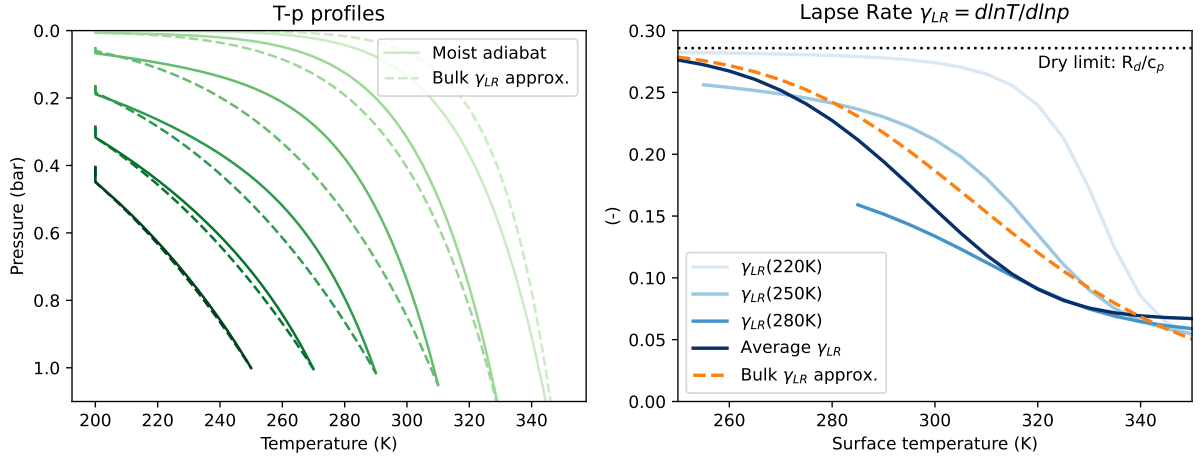


FIG. 2. Moist adiabatic lapse rates versus our analytic approximation. Left: Pressure-Temperature profiles following a moist adiabat (solid) and following the bulk lapse rate approximation (dashed). Right: adiabatic lapse rate  $\gamma_{lr}$  numerically computed at three fixed temperature levels inside the troposphere (light blue), compared with the bulk approximation in Equation (9) (orange). Note that  $\gamma_{lr}(T)$  is undefined if  $T$  is larger than the surface temperature  $T_s$ . The average  $\gamma_{lr}$  (dark blue) is a mass-weighted mean of all numerical lapse rates inside the troposphere,  $1/(p_s - p_{tp}) \times \int_{p_{tp}}^{p_s} \gamma_{lr} dp$ .

of  $(T, p)$ :

$$\gamma_{lr} \approx \frac{\ln(T_{tp}/T_s)}{\ln(p_{tp}/p_s)}. \quad (6)$$

Assuming that the tropopause temperature stays constant in response to surface temperature changes, in accord with the FAT/FiTt hypothesis (Hartmann and Larson 2002; Seeley et al. 2019), then all that is needed is an expression for how  $p_{tp}$  depends on  $T_s$ . We can derive such an expression by first obtaining an expression for the tropopause height  $z_{tp}$ , following Romps (2016). From MSE conservation along an undilute moist adiabat between the surface and tropopause,

$$z_{tp} \approx \frac{1}{g} (c_p(T_s - T_{tp}) + L_v q_s^*), \quad (7)$$

where  $q_s^*$  is the mass mixing ratio of water at saturation,  $q^*$ , evaluated at the surface and we neglect  $q^*$  at the tropopause.  $p_{tp}$  can then be obtained as

$$p_{tp} = p_s e^{-z_{tp}/H}, \quad (8)$$

where  $H$  is the scale height of pressure ( $= \frac{R_d T_{av}}{g}$ ) and  $T_{av} \equiv (T_s + T_{tp})/2$ . Plugging this into (6) yields

$$\gamma_{lr} \approx \frac{R_d T_{av} \ln(T_s/T_{tp})}{c_p (T_s - T_{tp}) + L_v q_s^*}. \quad (9)$$

One can show that Equation 9 correctly reduces to the dry lapse rate  $\gamma_{lr} = R_d/c_p$  by setting  $q_s^* = 0$  and series expanding the logarithm, assuming  $T_s - T_{tp} \ll T_{tp}$ . In practice the latter assumption is not strictly true but the resulting deviation from the dry adiabat is small even for a 100 K difference between surface and tropopause.

According to the bulk approximation,  $\gamma_{lr}$  is constant in the vertical and varies only in response to climatic changes (e.g., changes in surface temperature). One can then integrate Equation 5 to solve for the column's temperature-pressure profile. This leads to a power law similar to a dry adiabat,

$$T(p) = T_s \left( \frac{p}{p_s} \right)^{\gamma_{lr}(T_s)}, \quad (10)$$

where the only difference to a dry adiabat is that now the lapse rate depends on surface temperature.

Figure 2 (left) compares profiles based on Equation 10 to moist adiabatic profiles. The moist adiabats are obtained by numerically integrating a generalized form of the moist adiabat which does not approximate water vapor as a dilute substance and thus remains valid at high temperatures (Ding and Pierrehumbert 2016). In all cases, the tropopause temperature is assumed to be fixed and equal to  $T_{strat} = 200$  K. The analytic profiles given by Equation 10 produce a reasonable fit to the moist adiabats, though at surface temperatures below 340 K they produce slightly colder tropospheres. The tropopause pressure is accurately reproduced, as the analytic profiles always reach the tropopause at roughly the same point as the moist adiabats.

Figure 2 (right) compares the  $T_s$ -dependence of  $\gamma_{lr}$ . First, the moist adiabatic  $T(p)$  profiles shown in Figure 2 (left) are used to numerically compute  $\gamma_{LR}$  at individual levels of the troposphere. Because our bulk expression for  $\gamma_{LR}$  only depends on temperature, and not pressure, the moist adiabatic values of  $\gamma_{LR}$  are similarly shown at fixed temperature levels. Additionally, for each adiabatic  $T(p)$  profile we compute the average moist lapse rate using a mass-weighted mean,  $1/(p_s - p_{tp}) \times \int_{p_{tp}}^{p_s} \gamma_{lr} dp$ . Figure 2 shows that our analytic approximation captures the  $T_s$ -dependence of the average moist lapse rate relatively well, though this general agreement can obscure significant differences at individual levels. For example, our analytic approximation of

$\gamma_{\text{r}}$  deviates by more than a factor of two from the moist-adiabatic  $\gamma_{\text{r}}$  at the  $T = 220$  K level. We will show below that these details of atmospheric lapse rates do not have a major impact on Earth's longwave feedback at low surface temperatures, but they become increasingly important above  $\sim 300$  K.

### c. $\text{H}_2\text{O}$ and $\text{CO}_2$ spectroscopy

The third ingredient for our derivations is a model of  $\text{H}_2\text{O}$  and  $\text{CO}_2$  spectroscopy. We follow previous studies and model the absorption cross-sections of  $\text{H}_2\text{O}$  and  $\text{CO}_2$  as log-linear band shapes. Despite the simplicity of these models, they are able to explain numerous features of Earth's climate, including the logarithmic nature of  $\text{CO}_2$  forcing, the temperature-dependence of Earth's surface feedback and the vertical structure of radiative cooling (Crisp et al. 1986; Pierrehumbert 2010; Wilson and Gea-Banacloche 2012; Koll and Cronin 2018; Jeevanjee and Fueglistaler 2020; Roms et al. 2022). Because we explore feedbacks over a wide range of temperatures, we additionally need to account for the  $\text{H}_2\text{O}$  continuum. We do so by approximating the continuum as a grey absorber.

For  $\text{CO}_2$ , the absorption cross-section is

$$\kappa_{\text{CO}_2} = \kappa_0 \left( \frac{p}{p_0} \right) \exp \left( - \frac{|\nu - \nu_0|}{l_\nu} \right), \quad (11)$$

where  $\kappa_0$  is the absorption cross-section in the center of the band,  $p_0$  is a reference pressure,  $\nu$  is wavenumber,  $\nu_0$  the wavenumber of the center of the band and  $l_\nu$  the decay rate of the absorption cross-section in wavenumber space. Previous work fit these parameters to the  $\text{CO}_2$  absorption spectrum at a reference pressure of  $p_0 = 0.1$  bar (Jeevanjee et al. 2021b). Because the choice of reference pressure is arbitrary, we here rescale the fits to the dry surface pressure in our calculations (i.e., the surface pressure excluding the contribution of water vapor),  $p_0 = 1$  bar. The resulting values are  $\kappa_0 = 500 \text{ m}^2/\text{kg}$ ,  $\nu_0 = 667.5 \text{ cm}^{-1}$  and  $l_\nu = 10.2 \text{ cm}^{-1}$ .

$\text{H}_2\text{O}$  band absorption can similarly be modeled using a log-linear shape, though one has to account for the fact that  $\text{H}_2\text{O}$  has two bands which are relevant for Earth's longwave feedback. The rotation band determines  $\text{H}_2\text{O}$  absorption at wavenumbers less than  $1000 \text{ cm}^{-1}$  and the vibration-rotation

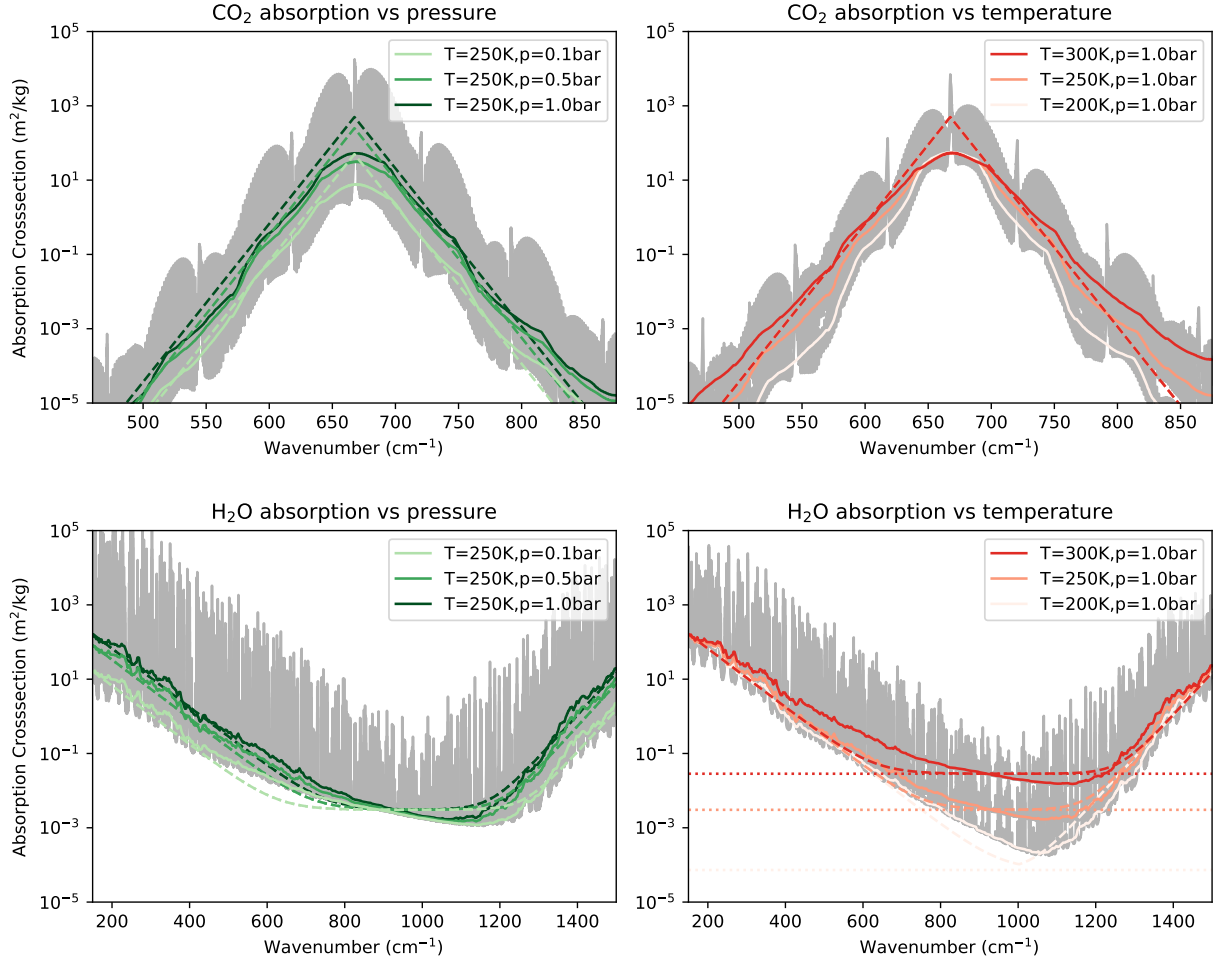


FIG. 3. Idealized band models compared against the absorption cross-sections of CO<sub>2</sub> (top row) and H<sub>2</sub>O (bottom). Grey envelopes show cross-sections computed at line-by-line spectral resolution, solid lines are the cross-sections smoothed by a median filter with width 25 cm<sup>-1</sup>. Dashed lines are the band models for CO<sub>2</sub> and H<sub>2</sub>O bands (the sum of line and continuum absorption), while dotted lines show the grey H<sub>2</sub>O continuum model only. The CO<sub>2</sub> band model assumes the absorption cross-section is independent of temperature, so only one dashed line is shown in the top right.

band at wavenumbers larger than 1000 cm<sup>-1</sup>. We model these two bands as

$$\kappa_{\text{H}_2\text{O},\text{line}} = \left(\frac{p}{p_0}\right) \max \left[ \kappa_{\text{rot}} \exp\left(-\frac{|\nu - \nu_{\text{rot}}|}{l_{\text{rot}}}\right), \kappa_{\nu-\tau} \exp\left(-\frac{|\nu - \nu_{\nu-\tau}|}{l_{\nu-\tau}}\right) \right]. \quad (12)$$

The first term in the  $\max(\dots)$  expression represents the rotation band, which dominates at low wavenumbers, while the second term represents the vibration-rotation band at high wavenumbers. The factor  $p/p_0$  in front of both H<sub>2</sub>O and CO<sub>2</sub> cross-sections reflects pressure broadening: under present-Earth conditions CO<sub>2</sub> and H<sub>2</sub>O absorption lines become wider due to collisions of those molecules with the background air (N<sub>2</sub> or O<sub>2</sub>). This has the overall effect that both gases become more efficient absorbers at higher pressure.

In contrast to the CO<sub>2</sub> and H<sub>2</sub>O bands, the H<sub>2</sub>O continuum is dominated by self broadening so the continuum cross-section is independent of pressure and instead scales as  $\propto e = \text{RH}e^*$ . Although continuum absorption is not uniform with respect to wavenumber, its spectral dependence is significantly weaker than the H<sub>2</sub>O or CO<sub>2</sub> bands. We therefore approximate the continuum as a grey absorber and write

$$\kappa_{\text{H}_2\text{O},\text{cnt}} = \kappa_{\text{cnt}} \text{RH} \frac{e^*(T)}{e_0^*} \left( \frac{T}{T_0} \right)^{-a}, \quad (13)$$

where the dimensionless exponent  $a$  captures the direct temperature-dependence which acts to weaken the continuum (Pierrehumbert 2010). The total H<sub>2</sub>O cross-section is the sum of line and continuum absorption,  $\kappa_{\text{H}_2\text{O}} = \kappa_{\text{H}_2\text{O},\text{line}} + \kappa_{\text{H}_2\text{O},\text{cnt}}$ . Because the line opacity decreases exponentially away from H<sub>2</sub>O band centers, the total opacity becomes largely dominated by the continuum in the window region around  $\sim 1000 \text{ cm}^{-1}$ .

Our model of H<sub>2</sub>O spectroscopy has eight parameters:  $\kappa_{\text{rot}}$ ,  $l_{\text{rot}}$ ,  $\nu_{\text{rot}}$ ,  $\kappa_{\text{v-r}}$ ,  $l_{\text{v-r}}$ ,  $\nu_{\text{v-r}}$ ,  $\kappa_{\text{cnt}}$ ,  $a$ . We set  $\nu_{\text{rot}} = 150 \text{ cm}^{-1}$  and  $\nu_{\text{v-r}} = 1500 \text{ cm}^{-1}$ , and fit the remaining parameters using the median-smoothed H<sub>2</sub>O cross-sections shown in Figure 3 across the wavenumber range  $150 \text{ cm}^{-1} \leq \nu \leq 1500 \text{ cm}^{-1}$ . The results are sensitive to the smoothing procedure, that is whether one uses a geometric mean or a median. Because the average transmission across a spectral band tends to be dominated by the most optically thin frequencies (Pierrehumbert 2010), we use a median filter. To perform the fits we use the non-linear least-squares algorithm `scipy.optimize.curve_fit`, with a reference temperature of  $T_0=300 \text{ K}$ . We first fit the parameters  $\kappa_{\text{rot}}$ ,  $l_{\text{rot}}$ ,  $\kappa_{\text{v-r}}$ ,  $l_{\text{v-r}}$  to H<sub>2</sub>O line opacities only, and then use these parameters to fit  $\kappa_{\text{cnt}}$  and  $a$  to H<sub>2</sub>O cross-sections that include both line and continuum opacity. The resulting values are  $\kappa_{\text{rot}} = 165 \text{ m}^2/\text{kg}$ ,  $l_{\text{rot}} = 55 \text{ cm}^{-1}$ ,  $\kappa_{\text{v-r}} = 15 \text{ m}^2/\text{kg}$ ,  $l_{\text{v-r}} = 38 \text{ cm}^{-1}$ ,  $\kappa_{\text{cnt}} = 3 \times 10^{-3} \text{ m}^2/\text{kg}$  and  $a = 7$ , which broadly match the H<sub>2</sub>O fits

previously reported in Jeevanjee and Fueglistaler (2020). Table 1 summarizes the thermodynamic and spectral parameters used in this paper.

Figure 3 compares the idealized band models with line-by-line absorption cross-sections. Overall, the shape of the cross-sections is captured fairly well. The median CO<sub>2</sub> and H<sub>2</sub>O cross-sections scale linearly with total pressure, as expected for pressure-broadening. The increasing H<sub>2</sub>O absorption in response to warming around 1000 cm<sup>-1</sup> is also qualitatively captured by our grey continuum model, even though the H<sub>2</sub>O continuum itself is actually not grey.

Figure 3 (right plots) shows that the slopes of the CO<sub>2</sub> and H<sub>2</sub>O bands flatten as temperature increases, with roughly constant opacity in the band centers but increasing opacity in the band wings. This behavior is not captured by our simple models. Physically, absorption band slopes can depend on temperature due to the shifting population of different molecular excitation states. For example, the wings of the 667 cm<sup>-1</sup> CO<sub>2</sub> band consist of multiple smaller bands that correspond to transitions between excited states of CO<sub>2</sub> (so-called hot bands), while the center of the CO<sub>2</sub> band is dominated by transitions to/from the ground state of CO<sub>2</sub>. As temperature rises more CO<sub>2</sub> molecules leave the ground state and access excited states, which in turn preferentially increases the opacity in the wings of the CO<sub>2</sub> band. To keep our parameterizations simple, however, we do not attempt to model the temperature-dependence of the band slopes.

### 3. Spectral Framework

#### *a. The emission-level approximation*

To decompose the net longwave feedback into its spectral components we first need to consider the outgoing longwave flux (OLR) of a vertical column. At a spectral wavenumber  $\nu$ , the column's longwave flux varies vertically according to the monochromatic optical thickness  $\tau^*$  and the angle  $\cos(\theta)$  with which radiation propagates through the column. Assuming that the atmosphere's longwave radiation follows a known angular distribution, e.g., isotropic, these quantities can be combined into the vertical coordinate  $\tau = \tau^*/\cos(\bar{\theta})$ . Here  $\cos(\bar{\theta})$  describes the average angle of propagation, and  $\tau$  varies from  $\tau = 0$  at the TOA to  $\tau = \tau_{\text{surf}}$  at the surface (e.g. Pierrehumbert 2010). The column's OLR is then equal to

$$\text{OLR} = \int_0^\infty \pi B_\nu(T_s) e^{-\tau_{\text{surf}}} d\nu + \int_0^\infty \int_0^{\tau_{\text{surf}}} \pi B_\nu(T(\tau)) e^{-\tau} d\tau d\nu. \quad (14)$$

TABLE 1. List of parameters and, where applicable, assumed values.

Parameter name	Explanation	Assumed value
Thermodynamic parameters		
$T_0$	Reference temperature for saturation vapor pressure power-law	300 K
$\gamma_{\text{wv}}$	Exponent in saturation vapor pressure power-law	18
$\gamma_{\text{lr}}$	Exponent in bulk lapse rate temperature-pressure power-law	Computed using Eqn. 9 (Section 5), or derived from data (Section 6)
Spectral parameters		
$\cos(\bar{\theta})$	Inverse angular diffusivity factor	3/5
$p_0$	Reference pressure for absorption cross-sections	1 bar
$\kappa_0$	Absorption cross-section in center of CO <sub>2</sub> band	500 m <sup>2</sup> /kg
$\nu_0$	Wavenumber of the center of the CO <sub>2</sub> band	667.5 cm <sup>-1</sup>
$l_{\nu}$	Decay rate of the CO <sub>2</sub> absorption cross-section in wavenumber space	10.2 cm <sup>-1</sup>
$\kappa_{\text{rot}}$	Absorption cross-section in center of H <sub>2</sub> O rotation band	165 m <sup>2</sup> /kg
$\nu_{\text{rot}}$	Wavenumber of the center of the H <sub>2</sub> O rotation band	150 cm <sup>-1</sup>
$l_{\text{rot}}$	Decay rate of the H <sub>2</sub> O absorption cross-section in wavenumber space in the rotation band	55 cm <sup>-1</sup>
$\kappa_{\nu-r}$	Absorption cross-section in center of H <sub>2</sub> O vibration-rotation band	15 m <sup>2</sup> /kg
$\nu_{\nu-r}$	Wavenumber of the center of the H <sub>2</sub> O vibration-rotation band	1500 cm <sup>-1</sup>
$l_{\nu-r}$	Decay rate of the H <sub>2</sub> O absorption cross-section in wavenumber space in the vibration-rotation band	38 cm <sup>-1</sup>
$\kappa_{\text{rot}}$	Grey absorption cross-section of H <sub>2</sub> O continuum	$3 \times 10^{-3}$ m <sup>2</sup> /kg
$\alpha$	Exponent of H <sub>2</sub> O continuum temperature-dependence	7
Analytic model parameters		
$T_{\text{strat}}$	Stratospheric temperature	200 K
$c_{\text{surf}}$	Scaling constant for surface feedback	0.8 (bulk lapse rate)/0.8 (moist adiabat)
$c_{\text{H}_2\text{O}}$	Scaling constant for H <sub>2</sub> O band feedback	0.6 (bulk lapse rate)/1.0 (moist adiabat)
$c_{\text{cnt}}$	Scaling constant for H <sub>2</sub> O continuum feedback	0.4 (bulk lapse rate)/0.4 (moist adiabat)
$c_{\text{CO}_2}$	Scaling constant for CO <sub>2</sub> band feedback	0.7 (bulk lapse rate)/0.9 (moist adiabat)

The optical thicknesses  $\tau$  and  $\tau_{\text{surf}}$  are functions of  $\nu$ , so the order of integration cannot be switched. Physically, the first term corresponds to the surface's emission to space, while the second term corresponds to an integral of the emission coming from each vertical level in the atmosphere.

The emission-level or radiating-level approximation states that the atmosphere's emission to space (the second integral in Equation 14) originates from the vertical level at which optical thickness  $\tau$  is order unity. The intuition behind the emission-level approximation is that levels of the atmosphere for which  $\tau \ll 1$  are optically thin and do not contribute much to the TOA flux, while most emission from levels with  $\tau \gg 1$  is absorbed by the overlying atmosphere and so its contribution to the TOA flux is also small. The emission level has been defined at slightly different values of  $\tau$ , but all definitions agree on a value of order unity (Pierrehumbert 2010; Jeevanjee et al. 2021b). For simplicity, we define the emission level here as the level at which  $\tau = 1$ . The temperature at this level is then the emission level temperature,  $T_{\text{rad}} \equiv T(\tau = 1)$ , so

$$\text{OLR} \approx \int_0^{\infty} \pi B_{\nu}(T_s) e^{-\tau_{\text{surf}}} d\nu + \int_0^{\infty} \pi B_{\nu}(T_{\text{rad}}(\nu)) d\nu. \quad (15)$$

Given the emission-level approximation, the clear-sky longwave feedback is determined by how the surface emission and the atmospheric emission change in response to warming,

$$\begin{aligned}
 -\lambda_{LW} &= \frac{d\text{OLR}}{dT_s} \\
 &\approx \int_0^\infty \pi \frac{dB_\nu}{dT} \Big|_{T_s} e^{-\tau_{\text{surf}}} d\nu + \int_0^\infty \pi \frac{dB_\nu}{dT} \Big|_{T_{\text{rad}}} \frac{dT_{\text{rad}}}{dT_s} d\nu.
 \end{aligned} \tag{16}$$

The minus sign ensures consistency with the sign convention used in most climate studies: OLR typically increases in response to surface warming, so  $\lambda_{LW} < 0$ . Note that Equation 16 does not contain any terms  $\propto d\tau_{\text{surf}}/dT_s$  because the resulting contribution to change in the surface emission decreases with warming at exactly the same rate as the atmospheric emission increases (this can be seen by differentiating Eqn. 14 first before applying the emission-level approximation).

### *b. Spectral feedback decomposition*

The net feedback in Equation 16 can be decomposed into multiple spectral regions or bands. The surface term dominates in the window region where  $\tau_{\text{surf}} < 1$  and the feedback is primarily a function of surface temperature  $T_s$ . The atmospheric emission dominates where  $\tau_{\text{surf}} > 1$ , and its magnitude primarily depends on the derivative  $dT_{\text{rad}}/dT_s$ . As we show below,  $dT_{\text{rad}}/dT_s$  differs depending on the opacity source at a given wavenumber. In this work we only consider Earth's dominant greenhouse gases, CO<sub>2</sub> and H<sub>2</sub>O, where H<sub>2</sub>O's radiative effect additionally varies between the H<sub>2</sub>O bands and the H<sub>2</sub>O continuum, so we split the spectral integral into four terms:

$$\begin{aligned}
 -\lambda_{LW} &= \int_{\text{surf}} \pi \frac{dB_\nu}{dT} \Big|_{T_s} e^{-\tau_{\text{surf}}} d\nu + \int_{\text{CO}_2} \pi \frac{dB_\nu}{dT} \Big|_{T_{\text{CO}_2}} \frac{dT_{\text{CO}_2}}{dT_s} d\nu + \\
 &\quad \int_{\text{H}_2\text{O}} \pi \frac{dB_\nu}{dT} \Big|_{T_{\text{H}_2\text{O}}} \frac{dT_{\text{H}_2\text{O}}}{dT_s} d\nu + \int_{\text{cnt}} \pi \frac{dB_\nu}{dT} \Big|_{T_{\text{cnt}}} \frac{dT_{\text{cnt}}}{dT_s} d\nu \\
 &= -(\lambda_{\text{surf}} + \lambda_{\text{CO}_2} + \lambda_{\text{H}_2\text{O}} + \lambda_{\text{cnt}}),
 \end{aligned} \tag{17}$$

where  $T_{\text{CO}_2}$ ,  $T_{\text{H}_2\text{O}}$  and  $T_{\text{cnt}}$  are the emission temperatures in the CO<sub>2</sub> band, the H<sub>2</sub>O band, and the H<sub>2</sub>O continuum respectively (the wavenumber range of each integral is discussed in Section 5a). Based on the emitter, we refer to the four feedback terms as the surface feedback ( $\lambda_{\text{surf}}$ ), the CO<sub>2</sub> band feedback ( $\lambda_{\text{CO}_2}$ ), the (non-Simpsonian) H<sub>2</sub>O band feedback ( $\lambda_{\text{H}_2\text{O}}$ ), and the H<sub>2</sub>O continuum feedback ( $\lambda_{\text{cnt}}$ ).



Our spectral decomposition complements the conventional feedback decomposition which splits  $\lambda_{LW}$  into Planck, Lapse-Rate, and Water Vapor (or Relative Humidity) feedbacks. The surface feedback  $\lambda_{\text{surf}}$  measures the OLR increase due to surface warming while keeping the atmosphere fixed. This term is identical to the surface contribution of the Planck feedback, or “surface kernel”, in the conventional decomposition (Soden et al. 2008). As for the atmospheric feedback, Equation 16 shows that it depends on the *total* derivative of  $T_{\text{rad}}$ , that is, on  $dT_{\text{rad}}/dT_s$ . The conventional decomposition can be interpreted as splitting the total derivative  $dT_{\text{rad}}/dT_s$  up into various partial derivatives (uniform warming versus lapse-rate versus water vapor changes), while using a single, spectrally-averaged  $T_{\text{rad}}$ . In contrast, our decomposition splits the atmosphere’s feedback into three different bands, but still retains the total derivative  $dT_{\text{rad}}/dT_s$  in each band. In principle our decomposition could be split further to recover the conventional decomposition. That is, one could further decompose  $dT_{\text{rad}}/dT_s$  in each band into partial derivatives of  $T_{\text{rad}}$  that correspond to vertically-uniform warming, lapse-rate warming, and water-vapor changes – see Jeevanjee et al. (2021a) for more details. Here, however, we do not pursue this approach because our analytic expressions are general enough to predict  $T_{\text{rad}}$  and the total derivative  $dT_{\text{rad}}/dT_s$ .

We use relative humidity as the state variable throughout this paper, so the analytic results are compatible with papers that argue for the use of relative humidity in feedback decompositions instead of specific humidity (Held and Shell 2012; Jeevanjee et al. 2021a). In the fixed-RH framework the conventional Water Vapor feedback is replaced by a Relative Humidity feedback, which measures the clear-sky feedback due to RH changes. It is worth noting that the RH feedback is small in individual climate models, and its multi-model mean is close to zero (Zelinka et al. 2020). In the derivations below we therefore treat RH as an external parameter whose value is assumed constant under surface warming.

### *c. Line-by-line calculations*

To calculate spectral feedbacks numerically we use a 1D line-by-line model, PyRADS (Koll and Cronin 2018). The model’s radiative transfer includes HITRAN2016 CO<sub>2</sub> and H<sub>2</sub>O absorption data as well as the H<sub>2</sub>O component of the MTCKD continuum version 3.2 (Mlawer et al. 2012; Gordon et al. 2017). Calculations cover the spectral range 0.1-2500 cm<sup>-1</sup> with a resolution of  $\Delta\nu = 0.01$  cm<sup>-1</sup>, while the vertical resolution is 50 points in log-pressure. In general the angular distribution

of longwave radiation  $\cos(\bar{\theta})$  varies in the vertical as well as across wavenumber (Li 2000; Feng and Huang 2019); however, a common approximation is to assume  $\cos(\bar{\theta}) = 3/5$  (Elsasser 1942), which is also used here.

The 1D calculations assume the atmosphere's temperature profile follows either a moist adiabat or a power law temperature-pressure profile that is consistent with our bulk lapse rate approximation. In both cases the troposphere is capped by a tropopause at 200 K, while the overlying stratosphere is isothermal at the same temperature. Relative humidity in the troposphere is vertically uniform while the H<sub>2</sub>O mass fraction in the stratosphere is set equal to its value at the tropopause. CO<sub>2</sub> is treated as uniformly mixed in the vertical and fixed with respect to surface temperature. Because we are considering a wide range of surface temperatures, across which the tropopause pressure varies substantially, we vary the vertical grid-spacing in PyRADS: for each surface temperature, the model top pressure is set to a slightly lower value than the estimated tropopause pressure based on our bulk lapse rate formulation, which ensures the model's top is always in the stratosphere and the tropopause is well resolved.

The spectrally-resolved feedback is the difference in the spectrally-resolved outgoing longwave flux,  $\text{OLR}_v$ , between a base state and a perturbed state with warmed surface and atmosphere,

$$-\lambda_v = \frac{\text{OLR}_v(T_s + \Delta T_s, \vec{T} + \Delta \vec{T}) - \text{OLR}_v(T_s, \vec{T})}{\Delta T_s}. \quad (18)$$

We use  $\Delta T_s = 1$  K, while  $\Delta \vec{T}$  denotes the atmospheric temperature perturbation caused by the surface warming  $\Delta T_s$ . Because relative humidity is kept fixed, the atmospheric warming  $\vec{T} + \Delta \vec{T}$  also implies an increase in specific humidity.

Previous work has used various approaches to interpret line-by-line output. Seeley and Jeevanjee (2021) defined CO<sub>2</sub> versus H<sub>2</sub>O bands based on the column-integrated, spectrally-smoothed optical thickness of CO<sub>2</sub> and H<sub>2</sub>O. However, the behavior of H<sub>2</sub>O differs strongly between the H<sub>2</sub>O bands and the H<sub>2</sub>O continuum, and it is difficult to distinguish these terms based on column-integrated optical thicknesses. For example, the H<sub>2</sub>O continuum might have a larger integrated optical thickness at some wavenumber than the H<sub>2</sub>O bands, but because continuum absorption decays more rapidly with altitude than band absorption ( $\kappa_{\text{cnt}} \propto e^*(T)$  versus  $\kappa_{\text{H}_2\text{O}} \propto p$ ) the emission at the level where  $\tau \sim 1$  could still be determined by the H<sub>2</sub>O bands.

Instead we first split the net feedback into its contributions from the surface versus atmosphere. The spectrally-resolved surface feedback is the feedback in response to surface-only warming while keeping the atmosphere fixed,

$$-\lambda_{\text{surf}}^{\nu} = \frac{\text{OLR}_{\nu}(T_s + \Delta T_s, \vec{T}) - \text{OLR}_{\nu}(T_s, \vec{T})}{\Delta T_s}. \quad (19)$$

If we integrate  $\lambda_{\text{surf}}^{\nu}$  over all wavenumbers we get the surface feedback  $\lambda_{\text{surf}}$ , equivalent to the surface kernel of Soden et al. (2008). The atmospheric feedback is equal to the difference between  $\lambda_{\nu}$  and  $\lambda_{\text{surf}}^{\nu}$ ,

$$-\lambda_{\text{atm}}^{\nu} = \frac{\text{OLR}_{\nu}(T_s, \vec{T} + \Delta \vec{T}) - \text{OLR}_{\nu}(T_s, \vec{T})}{\Delta T_s}. \quad (20)$$

We split  $\lambda_{\text{atm}}^{\nu}$  into different bands based on the spectrally-resolved emission pressures of CO<sub>2</sub>, H<sub>2</sub>O, and the H<sub>2</sub>O continuum. For each absorber PyRADS computes the optical thickness as a function of pressure and wavenumber,  $\tau(p, \nu)$ . We define the CO<sub>2</sub> emission pressure as the pressure at which the optical thickness of CO<sub>2</sub> is equal to unity,

$$\tau_{\text{CO}_2}(p_{\text{rad}}, \nu) = 1, \quad (21)$$

which can be solved in each wavenumber bin to find  $p_{\text{rad}}(\nu)$  (in practice we interpolate to find the pressure at which  $\log[\tau] = 0$ ). The emission pressures of H<sub>2</sub>O and the H<sub>2</sub>O continuum are determined for each wavenumber bin in the same manner. The CO<sub>2</sub> band feedback  $\lambda_{\text{CO}_2}$  is then the integral of  $\lambda_{\text{atm}}^{\nu}$  over all wavenumbers at which CO<sub>2</sub> has the smallest emission pressure, the H<sub>2</sub>O band feedback  $\lambda_{\text{H}_2\text{O}}$  is the integral of  $\lambda_{\text{atm}}^{\nu}$  over all wavenumbers at which H<sub>2</sub>O has the smallest emission pressure, and so on. The spectral decomposition is recomputed each time the atmosphere or surface state is varied, thereby allowing us to capture the state-dependence of the longwave feedback not just due to changes in the atmosphere's and surface's emission but also due to changes in the width of spectral bands. We note that this approach is justified if one emitter clearly dominates the atmosphere's emission at a given wavenumber, such that its emission pressure  $p_{\text{rad}}$  is much lower than that of any other emitters, but could be misleading if two emitters have very similar emission pressures. In practice, H<sub>2</sub>O and CO<sub>2</sub> absorption cross-sections decrease

quasi-exponentially away from their band centers (see Section 2), which means the wavenumber range over which two absorbers can have a similar emission pressure is limited.

#### 4. Emission temperatures

The feedbacks are set by the temperatures at the  $\tau = 1$  levels, so we seek analytic expressions for the emission temperatures  $T_{\text{CO}_2}$ ,  $T_{\text{H}_2\text{O}}$  and  $T_{\text{cnt}}$ . The optical thickness of a generic absorber is

$$\tau = \int \kappa q \frac{dp}{g \cos(\bar{\theta})}, \quad (22)$$

where  $\kappa$  is the absorption cross-section and  $q$  is the absorber's mass-specific concentration. We use this equation to derive expressions for the emission temperatures by first writing the optical thickness in each band as a function of atmospheric temperature, then inverting these relations to find the emission temperature at the  $\tau = 1$  level.

##### a. $\text{CO}_2$

$\text{CO}_2$  is well-mixed in the atmosphere so its mass-specific concentration  $q_{\text{CO}_2}$  is vertically uniform. As discussed in Section 2, its absorption cross-section depends linearly on pressure due to pressure broadening and can be written as  $\kappa_{\text{CO}_2}(\nu, p) = \kappa_{\text{CO}_2}^*(\nu)(p/p_0)$ , where  $\kappa_{\text{CO}_2}^*$  captures the wavenumber-dependence of the  $\text{CO}_2$  absorption cross-section,  $\kappa_{\text{CO}_2}^* \propto \exp(-|\nu - \nu_0|/l_\nu)$ , while  $p_0$  is an reference pressure. Because we previously chose  $p_0$  to be equal to the dry surface pressure, one can write  $\kappa_{\text{CO}_2}^*(\nu) \approx \kappa_{\text{CO}_2}^*(\nu, p_s)$  (the approximation is due to neglecting the mass contribution of water vapor to  $p_s$ ). The optical thickness at a vertical level with temperature and pressure  $(T, p)$  is then

$$\begin{aligned} \tau_{\text{CO}_2} &= \int_0^p \kappa_{\text{CO}_2}^* \left( \frac{p'}{p_s} \right) q_{\text{CO}_2} \frac{dp'}{g \cos(\bar{\theta})}, \\ &= \frac{\kappa_{\text{CO}_2}^*}{2g \cos(\bar{\theta}) p_s} q_{\text{CO}_2} p^2, \\ &= \frac{\kappa_{\text{CO}_2}^* p_s}{2g \cos(\bar{\theta})} q_{\text{CO}_2} \left( \frac{p}{p_s} \right)^2 \\ &= \frac{\kappa_{\text{CO}_2}^* p_s}{2g \cos(\bar{\theta})} q_{\text{CO}_2} \left( \frac{T}{T_s} \right)^{2/\gamma_{\text{r}}} \\ &\equiv \tau_{\text{CO}_2}^*(\nu) q_{\text{CO}_2} \times \left( \frac{T}{T_s} \right)^{2/\gamma_{\text{r}}}, \end{aligned} \quad (23)$$

where the fourth step uses the bulk lapse rate. Note that all spectroscopic parameters as well as  $p_s$  and  $g$  are combined into a reference optical thickness,  $\tau_{\text{CO}_2}^*(\nu)$ , which encapsulates how  $\text{CO}_2$  absorption varies with respect to wavenumber  $\nu$ , surface pressure  $p_s$ , and gravity  $g$ , but which can be treated as constant in response to warming.

### b. Non-Simpsonian $\text{H}_2\text{O}$

As for  $\text{CO}_2$ , the absorption cross-section of  $\text{H}_2\text{O}$  scales linearly with pressure and can be written as  $\kappa_{\text{H}_2\text{O}}(\nu, p) = \kappa_{\text{H}_2\text{O}}^*(\nu)(p/p_s)$ . We use the Clausius-Clapeyron power law approximation to write the saturation specific humidity as  $q^* \approx R_d/R_v \times e_0^*/p \times (T/T_0)^{\gamma_{\text{wv}}}$  and the specific humidity as  $q = \text{RH} \times q^*$ . The optical thickness of  $\text{H}_2\text{O}$  at a level  $(T, p)$  is then

$$\begin{aligned}
 \tau_{\text{H}_2\text{O}} &= \int_0^p \kappa_{\text{H}_2\text{O}}^* \left( \frac{p'}{p_s} \right) q \frac{dp'}{g \cos(\bar{\theta})}, \\
 &\approx \text{RH} \frac{\kappa_{\text{H}_2\text{O}}^* e_0^* R_d}{g \cos(\bar{\theta}) R_v} \times \int_0^p \left( \frac{p'}{p_s} \right) \left( \frac{T'}{T_0} \right)^{\gamma_{\text{wv}}} \frac{dp'}{p'} \\
 &= \text{RH} \frac{\kappa_{\text{H}_2\text{O}}^* e_0^* R_d}{g \cos(\bar{\theta}) R_v} \times \int_0^T \left( \frac{T'}{T_s} \right)^{1/\gamma_{\text{lr}}} \left( \frac{T'}{T_0} \right)^{\gamma_{\text{wv}}} \frac{1}{\gamma_{\text{lr}}} \frac{dT'}{T'} \\
 &= \text{RH} \frac{\kappa_{\text{H}_2\text{O}}^* e_0^* R_d}{g \cos(\bar{\theta}) R_v} \frac{1}{\gamma_{\text{lr}}} \left( \frac{T_0}{T_s} \right)^{1/\gamma_{\text{lr}}} \times \int_0^T \left( \frac{T'}{T_0} \right)^{\gamma_{\text{wv}} + \frac{1}{\gamma_{\text{lr}}}} \frac{dT'}{T'} \\
 &= \text{RH} \frac{\kappa_{\text{H}_2\text{O}}^* e_0^* R_d}{g \cos(\bar{\theta}) R_v} \frac{1}{1 + \gamma_{\text{wv}} \gamma_{\text{lr}}} \times \left( \frac{T}{T_0} \right)^{\frac{1 + \gamma_{\text{wv}} \gamma_{\text{lr}}}{\gamma_{\text{lr}}}} \left( \frac{T_0}{T_s} \right)^{1/\gamma_{\text{lr}}} \\
 &\equiv \text{RH} \tau_{\text{H}_2\text{O}}^*(\nu) \frac{1}{1 + \gamma_{\text{wv}} \gamma_{\text{lr}}} \times \left( \frac{T}{T_0} \right)^{\frac{1 + \gamma_{\text{wv}} \gamma_{\text{lr}}}{\gamma_{\text{lr}}}} \left( \frac{T_0}{T_s} \right)^{1/\gamma_{\text{lr}}}. \tag{24}
 \end{aligned}$$

where the second step uses the Clausius-Clapeyron power law and also replaces the water vapor concentration in the stratosphere with the water vapor concentration of a moist adiabat that extends all the way to the top-of-atmosphere. We again define a reference optical thickness,  $\tau_{\text{H}_2\text{O}}^*(\nu)$ , which encapsulates how  $\text{H}_2\text{O}$  band absorption varies with respect to wavenumber  $\nu$ , and gravity  $g$ , but which is independent of temperature.

### c. $\text{H}_2\text{O}$ Continuum

Absorption by the  $\text{H}_2\text{O}$  continuum strengthens in response to increasing water vapor concentrations and weakens in response to warming,  $\kappa_{\text{H}_2\text{O}, \text{cnt}} = \kappa_{\text{cnt}} \times \text{RH} e^*(T)/e^*(T_0) \times (T/T_0)^{-a}$ . The

optical thickness of the continuum is then

$$\begin{aligned}
\tau_{\text{cnt}} &= \text{RH} \int_0^p \kappa_{\text{cnt}} \frac{e^*(T')}{e^*(T_0)} \left(\frac{T'}{T_0}\right)^{-a} q \frac{dp'}{g \cos(\bar{\theta})}, \\
&\approx \text{RH}^2 \frac{\kappa_{\text{cnt}} e_0^*}{g \cos(\bar{\theta})} \frac{R_d}{R_v} \times \int_0^T \left(\frac{T'}{T_0}\right)^{2\gamma_{\text{wv}}-a} \frac{dT'}{p}, \\
&= \text{RH}^2 \frac{\kappa_{\text{cnt}} e_0^*}{g \cos(\bar{\theta})} \frac{R_d}{R_v} \times \int_0^T \left(\frac{T'}{T_0}\right)^{2\gamma_{\text{wv}}-a} \frac{1}{\gamma_{\text{lr}} T'} dT', \\
&= \text{RH}^2 \frac{\kappa_{\text{cnt}} e_0^*}{g \cos(\bar{\theta})} \frac{R_d}{R_v} \frac{1}{(2\gamma_{\text{wv}}-a)\gamma_{\text{lr}}} \times \left(\frac{T}{T_0}\right)^{2\gamma_{\text{wv}}-a}, \\
&\equiv \text{RH}^2 \tau_{\text{cnt}}^* \frac{1}{(2\gamma_{\text{wv}}-a)\gamma_{\text{lr}}} \times \left(\frac{T}{T_0}\right)^{2\gamma_{\text{wv}}-a}, \tag{25}
\end{aligned}$$

where the second and third steps make the same assumptions as the derivation for the H<sub>2</sub>O band. Here the reference optical thickness,  $\tau_{\text{cnt}}^*$  encapsulates how the H<sub>2</sub>O self-continuum varies with respect to gravity  $g$  but has no dependence on wavenumber or temperature.

#### d. Emission temperatures

By setting  $\tau = 1$  and inverting the above relations, we arrive at the emission temperatures in the CO<sub>2</sub> band, the H<sub>2</sub>O band and the H<sub>2</sub>O self-continuum:

$$T_{\text{CO}_2} = T_s \left( \frac{1}{\tau_{\text{CO}_2}^*(\nu) q_{\text{CO}_2}} \right)^{\gamma_{\text{lr}}/2} \tag{26a}$$

$$T_{\text{H}_2\text{O}} = T_0 \left( \frac{1 + \gamma_{\text{wv}} \gamma_{\text{lr}}}{\tau_{\text{H}_2\text{O}}^*(\nu) \text{RH}} \right)^{\frac{\gamma_{\text{lr}}}{1 + \gamma_{\text{wv}} \gamma_{\text{lr}}}} \left( \frac{T_s}{T_0} \right)^{\frac{1}{1 + \gamma_{\text{wv}} \gamma_{\text{lr}}}} \tag{26b}$$

$$T_{\text{cnt}} = T_0 \left( \frac{(2\gamma_{\text{wv}} - a) \gamma_{\text{lr}}}{\tau_{\text{cnt}}^* \text{RH}^2} \right)^{\frac{1}{2\gamma_{\text{wv}} - a}}. \tag{26c}$$

To interpret these emission temperatures, consider whether a given emitter stabilizes or destabilizes Earth's climate. For CO<sub>2</sub> it is easy to see that the feedback is always stabilizing. Ignoring lapse rate changes we have  $T_{\text{CO}_2} \propto T_s$ , so  $dT_{\text{CO}_2}/dT_s > 0$ . More intuitively, the optical thickness of

CO<sub>2</sub> can be written as

$$\tau_{\text{CO}_2} \propto \left(\frac{T}{T_s}\right)^{2/\gamma_{\text{lr}}} = \left(\frac{p}{p_s}\right)^2. \quad (27)$$

The emission level of CO<sub>2</sub> is therefore a fixed function of pressure at a given atmospheric CO<sub>2</sub> concentration. Given that the atmosphere's temperature at a fixed pressure level always increases in response to surface warming,  $T_{\text{CO}_2}$  also has to increase under warming. This effect can be thought of as a spectral radiator fin, and is also valid if the lapse rate  $\gamma_{\text{lr}}$  varies under surface warming. It implies that even if the atmosphere stops emitting more at all other wavenumbers, so  $dT_{\text{rad}}/dT_s = 0$  outside the CO<sub>2</sub> band, the presence of CO<sub>2</sub> still allows the atmosphere to shed more energy to space in response to surface warming (Seeley and Jeevanjee 2021).

Next, our expressions suggest that the feedback from H<sub>2</sub>O is small and, to first order, might be negligible. Equation 26b shows  $T_{\text{H}_2\text{O}} \propto T_s^{1/(1+\gamma_{\text{wv}}\gamma_{\text{lr}})}$ , where representative values for Earth's tropics are  $\gamma_{\text{wv}} \sim 20$  and  $\gamma_{\text{lr}} \sim 1/7$ , so the H<sub>2</sub>O emission temperature only depends weakly on surface temperature,  $T_{\text{H}_2\text{O}} \propto T_s^{1/4}$ . This small exponent is closely related to Simpson's "paradox" (Ingram 2010) or Simpson's "law" (Jeevanjee et al. 2021a), which state that  $T_{\text{H}_2\text{O}}$  is approximately independent of surface temperature. In the limit  $\gamma_{\text{wv}}\gamma_{\text{lr}} = d \ln e^* / d \ln p \gg 1$ , that is, if water vapor increases much faster in the vertical than the total atmospheric mass, then

$$T_{\text{H}_2\text{O}} \approx T_0 \left( \frac{\gamma_{\text{wv}}\gamma_{\text{lr}}}{\tau_{\text{H}_2\text{O}}^*(\nu)RH} \right)^{\frac{1}{\gamma_{\text{wv}}}}, \quad (28)$$

and  $T_{\text{H}_2\text{O}}$  ceases to depend on  $T_s$ . If the lapse rate is also independent of  $T_s$  we recover Simpson's law:

$$\frac{dT_{\text{H}_2\text{O}}}{dT_s} \approx 0. \quad (29)$$

In reality, however, water vapor dominates much of the spectrum so even minor deviations from Simpson's law can have a notable impact on the longwave feedback. Deviations arise because the H<sub>2</sub>O optical thickness is sensitive to pressure broadening and because changes in  $\gamma_{\text{lr}}$  modify the total water vapor path inside the atmospheric column. For present-day Earth the net impact of these

changes is to increase the H<sub>2</sub>O emission temperature under surface warming: since  $T_{\text{H}_2\text{O}} \propto T_s^{1/4}$ , it follows that  $dT_{\text{H}_2\text{O}}/dT_s > 0$ , which means the H<sub>2</sub>O bands tend to stabilize Earth's climate.

Finally,  $T_{\text{cnt}}$  has no direct dependence on surface temperature, but is sensitive to lapse rate changes. If we take the continuum's emission temperature (Eqn. 26c), and assume that the direct temperature-dependence of the continuum  $a \sim 7$  is much smaller than its temperature-dependence due to the Clausius-Clapeyron relation,  $2\gamma_{\text{wv}} \sim 40$ , we have

$$T_{\text{cnt}} \propto T_0 \times [\gamma_{\text{lr}}]^{1/(2\gamma_{\text{wv}})}. \quad (30)$$

Because the lapse rate  $\gamma_{\text{lr}}$  decreases under surface warming we have  $dT_{\text{cnt}}/dT_s = dT_{\text{cnt}}/d\gamma_{\text{lr}} \times d\gamma_{\text{lr}}/dT_s < 0$ . Physically, this effect can be understood by considering the impact of  $\gamma_{\text{lr}}$  on the atmosphere's total water vapor path. If one decreases the lapse rate  $\gamma_{\text{lr}}$  while keeping  $T_s$  fixed, the atmospheric column warms and thus can store more water vapor. To still maintain an optical thickness of unity then requires that the continuum's emission level moves to colder temperatures. Our expressions thus predict that the H<sub>2</sub>O continuum gives rise to a destabilizing feedback.

#### *e. Comparison against LBL calculations*

Equations 26a - 26c predict how Earth's emission temperature varies in response to changes in  $T_s$ ,  $q_{\text{CO}_2}$ ,  $\gamma_{\text{lr}}$  and RH. To test these equations we perform four sets of numerical experiments with PyRADS in which we variously change  $T_s$ ,  $q_{\text{CO}_2}$ ,  $\gamma_{\text{lr}}$ , and RH while holding the other parameters fixed. The default values are  $T_s = 290$  K, 400 ppm of CO<sub>2</sub>,  $\gamma_{\text{lr}} = 2/7$ , and RH = 0.8. To match our underlying assumptions we assume a bulk tropospheric lapse rate, so  $T = T_s(p/p_s)^{\gamma_{\text{lr}}}$ , which means the temperature profile differs from an adiabat if  $\gamma_{\text{lr}} < 2/7$ . The troposphere is capped by an isothermal stratosphere which is kept fixed at  $T_{\text{strat}} = 200$  K. Note that in Equations 26a - 26c the dependence on wavenumber only enters through the reference optical thicknesses  $\tau_{\text{CO}_2}^*$ ,  $\tau_{\text{H}_2\text{O}}^*$ , and  $\tau_{\text{cnt}}^*$ , which are evaluated using the cross-sections from Section 2. Because the cross-sections were fit independently, the analytic  $T_{\text{rad}}$  expressions do not contain any free tuning parameters.

To compare the analytic results against line-by-line calculations we first numerically compute the top-of-atmosphere spectral flux  $\text{OLR}_\nu$  for a given set of  $(T_s, q_{\text{CO}_2}, \gamma_{\text{lr}}, \text{RH})$ . We then smooth  $\text{OLR}_\nu$  with a median filter of width  $50 \text{ cm}^{-1}$ , before inverting it using the Planck function to find the



atmosphere's emission temperature (also known as brightness temperature) at a given wavenumber. Finally, we combine our analytic expressions into a single emission temperature via

$$T_{\text{rad}} = \max \left[ T_{\text{strat}}, \min \left[ T_s, T_{\text{CO}_2}, T_{\text{H}_2\text{O}}, T_{\text{cnt}} \right] \right], \quad (31)$$

to compare directly with temperatures from line-by-line calculations.

Figure 4 demonstrates that the analytic results compare favorably against numerical calculations. Even though the analytic  $T_{\text{rad}}$  shapes are idealized compared to the numerical calculations, the overall response of  $T_{\text{rad}}$  to perturbations is captured well. First, increasing  $\text{CO}_2$  concentration lowers  $T_{\text{rad}}$  around  $667 \text{ cm}^{-1}$ , which corresponds to the wings of the  $\text{CO}_2$  band. This is simply a spectrally resolved view of how increasing  $\text{CO}_2$  acts as a radiative forcing (Jeevanjee et al. 2021b). Second, warming the surface while keeping all other parameters fixed has multiple effects. The main impact is to increase the emission temperature in the window region between  $\sim 800$  and  $1200 \text{ cm}^{-1}$ . In addition there are secondary impacts: surface warming also shrinks the width of the  $\text{CO}_2$  band and slightly increases the emission temperature in the  $\text{H}_2\text{O}$  bands below  $600 \text{ cm}^{-1}$  and above  $1300 \text{ cm}^{-1}$  (this latter effect is hard to see in Figure 4). The increased emission in the  $\text{H}_2\text{O}$  bands shows that Simpson's law in Equation 29 is not exact, an effect that is captured by our analytic expressions. Third, reducing the lapse rate  $\gamma_{\text{lr}}$  preserves the width of the  $\text{CO}_2$  band, but it flattens the steepness of its slopes and increases the emission temperature in the center of the band. In the  $\text{H}_2\text{O}$  bands, a smaller  $\gamma_{\text{lr}}$  while keeping  $T_s$  fixed also leads to a non-Simpsonian increase of the emission temperature in the  $\text{H}_2\text{O}$  bands. In contrast to the  $\text{H}_2\text{O}$  bands, the emission temperature of the  $\text{H}_2\text{O}$  continuum around  $1000 \text{ cm}^{-1}$  decreases as  $\gamma_{\text{lr}}$  is reduced. As discussed above, this is because the atmospheric water path increases with a smaller  $\gamma_{\text{lr}}$ , which reduces  $T_{\text{cnt}}$ . The feedback of the  $\text{H}_2\text{O}$  continuum therefore has the opposite sign as the  $\text{H}_2\text{O}$  bands, in line with the analytic results. Finally, reducing the relative humidity increases  $T_{\text{rad}}$  in all regions dominated by water vapor, both in the  $\text{H}_2\text{O}$  bands below  $600 \text{ cm}^{-1}$ /above  $1300 \text{ cm}^{-1}$  and in the  $\text{H}_2\text{O}$  continuum around  $1000 \text{ cm}^{-1}$ , while the  $\text{CO}_2$  band is unaffected.

Overall, Figure 4 underlines that comparatively simple physics is sufficient to explain the spectrally-resolved response of  $T_{\text{rad}}$  to different climate perturbations. To connect Figure 4 back to the total clear-sky longwave feedback we only need to consider how these changes in  $T_{\text{rad}}$  play

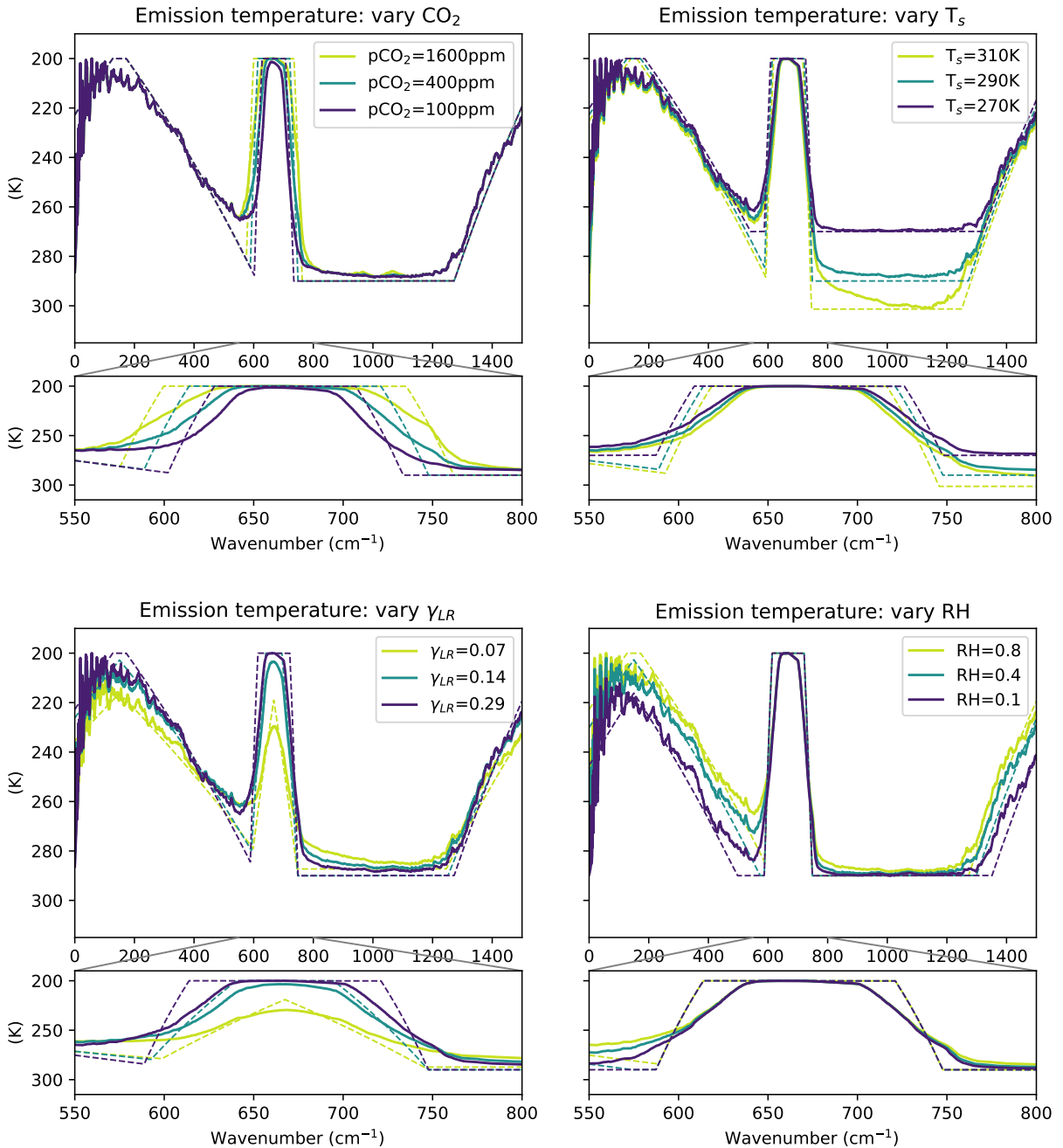


FIG. 4. Analytic emission temperatures (dashed), compared against numerical line-by-line results smoothed with a median filter of width  $50 \text{ cm}^{-1}$ . Large rows show the entire infrared spectrum, small rows are zoomed in on the  $\text{CO}_2$  band. The y-axes are flipped so that emission temperature decreases going up, the same way temperature decreases with altitude in Earth's atmosphere.

out once we average them into spectral bands, and how multiple bands add up to determine the net longwave feedback.

## 5. Analytic Feedbacks

Having derived expressions for the emission temperature in different parts of the LW spectrum, and verified these expressions against line-by-line calculations, we can now derive analytic expressions for the four spectral feedbacks:  $\lambda_{\text{surf}}$ ,  $\lambda_{\text{CO}_2}$ ,  $\lambda_{\text{H}_2\text{O}}$  and  $\lambda_{\text{cnt}}$ . Above each spectral feedback was defined as an integral over a wavenumber range (Eqn. 17), but the wavenumber ranges were not further specified. We therefore first define and estimate the width of the different spectral bands.

### a. Band widths

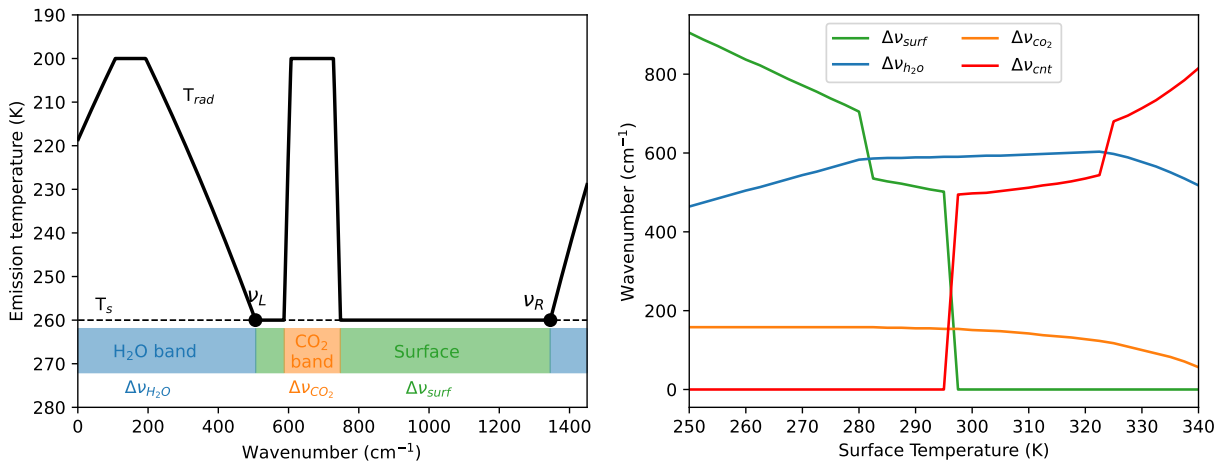


FIG. 5. Illustration of spectral band widths. The emission temperature is equal to the emission temperature of whichever emitter is coldest,  $T_{\text{rad}} = \min[T_{\text{CO}_2}, T_{\text{H}_2\text{O}}, T_{\text{cnt}}, T_s]$ , or the stratospheric temperature. Left: Lines show the analytic  $T_{\text{rad}}$  (solid) and surface temperature  $T_s$  (dashed), while colored regions illustrate which emitters dominate in which band. The calculation shown uses  $T_s = 260$  K, RH = 0.8, and 400ppm of CO<sub>2</sub>. Right: Band widths as a function of surface temperature, numerically calculated based on our emission temperature expressions. Here  $\Delta\nu_{\text{H}_2\text{O}}$  refers only to the rotational band at wavenumbers lower than 1000 cm<sup>-1</sup>. The jumps at  $\sim 280$  K,  $\sim 295$  K and  $\sim 325$  K occur when the H<sub>2</sub>O band starts intersecting the CO<sub>2</sub> band; when the continuum becomes opaque; and when the continuum becomes opaque on the left side of the CO<sub>2</sub> band, at wavenumbers less than about 600 cm<sup>-1</sup>, respectively.

We define an absorption band as the spectral range in which a given absorber has the coldest emission temperature compared to all other absorbers (this is equivalent to the highest-altitude emission level), and thus dominates the column's emission to space. For example, the CO<sub>2</sub> band is defined as all wavenumbers in which  $T_{\text{CO}_2} < \min[T_{\text{H}_2\text{O}}, T_{\text{cnt}}, T_s]$ , as illustrated in Figure 5a. The width of the CO<sub>2</sub> band can then be computed from the two wavenumbers  $\nu^{\text{edge}}$  which define the edges of the CO<sub>2</sub> band, which is where the emission temperature of CO<sub>2</sub> is equal to the emission temperatures of its neighboring absorbers:  $T_{\text{CO}_2}(\nu^{\text{edge}}) = \min[T_{\text{H}_2\text{O}}(\nu^{\text{edge}}), T_{\text{cnt}}, T_s]$ .

### 1) CO<sub>2</sub> BAND WIDTH

To estimate the width of the CO<sub>2</sub> band we consider three situations: (1) the CO<sub>2</sub> concentration  $q_{\text{CO}_2}$  is so low that even in the center of the CO<sub>2</sub> band the optical thickness is less than one; (2) a dry atmosphere in which there is no overlap between CO<sub>2</sub> and H<sub>2</sub>O bands; and (3) a moist atmosphere in which there is some overlap between CO<sub>2</sub> and H<sub>2</sub>O.

First, at very low CO<sub>2</sub> concentrations the band width of CO<sub>2</sub> is simply equal to zero. From the optical thickness of CO<sub>2</sub> (Eqn. 23), the column-integrated optical thickness in the middle of the CO<sub>2</sub> band is equal to  $\tau_{\text{CO}_2}(\nu_0, T_s) = q_{\text{CO}_2} \tau_{\text{CO}_2}^*(\nu_0)$  so this occurs when

$$\Delta\nu_{\text{CO}_2} = 0, \quad \text{if } q_{\text{CO}_2} \tau_{\text{CO}_2}^*(\nu_0) < 1. \quad (32)$$

As a representative value, we evaluate  $\tau_{\text{CO}_2}^*(\nu_0)$  using  $\kappa_0 = 500 \text{ m}^2 \text{ kg}^{-1}$  from Section 2c. We find that the middle of the CO<sub>2</sub> band becomes optically thick above a CO<sub>2</sub> concentration of  $\sim 0.2$  ppm. Note this value is only approximate, as our idealized band model deviates from real CO<sub>2</sub> absorption cross-section in the middle of the CO<sub>2</sub> band (see Fig. 3).

Second, at non-negligible CO<sub>2</sub> concentrations and low water vapor concentrations, CO<sub>2</sub>-H<sub>2</sub>O overlap is negligible. Physically, this occurs either when the surface temperature is cold or the relative humidity is low; for simplicity we refer to this as the ‘‘cold’’ regime. In this regime the edge of the CO<sub>2</sub> band can be defined as the wavenumber  $\nu^{\text{cold}}$  at which  $T_{\text{CO}_2}$  intersects with the surface temperature  $T_s$ ,  $T_{\text{CO}_2}(\nu^{\text{cold}}) = T_s$ . The emission temperature of CO<sub>2</sub> is equal to  $T_{\text{CO}_2} = T_s \times (\tau_{\text{CO}_2}^* q_{\text{CO}_2})^{-\gamma_{\text{lr}}/2}$  (Eqn. 26a), while our model of CO<sub>2</sub> spectroscopy states  $\tau_{\text{CO}_2}(\nu)^* \propto \exp(-|\nu - \nu_0|/l_\nu)$

(Eqn. 11). Combining the two equations yields

$$\nu^{cold} = \nu_0 \pm l_\nu \log(q_{\text{CO}_2} \tau_{\text{CO}_2}^*(\nu_0)), \quad (33)$$

where  $\tau_{\text{CO}_2}^*(\nu_0) = \kappa_0(\nu_0)p_s/(2g)$  is the reference optical thickness in the center of the CO<sub>2</sub> band. The overall width of the CO<sub>2</sub> band in the cold regime is therefore

$$\Delta\nu_{\text{CO}_2}^{cold} = 2l_\nu \log(q_{\text{CO}_2} \tau_{\text{CO}_2}^*(\nu_0)). \quad (34)$$

To estimate the order of magnitude of  $\Delta\nu_{\text{CO}_2}^{cold}$  we again use  $\kappa_0 = 500 \text{ m}^2 \text{ kg}^{-1}$  and a  $q_{\text{CO}_2}$  that corresponds to 400ppm of CO<sub>2</sub>. The optical thickness in the center of the CO<sub>2</sub> band is  $\tau_{\text{CO}_2}^*(\nu_0) \sim 2600$ . This large optical thickness decreases exponentially with wavenumber away from  $\nu_0$ , so that  $T_{\text{CO}_2} = T_s$  only  $\sim 80 \text{ cm}^{-1}$  away from  $\nu_0$ . Because CO<sub>2</sub>'s band shape is symmetric about  $\nu_0$ , the present-day CO<sub>2</sub> band width is thus roughly  $160 \text{ cm}^{-1}$ .

Third, at high water vapor concentrations, surface emission is replaced by H<sub>2</sub>O emission. Physically, this occurs either when the surface temperature is hot and/or relative humidity is high; for simplicity we refer to this as the ‘‘hot’’ regime. In this regime we solve the CO<sub>2</sub> band width as  $T_{\text{CO}_2}(\nu^{hot}) = T_{\text{H}_2\text{O}}(\nu^{hot})$ . Because the CO<sub>2</sub> band decays much faster with wavenumber away from its band center than the H<sub>2</sub>O band does ( $l_\nu \sim 10 \text{ cm}^{-1}$  versus  $l_{\text{rot}} \sim 55 \text{ cm}^{-1}$ ; see Table 1) we further approximate  $T_{\text{H}_2\text{O}}$  as constant across the CO<sub>2</sub> band and equal to its value in the CO<sub>2</sub> band center  $T_{\text{H}_2\text{O}}(\nu) \approx T_{\text{H}_2\text{O}}(\nu_0)$ . Combining the emission temperature of CO<sub>2</sub> (Eqn. 26a) with our model of CO<sub>2</sub> spectroscopy (Eqn. 11),

$$\nu^{hot} = \nu_0 \pm l_\nu \log \left[ q_{\text{CO}_2} \tau_{\text{CO}_2}^*(\nu_0) \left( \frac{T_{\text{H}_2\text{O}}(\nu_0)}{T_s} \right)^{\frac{2}{\gamma_r}} \right], \quad (35)$$

where the emission temperature of H<sub>2</sub>O can be evaluated using Eqn. 26b. Physically speaking, the H<sub>2</sub>O emission temperature is colder than the surface,  $T_{\text{H}_2\text{O}}(\nu_0)/T_s < 1$ , so our model correctly captures the fact that H<sub>2</sub>O-CO<sub>2</sub> overlap decreases the width of the CO<sub>2</sub> band. Taking into account

all three regimes, the overall width of the CO<sub>2</sub> band is therefore

$$\Delta\nu_{\text{CO}_2} = \begin{cases} 0, & \text{if } q_{\text{CO}_2}\tau_{\text{CO}_2}^*(\nu_0) < 1 \\ 2 \times \min(\nu^{\text{hot}} - \nu_0, \nu^{\text{cold}} - \nu_0), & \text{if } q_{\text{CO}_2}\tau_{\text{CO}_2}^*(\nu_0) \geq 1. \end{cases} \quad (36)$$

## 2) H<sub>2</sub>O BAND WIDTH

To determine the width of the H<sub>2</sub>O band the potential overlap with CO<sub>2</sub> matters less because the CO<sub>2</sub> band is too narrow to block a significant portion of the emission by H<sub>2</sub>O (at present-day CO<sub>2</sub> concentrations). However, at high water vapor concentrations, competition between the H<sub>2</sub>O bands and the H<sub>2</sub>O continuum becomes important, so we again consider a “cold” and a “hot” regime. At low water vapor concentrations (physically, at cold temperature or low relative humidity) continuum absorption is negligible and we solve  $T_{\text{H}_2\text{O}}(\nu^{\text{cold}}) = T_s$ . Combining the emission temperature of H<sub>2</sub>O (Eqn. 26b) with our H<sub>2</sub>O band model (Eqn. 12), this leads to

$$\nu_L^{\text{cold}} = \nu_{\text{rot}} + l_{\text{rot}} \log \left( \frac{\text{RH}\tau_{\text{rot}}^*(\nu_{\text{rot}})}{1 + \gamma_{\text{wv}}\gamma_{\text{lr}}} \left( \frac{T_s}{T_0} \right)^{\gamma_{\text{wv}}} \right), \quad (37a)$$

$$\nu_R^{\text{cold}} = \nu_{\text{v-r}} - l_{\text{v-r}} \log \left( \frac{\text{RH}\tau_{\text{v-r}}^*(\nu_{\text{v-r}})}{1 + \gamma_{\text{wv}}\gamma_{\text{lr}}} \left( \frac{T_s}{T_0} \right)^{\gamma_{\text{wv}}} \right), \quad (37b)$$

where  $\nu_L$  is the left edge of the window below  $\sim 1000 \text{ cm}^{-1}$ , and  $\nu_R$  is the right edge of the window above  $\sim 1000 \text{ cm}^{-1}$  (see Figure 5). The two H<sub>2</sub>O bands have different spectral slopes, and subscript “rot” denotes quantities that are related to the rotational H<sub>2</sub>O band at wavenumbers below  $1000 \text{ cm}^{-1}$  while subscript “v-r” denotes quantities related to the vibrational-rotational H<sub>2</sub>O band at wavenumbers above  $1000 \text{ cm}^{-1}$  (see Section 2). At high water vapor concentrations, the continuum cuts off emission from the surface so the H<sub>2</sub>O band edge  $\nu^{\text{hot}}$  is determined by  $T_{\text{H}_2\text{O}}(\nu^{\text{hot}}) = T_{\text{cnt}}$ . Using the emission temperature of H<sub>2</sub>O (Eqn. 26b) and our H<sub>2</sub>O band model, we find

$$\nu_L^{\text{hot}} = \nu_{\text{rot}} + l_{\text{rot}} \log \left[ \frac{\text{RH}\tau_{\text{rot}}^*(\nu_{\text{rot}})}{1 + \gamma_{\text{wv}}\gamma_{\text{lr}}} \left( \frac{T_0}{T_s} \right)^{1/\gamma_{\text{lr}}} \left( \frac{T_{\text{cnt}}}{T_0} \right)^{\frac{1+\gamma_{\text{wv}}\gamma_{\text{lr}}}{\gamma_{\text{lr}}}} \right], \quad (38a)$$

$$\nu_R^{\text{hot}} = \nu_{\text{v-r}} - l_{\text{v-r}} \log \left[ \frac{\text{RH}\tau_{\text{v-r}}^*(\nu_{\text{v-r}})}{1 + \gamma_{\text{wv}}\gamma_{\text{lr}}} \left( \frac{T_0}{T_s} \right)^{1/\gamma_{\text{lr}}} \left( \frac{T_{\text{cnt}}}{T_0} \right)^{\frac{1+\gamma_{\text{wv}}\gamma_{\text{lr}}}{\gamma_{\text{lr}}}} \right], \quad (38b)$$

where the continuum emission temperature is given by Eqn. 26c. Combining both regimes, the window width due to H<sub>2</sub>O absorption is therefore

$$\begin{aligned}\Delta\nu_{\text{surf}}(T_s, \text{RH}, \gamma_{\text{lr}}) &= \nu_R - \nu_L \\ &= \max(\nu_R^{\text{cold}}, \nu_R^{\text{hot}}) - \min(\nu_L^{\text{cold}}, \nu_L^{\text{hot}}).\end{aligned}\quad (39)$$

Similar to the CO<sub>2</sub> band width, Equations 37 and 38 become invalid at very low RH or  $T_s$  because in those situations H<sub>2</sub>O ceases to be optically thick at all wavenumbers (mathematically, this happens when RH or  $T_s$  become small enough that the logarithms in Eqns. 37 and 38 change sign). We do not consider the limit  $\text{RH} \rightarrow 0$  in this paper, but care should be taken when applying our results to extremely dry or cold atmospheres.

Finally, our feedback expression for the H<sub>2</sub>O band feedback requires us to separately specify the width of the rotational H<sub>2</sub>O band below 1000 cm<sup>-1</sup>. This width can be estimated by assuming that the rotational band always extends from 0 cm<sup>-1</sup> to the left edge of the window region  $\nu_L$  (see Figure 5). Doing so presumes that H<sub>2</sub>O is always optically thick at low wavenumbers around  $\nu = 0$  cm<sup>-1</sup>. While this assumption again breaks down in very cold or dry climates (the maximum absorption in the rotational band occurs around  $\nu \sim 150$  cm<sup>-1</sup>, not 0 cm<sup>-1</sup>, so low wavenumbers could become optically thin even if the band center is still optically thick), in those climates the H<sub>2</sub>O band feedback becomes negligible relative to the surface anyway. The width of the rotational H<sub>2</sub>O band is then

$$\Delta\nu_{\text{H}_2\text{O}}(T_s, \text{RH}, \gamma_{\text{lr}}) \approx \nu_L - 0 = \min(\nu_L^{\text{cold}}, \nu_L^{\text{hot}}),\quad (40)$$

where the wavenumber  $\nu_L$  denotes the left edge of the surface window (see above), as well as the right edge of the rotational H<sub>2</sub>O band.

### *b. Surface Feedback*

The surface feedback is given by

$$-\lambda_{\text{surf}} = \int_{\text{surf}} \pi \frac{dB_\nu}{dT} \Big|_{T_s} e^{-\tau_{\text{surf}}} d\nu.\quad (41)$$

The column-integrated optical thickness at a single frequency is the sum over all absorbers at that frequency,  $\tau_{\text{surf}}(\nu) = \tau_{\text{H}_2\text{O}}(\nu) + \tau_{\text{CO}_2}(\nu) + \tau_{\text{cnt}}$ . However, the optical thickness of H<sub>2</sub>O and CO<sub>2</sub> drops off exponentially as a function of wavenumber away from their band centers. Thus most frequencies are either so optically thick with respect to H<sub>2</sub>O and CO<sub>2</sub> that all surface radiation is absorbed by the atmosphere (and hence does not contribute to the surface feedback), or so optically thin that we can ignore H<sub>2</sub>O and CO<sub>2</sub>. Inside the window we therefore only consider absorption by the grey continuum,  $\tau_{\text{surf}} \approx \tau_{\text{cnt}}$ , while the H<sub>2</sub>O and CO<sub>2</sub> bands primarily set the width of the window.

To determine the width of the window we first consider an atmosphere without CO<sub>2</sub>. As discussed above, in this case the window region is set the H<sub>2</sub>O bands, with  $\nu_L$  denoting the left window edge around  $\sim 700 \text{ cm}^{-1}$  and  $\nu_R$  the right window edge around  $\sim 1200 \text{ cm}^{-1}$ . The H<sub>2</sub>O continuum is grey and so can be taken out of the spectral integral,

$$-\lambda_{\text{surf}} \approx e^{-\tau_{\text{cnt}}(T_s)} \int_{\nu_L}^{\nu_R} \pi \frac{dB_\nu}{dT} \Big|_{T_s} d\nu.$$

We approximate the integral by treating the Planck function derivative as constant with respect to wavenumber, evaluated at the central wavenumber  $\tilde{\nu}$  of the window region, so  $\int dB_\nu/dT d\nu \propto dB_{\tilde{\nu}}/dT \times \Delta\nu$ . In reality the Planck derivative is not constant with wavenumber, so our approximation should only be treated as a scaling which we account for by including a scaling constant  $c_{\text{surf}}$ . The magnitude of  $c_{\text{surf}}$  is further discussed below. The result is

$$-\lambda_{\text{surf}} \approx c_{\text{surf}} \times \pi \frac{dB_{\tilde{\nu}}}{dT} \Big|_{T_s} e^{-\tau_{\text{cnt}}(T_s)} \Delta\nu_{\text{surf}},$$

where  $\Delta\nu_{\text{surf}} = \nu_R - \nu_L$  is the window region width due to H<sub>2</sub>O band absorption (see Eqn. 39), and we determine the central wavenumber of the window as  $\tilde{\nu} = (\nu_R + \nu_L)/2$ .

Next, we add the effect of CO<sub>2</sub>-surface spectral blocking. Even if the atmosphere contained no water vapor whatsoever, part of the surface's emission would still be absorbed by CO<sub>2</sub> and thus have no effect on the TOA feedback. We account for the potential overlap between the surface and CO<sub>2</sub> by simply subtracting the CO<sub>2</sub> band width from the H<sub>2</sub>O-only window width,

$$\Delta\tilde{\nu}_{\text{surf}} = \max \left[ 0, \Delta\nu_{\text{surf}}(T_s, \text{RH}, \gamma_{\text{lr}}) - \Delta\nu_{\text{CO}_2}(q_{\text{CO}_2}) \right], \quad (42)$$



where  $\Delta\nu_{\text{CO}_2}$  is defined above (Eqn. 36) and the tilde distinguishes the window width here from the H<sub>2</sub>O-only window width. Our final expression for the surface feedback is thus

$$-\lambda_{\text{surf}} \approx c_{\text{surf}} \times \pi \frac{dB_{\tilde{\nu}}}{dT} \Big|_{T_s} e^{-\tau_{\text{cnt}}(T_s)} \Delta\tilde{\nu}_{\text{surf}}. \quad (43)$$

### c. H<sub>2</sub>O band feedback

The H<sub>2</sub>O band feedback is given by

$$-\lambda_{\text{H}_2\text{O}} = \int_{\text{H}_2\text{O}} \pi \frac{dB_{\nu}}{dT} \Big|_{T_{\text{H}_2\text{O}}} \frac{dT_{\text{H}_2\text{O}}}{dT_s} d\nu. \quad (44)$$

As sketched in Figure 5, we consider the rotational H<sub>2</sub>O band as ranging from  $\nu \approx 0$  to the left edge of the window,  $\nu_L$ . We do not consider the potential feedback from the vibration-rotation band at wavenumbers higher than  $\sim 1250 \text{ cm}^{-1}$  and, for purposes of the H<sub>2</sub>O band feedback, also ignore CO<sub>2</sub>-H<sub>2</sub>O overlap effects.

The derivative of  $T_{\text{H}_2\text{O}}$  can be solved analytically. If water vapor behaved strictly according to Simpson's law then  $dT_{\text{H}_2\text{O}}/dT_s = 0$  and the H<sub>2</sub>O band feedback would be zero. Simpson's law is only an approximation, however, so

$$\begin{aligned} \frac{dT_{\text{H}_2\text{O}}}{dT_s} &= \frac{\partial T_{\text{H}_2\text{O}}}{\partial T_s} + \frac{\partial T_{\text{H}_2\text{O}}}{\partial \gamma_{\text{lr}}} \frac{d\gamma_{\text{lr}}}{dT_s} \\ &= \frac{1}{1 + \gamma_{\text{wv}}\gamma_{\text{lr}}} \frac{T_{\text{H}_2\text{O}}}{T_s} + \\ &\quad \frac{\gamma_{\text{wv}}\gamma_{\text{lr}} - \gamma_{\text{wv}} \log\left(\frac{T_s}{T_0}\right) + \log\left(\frac{1 + \gamma_{\text{wv}}\gamma_{\text{lr}}}{\text{RH}\tau_0^*}\right)}{(1 + \gamma_{\text{wv}}\gamma_{\text{lr}})^2} T_{\text{H}_2\text{O}} \times \frac{d\gamma_{\text{lr}}}{dT_s}. \end{aligned} \quad (45)$$

One could also explicitly write out the lapse rate derivative  $d\gamma_{\text{lr}}/dT_s$ , but the resulting expressions are long and do not lead to additional physical insight, so in practice we evaluate  $d\gamma_{\text{lr}}/dT_s$  numerically. To estimate a typical value for  $dT_{\text{H}_2\text{O}}/dT_s$  we ignore lapse rate changes, that is, the second term in Equation 45. Assuming values representative of Earth's tropics,  $1 + \gamma_{\text{wv}}\gamma_{\text{lr}} = 1 + 1/7 \times 20 \sim 4$ , and representative temperatures  $T_{\text{H}_2\text{O}} \sim 240 \text{ K}$  (see Figure 4) and  $T_s \sim 300 \text{ K}$ , a characteristic value

for  $dT_{\text{H}_2\text{O}}/dT_s$  is thus

$$\frac{dT_{\text{H}_2\text{O}}}{dT_s} \sim \frac{1}{4} \times \frac{240}{300} = \frac{1}{5}, \quad (46)$$

in line with the numerical results of Jeevanjee et al. (2021a).

Next, we treat the H<sub>2</sub>O band feedback similar to the surface feedback. We assume the integrand of the spectral feedback integral is approximately constant with respect to wavenumber, and equal to its value at a central frequency  $\tilde{\nu}$ . The feedback is then

$$\begin{aligned} -\lambda_{\text{H}_2\text{O}} &= \int_0^{\nu_L} \pi \frac{dB_\nu}{dT} \Big|_{T_{\text{H}_2\text{O}}} \frac{dT_{\text{H}_2\text{O}}}{dT_s} d\nu \\ &\approx c_{\text{H}_2\text{O}} \times \pi \frac{dB_{\tilde{\nu}}}{dT} \Big|_{T_{\text{H}_2\text{O}}(\tilde{\nu})} \times \frac{dT_{\text{H}_2\text{O}}}{dT_s} \Big|_{\tilde{\nu}} \times \Delta\nu_{\text{H}_2\text{O}}, \end{aligned} \quad (47)$$

where  $\Delta\nu_{\text{H}_2\text{O}} = \nu_L$  is the width of the H<sub>2</sub>O band,  $\tilde{\nu} = \nu_L/2$  is the central wavenumber of the H<sub>2</sub>O band, and  $c_{\text{H}_2\text{O}}$  is again a scaling constant to account for the fact that we are replacing a spectral integral with simple multiplication.

#### d. H<sub>2</sub>O continuum feedback

The H<sub>2</sub>O continuum feedback is

$$-\lambda_{\text{cnt}} = \int_{\text{cnt}} \pi \frac{dB_\nu}{dT} \Big|_{T_{\text{cnt}}} \frac{dT_{\text{cnt}}}{dT_s} d\nu. \quad (48)$$

We apply the same logic as for the surface and H<sub>2</sub>O band feedbacks. The derivative  $dT_{\text{cnt}}/dT_s$  can be solved for analytically:  $T_{\text{cnt}}$  has no dependence on  $T_s$  other than through lapse rate changes, so

$$\begin{aligned} \frac{dT_{\text{cnt}}}{dT_s} &= \frac{\partial T_{\text{cnt}}}{\partial \gamma_{\text{lr}}} \frac{d\gamma_{\text{lr}}}{dT_s} \\ &= \frac{T_{\text{cnt}}}{\gamma_{\text{lr}}(2\gamma_{\text{wv}} - a)} \frac{d\gamma_{\text{lr}}}{dT_s}. \end{aligned} \quad (49)$$

One important difference between the continuum and the other feedbacks is that the continuum is transparent across all wavenumbers at low surface temperatures, and only becomes optically

thick at high surface temperatures. We approximate the continuum’s emissivity as  $1 - e^{-\tau_{\text{cnt}}}$ , which correctly captures the limiting behavior of an emitter at small and large optical thickness ( $\tau_{\text{cnt}} \ll 1$  versus  $\tau_{\text{cnt}} \gg 1$ ). The continuum can only dominate the atmosphere’s emission at wavenumbers at which  $\text{CO}_2$  and  $\text{H}_2\text{O}$  absorption are weak, so we set the effective width of the continuum equal to the width of the window region  $\Delta\tilde{\nu}_{\text{surf}}$ , defined above. The continuum feedback is then

$$\begin{aligned}
 -\lambda_{\text{cnt}} &= \int_{\text{cnt}} \pi \frac{dB_\nu}{dT} \Big|_{T_{\text{cnt}}} \frac{dT_{\text{cnt}}}{dT_s} d\nu \\
 &\approx c_{\text{cnt}} \times \pi \frac{dB_{\tilde{\nu}}}{dT} \Big|_{T_{\text{cnt}}} \times \frac{dT_{\text{cnt}}}{dT_s} \times \Delta\tilde{\nu}_{\text{surf}} (1 - e^{-\tau_{\text{cnt}}})
 \end{aligned} \tag{50}$$

where  $c_{\text{cnt}}$  is again a scaling constant. The sign of  $\lambda_{\text{cnt}}$  is positive because the bulk lapse rate decreases with warming,  $d\gamma_{\text{lr}}/dT_s < 0$ . As discussed above, this means the  $\text{H}_2\text{O}$  continuum acts as a positive/destabilizing feedback and has the opposite sign of the negative/stabilizing  $\text{H}_2\text{O}$  band feedback.

### e. $\text{CO}_2$ band feedback

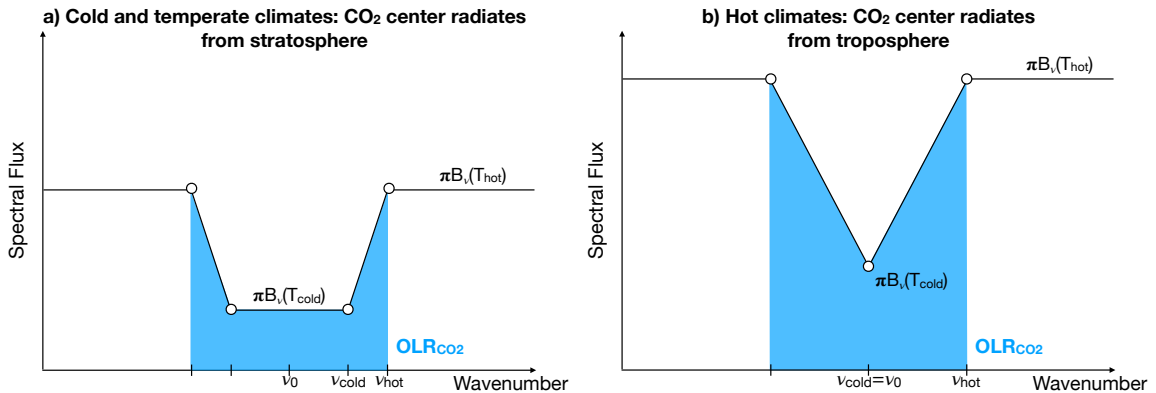


FIG. 6. A  $\text{CO}_2$  “ditch” model: the  $\text{CO}_2$  band emits  $\pi B_\nu(T_{\text{cold}})$  in its center, its flanks emit  $\pi B_\nu(T_{\text{hot}})$ , and the slopes in-between are approximated as linear and symmetric. Shaded blue area is the OLR contribution from the  $\text{CO}_2$  band. Left: In cold climates or at high  $\text{CO}_2$  abundances the  $\text{CO}_2$  band center radiates from the stratosphere. Right: In hot climates or at low  $\text{CO}_2$  abundances the  $\text{CO}_2$  band center radiates from the troposphere.

Next, we consider the  $\text{CO}_2$  feedback. Unlike the  $\text{H}_2\text{O}$  band and continuum, however, the emission temperature of  $\text{CO}_2$  varies strongly with wavenumber, which makes it difficult to approximate the

CO<sub>2</sub> feedback integral via simple multiplication. Instead we introduce an idealized CO<sub>2</sub> "ditch" model, illustrated in Figure 6. Our approach is closely related to the CO<sub>2</sub> forcing models of Wilson and Gea-Banacloche (2012) and Jeevanjee et al. (2021b) – in Appendix A we show that our ditch model can also be used to rederive the results of those previous studies, underlining the close relationship between forcing and feedbacks.

We approximate the CO<sub>2</sub> band as symmetric around the central frequency  $\nu_0 = 667 \text{ cm}^{-1}$ . The center of the band emits  $\pi B_\nu(T_{\text{cold}})$  while outside the band the emission is  $\pi B_\nu(T_{\text{hot}})$ . Here  $T_{\text{cold}}$  and  $T_{\text{hot}}$  are cold and hot emission temperatures, while  $\nu_{\text{hot}}$  and  $\nu_{\text{cold}}$  denote the edges of the CO<sub>2</sub> ditch. At low and moderate surface temperatures the CO<sub>2</sub> band center around  $667 \text{ cm}^{-1}$  radiates from the stratosphere, so  $T_{\text{cold}}$  is equal to the stratospheric temperature. However, this situation is no longer true at high surface temperatures. Physically, the tropopause rises as the surface warms, so if one warms the surface while holding CO<sub>2</sub> concentration fixed (this is implicit in the definition of a climate feedback), parts of the CO<sub>2</sub> band that were previously in the stratosphere have to start radiating from the troposphere. Eventually, even the CO<sub>2</sub> band center radiates from the troposphere so the rectangular CO<sub>2</sub> ditch turns into a triangular trough (see Fig. 6b). Here we leave our expressions general to allow for either situation.

The CO<sub>2</sub> band is relatively narrow, so we can neglect the wavenumber-dependence of the Planck function and evaluate it at the center of the CO<sub>2</sub> band,  $\pi B_\nu(T) \approx \pi B_{\nu_0}(T)$ . Treating the slopes of the CO<sub>2</sub> ditch as piecewise-linear, the OLR from the CO<sub>2</sub> band is then simply the blue area under the ditch in Figure 6a,

$$\begin{aligned} \text{OLR}_{\text{CO}_2} &= 2 \int_{\nu_0}^{\nu_{\text{hot}}} \pi B_{\nu_0}(T_{\text{CO}_2}) d\nu \\ &= [\pi B_{\nu_0}(T_{\text{hot}}) + \pi B_{\nu_0}(T_{\text{cold}})] (\nu_{\text{hot}} - \nu_{\text{cold}}) + 2\pi B_{\nu_0}(T_{\text{cold}})(\nu_{\text{cold}} - \nu_0). \end{aligned} \quad (51)$$

The OLR change in response to some climate perturbation is

$$\begin{aligned} \Delta \text{OLR}_{\text{CO}_2} &= \text{OLR}'_{\text{CO}_2} - \text{OLR}_{\text{CO}_2} \\ &= [\pi B_{\nu_0}(T'_{\text{hot}}) + \pi B_{\nu_0}(T'_{\text{cold}})] (\nu'_{\text{hot}} - \nu'_{\text{cold}}) - [\pi B_{\nu_0}(T_{\text{hot}}) + \pi B_{\nu_0}(T_{\text{cold}})] (\nu_{\text{hot}} - \nu_{\text{cold}}) + \\ &\quad 2\pi B_{\nu_0}(T'_{\text{cold}})(\nu'_{\text{cold}} - \nu_0) - 2\pi B_{\nu_0}(T_{\text{cold}})(\nu_{\text{cold}} - \nu_0), \end{aligned} \quad (52)$$

where primes indicate perturbed variables. For the CO<sub>2</sub> band feedback the relevant perturbation is a change in surface temperature  $\Delta T_s$ , while for the forcing the relevant perturbation is a change in  $q_{\text{CO}_2}$  (see Appendix A). If  $\Delta T_s$  is small enough we can series expand and drop higher-order terms. For example, the perturbation of the emission at the CO<sub>2</sub> band edge is

$$\pi B_{\nu_0}(T'_{\text{hot}}) = \pi B_{\nu_0}(T_{\text{hot}}) + \pi \left. \frac{dB_{\nu_0}}{dT} \right|_{T_{\text{hot}}} \frac{dT_{\text{hot}}}{dT_s} \Delta T_s,$$

with similar expressions for  $T'_{\text{cold}}$ ,  $\nu'_{\text{cold}}$ , and  $\nu'_{\text{cold}}$ . Plugging back into Equation 52, the feedback of the CO<sub>2</sub> ditch is

$$\begin{aligned} -\lambda_{\text{CO}_2} &= \lim_{\Delta T_s \rightarrow 0} \frac{\Delta \text{OLR}_{\text{CO}_2}}{\Delta T_s} \\ &= \left[ \pi \left. \frac{dB_{\nu_0}}{dT} \right|_{T_{\text{hot}}} \frac{dT_{\text{hot}}}{dT_s} + \pi \left. \frac{dB_{\nu_0}}{dT} \right|_{T_{\text{cold}}} \frac{dT_{\text{cold}}}{dT_s} \right] (\nu_{\text{hot}} - \nu_{\text{cold}}) \\ &\quad + [\pi B_{\nu_0}(T_{\text{hot}}) + \pi B_{\nu_0}(T_{\text{cold}})] \left( \frac{d\nu_{\text{hot}}}{dT_s} - \frac{d\nu_{\text{cold}}}{dT_s} \right) \\ &\quad + 2\pi \left. \frac{dB_{\nu_0}}{dT} \right|_{T_{\text{cold}}} \frac{dT_{\text{cold}}}{dT_s} (\nu_{\text{cold}} - \nu_0) + 2B_{\nu_0}(T_{\text{cold}}) \frac{d\nu_{\text{cold}}}{dT_s}. \end{aligned} \quad (53)$$

Equation 53 gives the most general expression for the feedback of the CO<sub>2</sub> ditch. Geometrically, the blue area under the CO<sub>2</sub> ditch changes if the flanks and center rise while the edges remain fixed (terms proportional to  $dT_{\text{hot}}/dT_s$  and  $dT_{\text{cold}}/dT_s$ ), or if the edges move while the flanks and center of the ditch remain fixed (terms proportional to  $d\nu_{\text{hot}}/dT_s$  and  $d\nu_{\text{cold}}/dT_s$ ). To evaluate Equation 53 we thus need to specify how the parameters  $T_{\text{hot}}$ ,  $T_{\text{cold}}$ ,  $\nu_{\text{hot}}$  and  $\nu_{\text{cold}}$  vary as a function of surface temperature.

At cold surface temperatures we again ignore H<sub>2</sub>O absorption around the CO<sub>2</sub> band so  $T_{\text{hot}} = T_s$ . Similarly, the tropopause is low and the CO<sub>2</sub> band center radiates from the stratosphere, so  $T_{\text{cold}} = T_{\text{strat}}$  and  $dT_{\text{cold}}/dT_s = 0$ . As in Section 5a, we find the band edges  $\nu_{\text{hot}}$  and  $\nu_{\text{cold}}$  by solving  $T_{\text{CO}_2}(\nu_{\text{hot}}) = T_s$  and  $T_{\text{CO}_2}(\nu_{\text{cold}}) = T_{\text{strat}}$ . The results are  $\nu_{\text{hot}} = \nu_0 + l_\nu \log[\tau_{\text{CO}_2}^*(\nu_0)q_{\text{CO}_2}]$ , and  $\nu_{\text{cold}} = \nu_0 + l_\nu \log[\tau_{\text{CO}_2}^*(\nu_0)q_{\text{CO}_2}(T_{\text{strat}}/T_s)^{2/\gamma_{\text{tr}}}]$ . We can see that the hot CO<sub>2</sub> band edge does not change under surface warming,  $d\nu_{\text{hot}}/dT_s = 0$ , while the sensitivity of the cold or stratospheric

band edge to surface warming is

$$\begin{aligned}\frac{d\nu_{\text{cold}}}{dT_s} &= \left. \frac{\partial \nu_{\text{cold}}}{\partial T_s} \right|_{\gamma_{\text{lr}}} + \left. \frac{\partial \nu_{\text{cold}}}{\partial \gamma_{\text{lr}}} \right|_{T_s} \frac{d\gamma_{\text{lr}}}{dT_s} \\ &= -\frac{2l_\nu}{\gamma_{\text{lr}} T_s} + \frac{2l_\nu}{\gamma_{\text{lr}}^2} \log\left(\frac{T_s}{T_{\text{strat}}}\right) \frac{d\gamma_{\text{lr}}}{dT_s}.\end{aligned}\quad (54)$$

The lapse rate change  $d\gamma_{\text{lr}}/dT_s$  is always negative, so the portion of the CO<sub>2</sub> band inside the stratosphere shrinks,  $d\nu_{\text{cold}}/dT_s < 0$ . Geometrically, since  $\nu_{\text{hot}}$  stays fixed while  $\nu_{\text{cold}}$  moves towards the center of the CO<sub>2</sub> band, the CO<sub>2</sub> band slope becomes shallower and the blue area under the CO<sub>2</sub> ditch increases – an OLR increase, or a stabilizing feedback. Physically, this is a simple consequence of a rising tropopause. As the surface warms, the tropopause moves to lower pressures, thus moving more of CO<sub>2</sub>'s emission from the cold stratosphere into the warmer tropopause. Plugging back into Equation 53, the CO<sub>2</sub> band feedback at cold surface temperatures is

$$\begin{aligned}-\lambda_{\text{CO}_2}^{\text{cool}} &= \pi \left. \frac{dB_{\nu_0}}{dT} \right|_{T_s} \frac{2}{\gamma_{\text{lr}}} \log\left(\frac{T_s}{T_{\text{strat}}}\right) + \left[ \pi B_{\nu_0}(T_s) - \pi B_{\nu_0}(T_{\text{strat}}) \right] \\ &\quad \times \left( \frac{2l_\nu}{\gamma_{\text{lr}} T_s} - \frac{2l_\nu}{\gamma_{\text{lr}}^2} \log\left(\frac{T_s}{T_{\text{strat}}}\right) \frac{d\gamma_{\text{lr}}}{dT_s} \right)\end{aligned}\quad (55)$$

At high surface temperatures the CO<sub>2</sub> band center moves into the tropopause and the rectangular ditch turns into a triangle (see lower left in Fig. 4, and sketch in Fig. 6b). We set  $\nu_{\text{cold}} = \nu_0$ , where the central wavenumber  $\nu_0$  is set by the spectroscopic properties of CO<sub>2</sub> and so is fixed under surface warming ( $d\nu_{\text{cold}}/dT_s = 0$ ). The emission temperature in the center of the CO<sub>2</sub> band is now  $T_{\text{cold}} = T_{\text{CO}_2}(\nu_0)$ , where  $T_{\text{CO}_2}$  is the emission temperature of CO<sub>2</sub> (Eqn. 26a). The crucial difference between high and low surface temperatures is that once the CO<sub>2</sub> band center moves into the tropopause  $T_{\text{cold}}$  is no longer constant,

$$\begin{aligned}\frac{dT_{\text{CO}_2}(\nu_0)}{dT_s} &= \left. \frac{\partial T_{\text{CO}_2}(\nu_0)}{\partial T_s} \right|_{\gamma_{\text{lr}}} + \left. \frac{\partial T_{\text{CO}_2}(\nu_0)}{\partial \gamma_{\text{lr}}} \right|_{T_s} \frac{d\gamma_{\text{lr}}}{dT_s} \\ &= \frac{T_{\text{CO}_2}(\nu_0)}{T_s} - \frac{T_{\text{CO}_2}(\nu_0)}{2} \log[q_{\text{CO}_2} \tau_{\text{CO}_2}^*(\nu_0)] \frac{d\gamma_{\text{lr}}}{dT_s}.\end{aligned}\quad (56)$$

The outer edges of the CO<sub>2</sub> band at high temperatures are set by water vapor absorption,  $T_{\text{hot}} = \min[T_{\text{H}_2\text{O}}(\nu_0), T_{\text{cnt}}]$ . We treat H<sub>2</sub>O as Simpsonian, so  $dT_{\text{hot}}/dT_s \approx 0$ , and also ignore non-Simpsonian shifts in the outer CO<sub>2</sub> band edge,  $d\nu_{\text{hot}}/dT_s \approx 0$ . Plugging back into Equation 53, the feedback at high surface temperatures is then

$$\begin{aligned} -\lambda_{\text{CO}_2}^{\text{hot}} &= \pi \left. \frac{dB_{\nu_0}}{dT} \right|_{T_{\text{cold}}} \frac{dT_{\text{cold}}}{dT_s} (\nu_{\text{hot}} - \nu_{\text{cold}}) \\ &= \pi \left. \frac{dB_{\nu_0}}{dT} \right|_{T_{\text{cold}}} \frac{dT_{\text{cold}}}{dT_s} l_{\nu} \log \left[ \tau_{\text{CO}_2}^*(\nu_0) q_{\text{CO}_2} \left( \frac{T_{\text{hot}}}{T_s} \right)^{\frac{2}{\gamma_{\text{tr}}}} \right]. \end{aligned} \quad (57)$$

Geometrically, the behavior of the CO<sub>2</sub> band at high temperatures is dictated by the rise in the center of the band,  $dT_{\text{cold}}/dT_s$ . Since the band center emits more in response to surface warming,  $dT_{\text{cold}}/dT_s > 0$ , the blue area under the triangular ditch goes up – again, an OLR increase, which leads to a stabilizing feedback. Physically, once the center of the CO<sub>2</sub> band radiates from inside the troposphere, we have  $dT_{\text{cold}}/dT_s \propto -d\gamma_{\text{tr}}/dT_s$ , which means the rate at which emission increases is highly sensitive to the rate at which the upper atmosphere warms via the changing lapse rate.

Finally, when does the CO<sub>2</sub> band center change from a stratospheric radiator at low  $T_s$  to a tropospheric radiator at high  $T_s$ , which also determines the transition between  $\lambda_{\text{CO}_2}^{\text{cool}}$  and  $\lambda_{\text{CO}_2}^{\text{hot}}$ ? Based on line-by-line calculations with 400 ppm of CO<sub>2</sub>, Appendix B shows that the smoothed emission temperature in the CO<sub>2</sub> band center moves out of the stratosphere at surface temperatures above 310 K. We therefore identify 310 K as the transition point between the low-temperature and high-temperature CO<sub>2</sub> feedback regimes. Note, however, that this value also depends on CO<sub>2</sub> concentration.

Multiplying the low-temperature regime with a scaling constant  $c_{\text{CO}_2}$ , similar to our other spectral feedbacks, the overall CO<sub>2</sub> band feedback is thus

$$\lambda_{\text{CO}_2} = \begin{cases} c_{\text{CO}_2} \times \lambda_{\text{CO}_2}^{\text{cool}} & \text{if } T_s \leq 310 \text{ K} \\ \lambda_{\text{CO}_2}^{\text{hot}} + b & \text{if } T_s > 310 \text{ K.} \end{cases} \quad (58)$$

where we choose the constant  $b$  to ensure that  $\lambda_{\text{CO}_2}$  remains continuous at 310 K (in practice  $b$  is always of order unity,  $b \sim 0.5$ ).

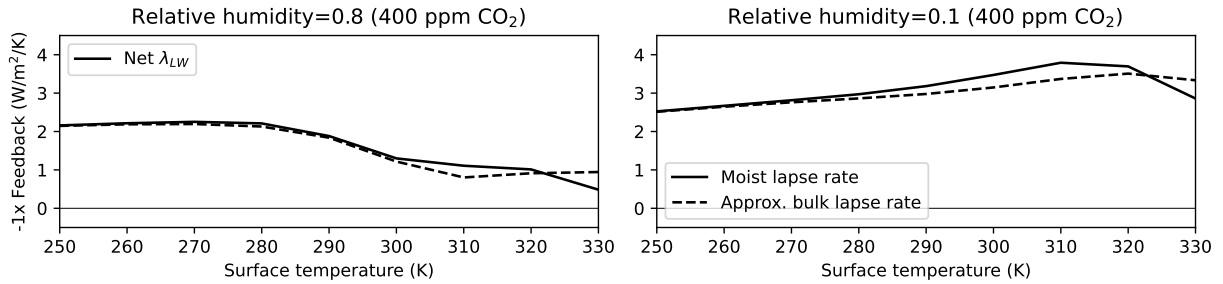


FIG. 7. The impact of the bulk lapse rate approximation on longwave feedbacks is modest below  $\sim 320$  K, but becomes significant at high temperatures. Solid lines are numerical feedbacks calculated assuming the atmosphere follows a moist adiabatic profile, dashed lines are numerical feedbacks calculated assuming the atmosphere follows our bulk lapse rate approximation.

#### f. Validation against LBL calculations

To test our analytic feedback expressions we again use 1D calculations with PyRADS. One potential issue is that our derivations use the bulk lapse rate approximation, and so might differ from realistic feedbacks. Figure 7 compares feedbacks calculated with a moist adiabat to feedbacks with bulk lapse rate profiles. Overall, the bulk lapse rate approximation only introduces minor errors in  $\lambda_{LW}$  over the temperature range 250 – 320 K. We therefore consider the bulk lapse rate approximation sufficiently accurate below 320 K, while care should be taken when applying our analytic expressions to extremely hot climates. To better match the derivations, the PyRADS calculations here also use vertical profiles with a bulk lapse rate, so  $T = T_s (p/p_s)^{\gamma_{lr}}$ . We explore the surface temperature-dependence of spectral feedbacks at high and low relative humidity (RH=0.8 and RH=0.1), without CO<sub>2</sub> and with 400 ppm of CO<sub>2</sub>, for four sets of calculations in total.

To compare our analytic expressions against the 1D calculations we need to specify the scaling constants  $c_{\text{surf}}$ ,  $c_{\text{H}_2\text{O}}$ ,  $c_{\text{cnt}}$ , and  $c_{\text{CO}_2}$ . We pick these constants to match the 1D calculations at RH=0.8 and 400 ppm of CO<sub>2</sub>. The temperature-dependence varies significantly between different feedbacks, so we choose  $c_{\text{surf}}$  to match  $\lambda_{\text{surf}}$  at low temperatures ( $T_s = 250$  K),  $c_{\text{cnt}}$  to match  $\lambda_{\text{cnt}}$  at high temperatures ( $T_s = 330$  K), and  $c_{\text{H}_2\text{O}}$  and  $c_{\text{CO}_2}$  to match  $\lambda_{\text{H}_2\text{O}}$  and  $\lambda_{\text{CO}_2}$  around Earth’s present-day mean temperature ( $T_s = 290$  K). Table 1 gives the resulting values for the above 1D calculations with bulk lapse rates, and for another set of 1D calculations with moist lapse rates. In agreement with Figure 7, the scaling constants vary little between the two sets of calculations.



In this Section we choose the scaling constants to match the idealized 1D calculations with bulk lapse rates, while Section 6 considers a feedback calculation specifically for present-day Earth, and so uses the scaling constants that match the moist adiabatic calculations. Regardless of the exact values, the scaling constants are always of order unity.

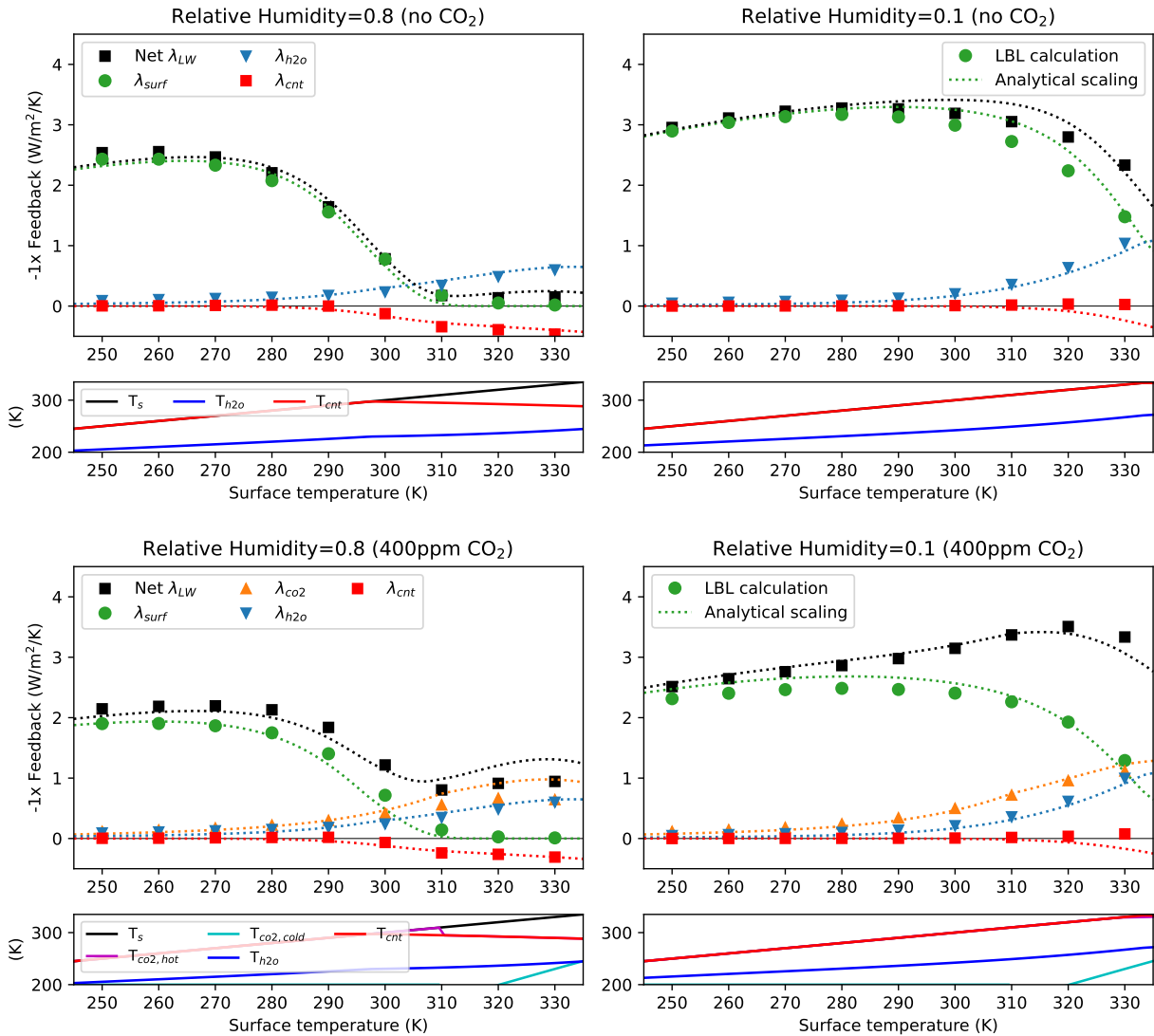


FIG. 8. Spectral feedbacks calculated using PyRADs and assuming a bulk lapse rate (symbols), compared against the analytic scalings (lines). Top row shows calculations without  $\text{CO}_2$ , bottom row with 400ppm of  $\text{CO}_2$ . The large panels show feedbacks while small panels show the corresponding analytic emission temperatures.

Figure 8 shows that our analytic expressions successfully capture the basic state-dependence of  $\lambda_{LW}$  as well as of its spectral constituents. The longwave feedback  $\lambda_{LW}$  is sensitive to changes in

surface temperature, but it also varies in response to humidity and CO<sub>2</sub> changes. Comparing the left and right columns in Figure 8,  $\lambda_{LW}$  becomes larger with decreasing relative humidity (also see McKim et al. 2021). Comparing the top and bottom rows, adding CO<sub>2</sub> to an atmosphere without any CO<sub>2</sub> evens out the temperature-dependence of  $\lambda_{LW}$ , by decreasing  $\lambda_{LW}$  at cold temperatures and increasing  $\lambda_{LW}$  at high temperatures. Importantly, the analytic expressions capture most of the variation in  $\lambda_{LW}$ , including its state-dependence.

To understand the behavior of  $\lambda_{LW}$  we turn to the individual spectral feedbacks. The surface feedback  $\lambda_{\text{surf}}$  is generally the dominant term in the spectral decomposition. Without CO<sub>2</sub>,  $\lambda_{\text{surf}}$  makes up at least 90% of  $\lambda_{LW}$  below 300 K. The presence of CO<sub>2</sub> decreases  $\lambda_{\text{surf}}$  but even in this case  $\lambda_{\text{surf}}$  makes up at least 60% of  $\lambda_{LW}$  below 300 K. Our analytic expressions thus agree with previous studies which showed that Earth’s longwave feedback is dominated by the surface feedback (Koll and Cronin 2018; Raghuraman et al. 2019). This situation changes at high temperatures, however, once the surface window closes, at which point  $\lambda_{LW}$  becomes dominated by atmospheric feedbacks.

In line with Section 4, the CO<sub>2</sub> band feedback acts to stabilize Earth’s climate in warm climates, and its importance increases with surface temperature. Below 300 K,  $\lambda_{\text{CO}_2}$  contributes less than 20% of the total feedback, but its magnitude grows rapidly with surface temperature such that at 330 K and high relative humidity  $\lambda_{\text{CO}_2}$  makes up almost 70% of  $\lambda_{LW}$ . Interestingly, for large RH  $\lambda_{\text{CO}_2}$  becomes equal to  $\lambda_{\text{surf}}$  at surface temperatures around  $\sim 305$  K. Extrapolating from these 1D calculations to Earth’s spatial feedback pattern, we can expect that Earth’s feedback is dominated by the surface in most regions, but that atmospheric feedbacks become important in the inner tropics – an issue explored in detail in Section 6.

Finally, again in line with our analytic results, the two water vapor feedbacks  $\lambda_{\text{H}_2\text{O}}$  and  $\lambda_{\text{cnt}}$  have opposing signs. At high relative humidity  $\lambda_{\text{H}_2\text{O}}$  and  $\lambda_{\text{cnt}}$  partially cancel. In contrast, at low relative humidity  $\lambda_{\text{cnt}}$  becomes negligible while  $\lambda_{\text{H}_2\text{O}}$  only changes moderately – a non-Simpsonian effect. The different sensitivity to RH arises because the continuum’s optical thickness scales as  $\tau_{\text{cnt}} \propto \text{RH}^2$ , whereas the optical thickness in the water vapor bands only scales as  $\tau_{\text{H}_2\text{O}} \propto \text{RH}$ . Decreases in relative humidity therefore increase  $\lambda_{LW}$  both by increasing the surface feedback  $\lambda_{\text{surf}}$  and by reducing  $\lambda_{\text{cnt}}$ , so that H<sub>2</sub>O acts as a net stabilizing feedback. Comparing  $\lambda_{\text{H}_2\text{O}}$  and  $\lambda_{\text{CO}_2}$  at present-day CO<sub>2</sub> levels, we see that the two feedbacks are roughly equal in magnitude. Non-

TABLE 2. Summary of main theoretical results.

Emission temperatures	
$T_{\text{CO}_2}(\nu) =$	$T_s \left( \frac{1}{\tau_{\text{CO}_2}^*(\nu) q_{\text{CO}_2}} \right)^{\gamma_{\text{IR}}/2}$
$T_{\text{H}_2\text{O}}(\nu) =$	$T_0 \left( \frac{1+\gamma_{\text{WV}}\gamma_{\text{IR}}}{\tau_{\text{H}_2\text{O}}^*(\nu)\text{RH}} \right)^{\frac{\gamma_{\text{IR}}}{1+\gamma_{\text{WV}}\gamma_{\text{IR}}}} \left( \frac{T_s}{T_0} \right)^{\frac{1}{1+\gamma_{\text{WV}}\gamma_{\text{IR}}}}$
$T_{\text{cnt}} =$	$T_0 \left( \frac{(2\gamma_{\text{WV}}-a)\gamma_{\text{IR}}}{\tau_{\text{cnt}}^*\text{RH}^2} \right)^{\frac{1}{2\gamma_{\text{WV}}-a}}$
Feedbacks	
$-\lambda_{\text{surf}} =$	$c_{\text{surf}} \times \pi \frac{dB_{\tilde{\nu}}}{dT} \Big _{T_s} \Delta\tilde{\nu}_{\text{surf}} e^{-\tau_{\text{cnt}}}$
$-\lambda_{\text{H}_2\text{O}} =$	$c_{\text{H}_2\text{O}} \times \pi \frac{dB_{\tilde{\nu}}}{dT} \Big _{T_{\text{H}_2\text{O}}(\tilde{\nu})} \times \frac{dT_{\text{H}_2\text{O}}(\tilde{\nu})}{dT_s} \times \Delta\nu_{\text{H}_2\text{O}}$
$-\lambda_{\text{cnt}} =$	$c_{\text{cnt}} \times \pi \frac{dB_{\tilde{\nu}}}{dT} \Big _{\tilde{\nu}, T_{\text{cnt}}} \times \frac{dT_{\text{cnt}}}{dT_s} \times \Delta\tilde{\nu}_{\text{surf}} (1 - e^{-\tau_{\text{cnt}}})$
$-\lambda_{\text{CO}_2} =$	$\begin{cases} c_{\text{CO}_2} \times \frac{2\pi}{\gamma_{\text{IR}}} \frac{dB_{\nu_0}}{dT} \Big _{T_s} \log\left(\frac{T_s}{T_{\text{strat}}}\right) - [\pi B_{\nu_0}(T_s) - \pi B_{\nu_0}(T_{\text{strat}})] \times \frac{d\nu_{\text{cold}}}{dT_s} & \text{at low } T_s \\ \pi \frac{dB_{\nu_0}}{dT} \Big _{T_{\text{cold}}} \frac{dT_{\text{cold}}}{dT_s} (\nu_{\text{hot}} - \nu_{\text{cold}}) + b & \text{at high } T_s \end{cases}$

Simpsonian H<sub>2</sub>O effects are thus about as important as the CO<sub>2</sub> band for Earth's current longwave feedback.

## 6. The Spatial Pattern of $\lambda_{LW}$

In the previous two sections we demonstrated that the analytic expressions summarized in Table 2 accurately capture the behavior of Earth's emission temperature  $T_{\text{rad}}$  as well as the state-dependence of  $\lambda_{LW}$ . These feedback expressions can be interpreted as either a model for the global-mean feedback or as a model for the local feedback of an isolated atmospheric column, so the state-dependence of  $\lambda_{LW}$  shown in Figure 8 should also appear as a spatial-dependence in Earth's clear-sky longwave feedback.

In this section we therefore analyze the spatial pattern of  $\lambda_{LW}$  for Earth's present-day climate. First, we generate a map of  $\lambda_{LW}$  using the radiative kernel technique (Soden et al. 2008). Next, we generate a map of  $\lambda_{LW}$  using our analytic expressions. The radiative kernel technique cannot be used to determine the feedback contributions of individual gases and our analytic expressions only account for the feedback from Earth's dominant greenhouse gases, H<sub>2</sub>O and CO<sub>2</sub>, whereas the radiative kernel includes additional greenhouse gases such as O<sub>3</sub> and CH<sub>4</sub>. We therefore

split  $\lambda_{LW}$  into only two terms, namely the surface feedback  $\lambda_{surf}$  and the atmospheric feedback  $\lambda_{atm} = \lambda_{LW} - \lambda_{surf}$ . Despite the idealizations in our analytic approach compared to a full radiative kernel, we find that the resulting feedback maps are in qualitative agreement. This allows us to attribute the spatial pattern of  $\lambda_{LW}$ , as deduced from the radiative kernel, to geographic variations in the inputs of our analytic model.

#### *a. Inputs for feedback maps*

For the kernel calculation we use the HadGEM2 radiative kernel. For consistency with the analytic model (which assumes the stratosphere is isothermal and at a fixed temperature), we set the kernel to zero in the stratosphere. The tropopause is defined as in Soden et al. (2008): the tropopause pressure  $p_{tp}$  increases linearly with latitude, from 0.1 bar at the equator to 0.3 bar at the poles. The analytic model also assumes RH stays fixed under surface warming, so we do not include RH changes in the kernel calculation. Doing so is justified because the RH feedback only makes a minor contribution to  $\lambda_{LW}$  in individual climate models, and it moreover tends to cancel in the multi-model mean (Zelinka et al. 2020). To compute the forced response we use HadGEM2 climatologies from the CMIP5 archive for a preindustrial control simulation and an abrupt-4xCO<sub>2</sub> simulation, where the climatologies are 50-year averages (for 4xCO<sub>2</sub>, years 100-150 after increasing CO<sub>2</sub>). Multiplying the kernel with the forced response gives a map of the change in top-of-atmosphere (TOA) radiation (Soden et al. 2008). To compute a feedback one additionally needs to normalize the change in TOA radiation by a change in surface temperature. Consistent with our assumption of an isolated atmospheric column we compute local-local feedback maps, that is, we divide the local change in OLR deduced from the kernel by the local change in surface temperature (Feldl and Roe 2013; Armour et al. 2013; Bloch-Johnson et al. 2020). To distinguish between surface and atmospheric feedbacks in the kernel method we compute the clear-sky longwave feedback  $\lambda_{LW}$  and the surface feedback  $\lambda_{surf}$ , where the second is equal to the surface kernel; the atmospheric feedback is then computed as the residual  $\lambda_{atm} = \lambda_{LW} - \lambda_{surf}$ .

We compare the kernel-derived feedback maps against maps from our analytic expressions. The surface feedback  $\lambda_{surf}$  is the same as in Section 5, while the atmospheric feedback is the sum over all atmospheric terms  $\lambda_{atm} = \lambda_{CO_2} + \lambda_{H_2O} + \lambda_{cnt}$ . The analytic expressions require six input parameters: CO<sub>2</sub> concentration, surface temperature  $T_s$ , stratosphere temperature  $T_{strat}$ , relative humidity RH,

temperature lapse rate  $\gamma_{lr}$ , and the change in lapse rate under surface warming  $d\gamma_{lr}/dT_s$ . Except for the lapse rate change  $d\gamma_{lr}/dT_s$ , all these inputs can be obtained from a single climate state (here, the HadGEM2 preindustrial state) and do not require knowledge of the climate's forced response. CO<sub>2</sub> is set to be spatially uniform at 400 ppm (results are highly similar if using a preindustrial 285 ppm); the surface temperature  $T_s$  is taken as the air temperature at 2m; and the stratospheric temperature  $T_{strat}$  is set equal to the temperature at the tropopause pressure level,  $T_{strat} = T(p_{tp})$ , where  $p_{tp}$  is defined using via the above tropopause definition of Soden et al. (2008). The relative humidity RH is set equal to the column relative humidity, defined as the ratio between the atmospheric column's water vapor path and its water vapor path at saturation (e.g., Bretherton et al. 2005),

$$RH = \frac{WVP}{WVP^*}, \quad (59)$$

$$= \frac{\int_{p_{tp}}^{p_s} q \, dp/g}{\int_{p_{tp}}^{p_s} q^* \, dp/g}. \quad (60)$$

Here the vertical integral is taken from the tropopause  $p_{tp}$  down to the surface to exclude the strongly sub-saturated stratosphere. One could in principle also approximate RH using other measures of atmospheric humidity; however, the column relative humidity is a natural choice because it correctly captures the atmosphere's total water vapor path, which in turn determines the width of the window region and  $\lambda_{surf}$ .

Next, the lapse rate  $\gamma_{lr} = d\ln T/d\ln p$  varies strongly in the vertical. We compute a bulk lapse rate using a mass-weighted vertical average,

$$\gamma_{lr} = \frac{1}{p_1 - p_{tp}} \int_{p_{tp}}^{p_1} \frac{p}{T} \frac{dT}{dp} dp, \quad (61)$$

where the average is taken from the tropopause  $p_{tp}$  down to a near-surface pressure  $p_1$ . Some polar regions have such strong surface inversions that the inferred bulk lapse rate becomes negative, whereas our derivations break down if  $\gamma_{lr} < 0$ . At the same time, the map of  $\gamma_{lr}$  should reflect near-surface inversions over subtropical eastern ocean basins and deep boundary layers over tropical land, discussed below. We therefore define  $p_1$  similar to  $p_{tp}$ , as varying linearly in latitude from  $p_1 = 1$  bar at the equator to  $p_1 = 0.85$  bar at the poles. One could also evaluate  $\gamma_{lr}$  using the bulk lapse rate definition from Equation 6 in combination with a tropopause definition; however,

this approach makes the inferred lapse rates quite sensitive to the tropopause definition, which we side-step by using the mass-weighted average in Equation 61 instead. Finally, the only input in our analytic expressions that requires information about the climate’s forced response is the change in lapse rate  $d\gamma_{lr}/dT_s$ , which is computed using the difference in  $\gamma_{lr}$  between the HadGEM2 4xCO<sub>2</sub> and preindustrial simulations.

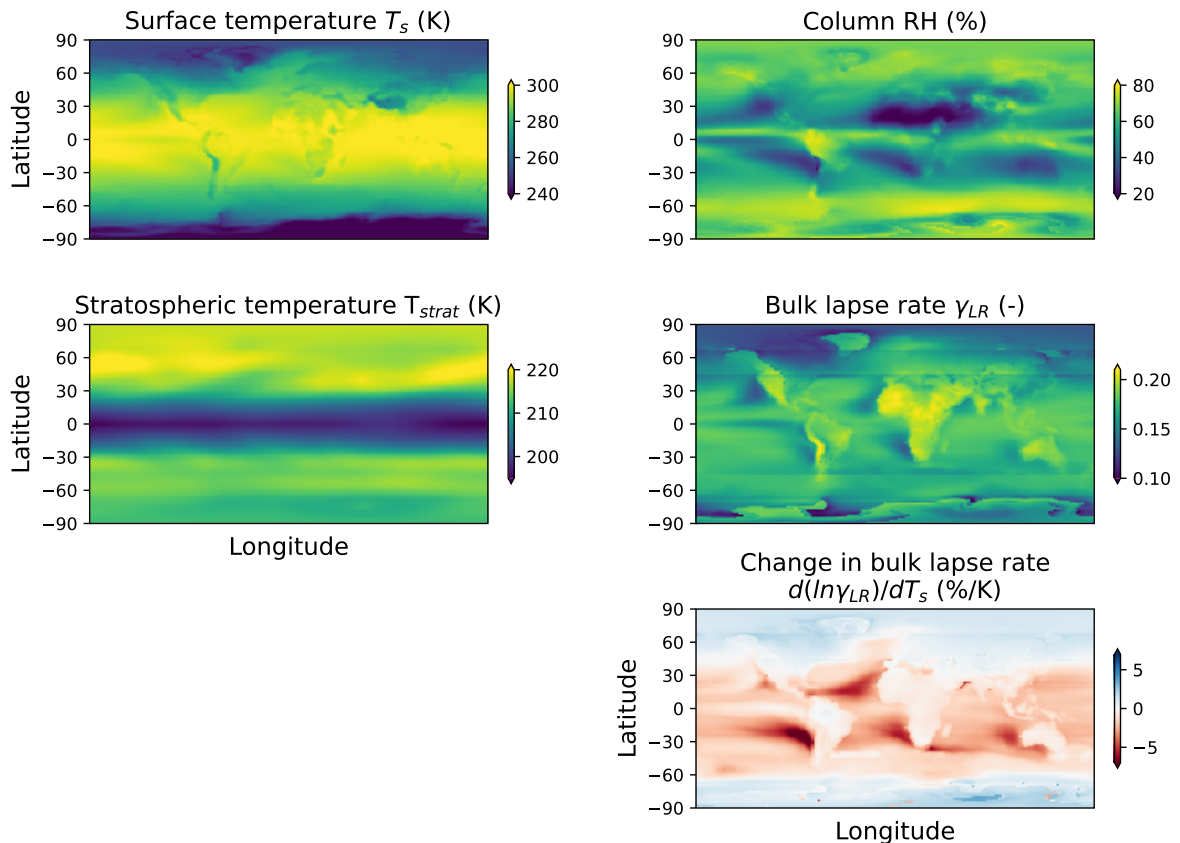


FIG. 9. Input data used to evaluate the analytic feedback maps in Figure 10. The top four panels show fields from a HadGEM2 preindustrial simulation. The bottom right panel shows the normalized bulk lapse rate change  $d\ln(\gamma_{lr})/dT_s$  computed using the HadGEM2 4xCO<sub>2</sub> and preindustrial simulations.

Figure 9 shows maps of the input data from HadGEM2, which we use below to evaluate the analytic expressions. In the top two rows, large variations are notable in the maps of surface temperature  $T_s$ , column relative humidity RH, and bulk lapse rate  $\gamma_{lr}$ . In contrast, apart from minor stationary wave patterns in the northern mid-latitudes, the stratospheric temperature  $T_{strat}$  is zonally fairly uniform and varies by only about 20 K between the equator and poles. The bottom row

shows the normalized bulk lapse change,  $d\ln(\gamma_{lr})/dT_s = 1/(\Delta\gamma_{lr}) \times (\Delta\gamma_{lr}/\Delta T_s)$ , computed using the bulk lapse rate difference  $\Delta\gamma_{lr}$  between 4xCO<sub>2</sub> and preindustrial simulations. The bulk lapse rate change shows an equator-pole contrast, with a decrease in  $\gamma_{lr}$  at low and mid latitudes and an increase in  $\gamma_{lr}$  at high latitudes. This contrast is in line with previous studies – for a moist adiabat the atmospheric temperature-pressure profile becomes less steep under warming, so  $\gamma_{lr}$  decreases in the tropics, while the opposite occurs at high latitudes (e.g., Payne et al. 2015; Cronin and Jansen 2016; Stuecker et al. 2018). There is also a noticeable tropical land-ocean contrast in the bulk lapse-rate change, with tropical land areas showing near-zero lapse-rate change. This is likely due to compensation between moist-adiabatic warming aloft, which is uniform across the tropics and tends to decrease  $\gamma_{lr}$ , and amplified land surface warming, which increases  $\gamma_{lr}$  (Byrne and O’Gorman 2013). Conversely, subtropical eastern ocean basins have the same moist adiabatic warming aloft but *suppressed* surface warming, both of which contribute to strong decreases in  $\gamma_{lr}$ .

### b. Feedback maps

Figure 10 shows the feedback maps resulting from kernel and analytic calculations. Overall, we find good qualitative agreement between kernel-derived feedbacks and our analytic approximations. The global pattern of  $\lambda_{LW}$  in both maps shows clear contrasts between the high latitudes, subtropics, and inner tropics (Fig. 10, top row).  $\lambda_{LW}$  is smallest in the inner tropics, especially in the intertropical convergence zone (ITCZ), while it is largest in the subtropics, especially over eastern ocean basins. The agreement is less good at small scales, with the analytic map of  $\lambda_{LW}$  showing less regional structure and deviating from the kernel-derived map in continental interiors and over the Southern Ocean. This is plausible given the idealizations in our derivations, such as representing realistic vertical temperature profiles by a smooth power-law. However, small-scale differences tend to cancel when taking a zonal or global mean. The zonal-mean of  $\lambda_{LW}$  in our analytic estimate agrees with the zonal-mean of the kernel  $\lambda_{LW}$  to within 11% at each latitude. The global-mean values of  $\lambda_{LW}$  are almost identical, with  $-2.15$  W/m<sup>2</sup>/K for the kernel calculation and  $-2.16$  W/m<sup>2</sup>/K for the analytic estimate. Note that these global mean averages are weighted by the HadGEM2 pattern of surface warming, which is required to convert a local-local feedback map into a global mean (Feldl and Roe 2013; Armour et al. 2013).

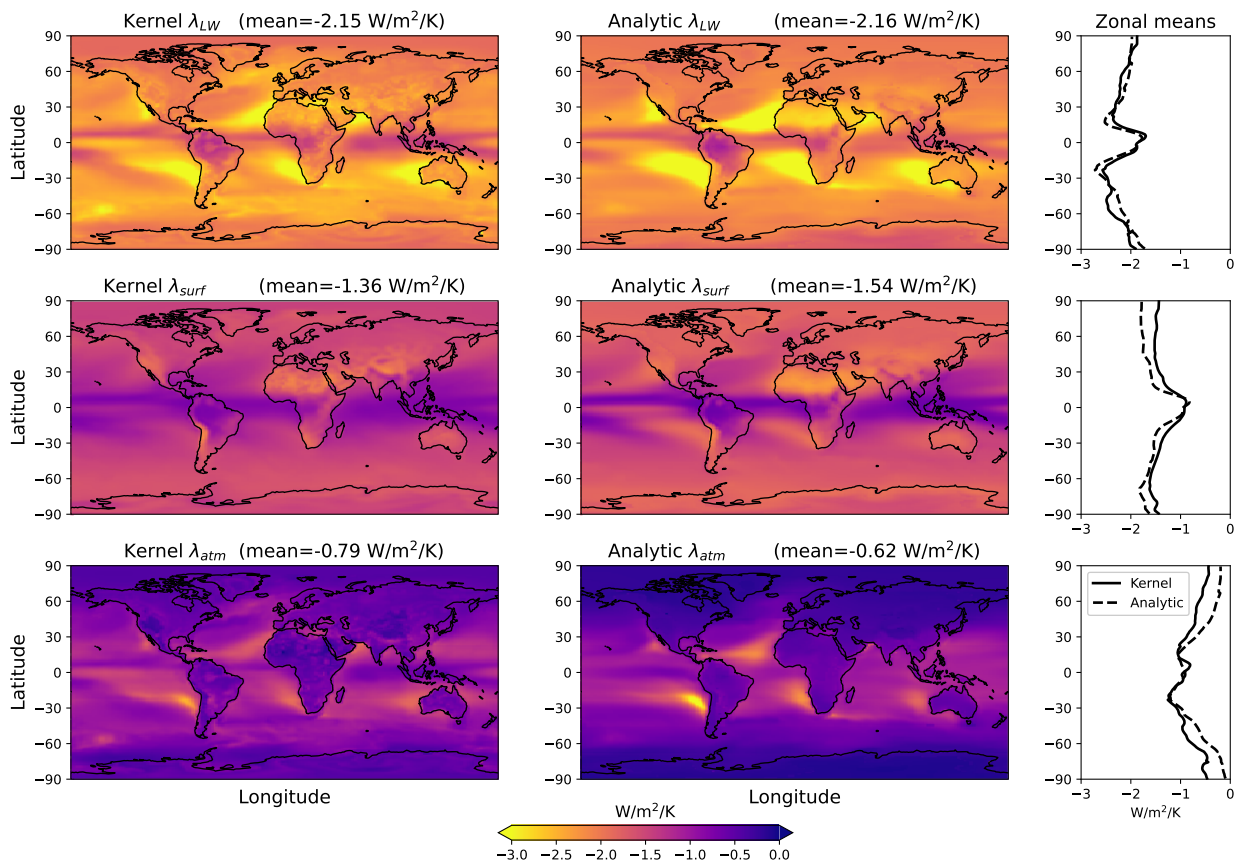


FIG. 10. Feedback maps showing feedbacks computed with a radiative kernel (left column), or with our analytic expressions (middle column). The analytic maps are calculated from the inputs shown in Figure 9. Top row shows the net longwave clear-sky feedback  $\lambda_{LW}$ , middle row the surface component  $\lambda_{surf}$ , and bottom row and the atmospheric component  $\lambda_{atm}$ . Means above each subpanel are area-weighted global means that are weighted by the pattern of surface warming.

The qualitative agreement between the  $\lambda_{LW}$  maps also holds separately for surface and atmospheric feedbacks, though differences are larger here. The kernel-derived map of  $\lambda_{surf}$  is almost uniform at high latitudes, large in magnitude over subtropical desert regions, and small in magnitude over the ITCZ. The analytic map of  $\lambda_{surf}$  qualitatively matches this pattern, though it overpredicts the magnitude of  $\lambda_{surf}$  in the global mean by 0.18  $W/m^2/K$ , or 13%. Conversely, the analytic estimate underpredicts  $\lambda_{atm}$  relative to the kernel-derived map in the global mean by 0.17  $W/m^2/K$ , or 22%. In addition, the analytic  $\lambda_{atm}$  map predicts that the atmospheric feedback goes almost to zero at the poles, whereas the kernel-derived  $\lambda_{atm}$  map shows a small but clearly non-zero feedback. The strong differences at the poles again presumably arise because our derivations fail to capture the



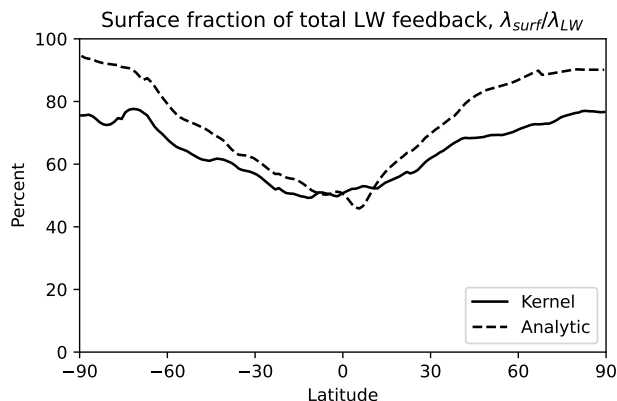


FIG. 11. Zonal mean fraction of the surface feedback to the net feedback,  $\lambda_{\text{surf}}/\lambda_{LW}$ , based on the radiative kernel (solid) and our analytic expressions (dashed).

atmospheric feedback response in areas with inversions and other complex temperature-pressure profiles.

In addition to an overall spatial agreement, both kernel and analytic feedback calculations agree that the surface dominates the net longwave feedback. Figure 11 shows that the surface's contribution to the total feedback is about 50% at low latitudes and increases towards the poles, reaching about 75% in the kernel maps and over 90% in the analytic maps. One plausible reason why the analytic maps tend to overestimate  $\lambda_{\text{surf}}/\lambda_{LW}$  at high latitudes is that our expressions do not include minor greenhouse gases such as ozone or methane. Any additional atmospheric absorption from such gases reduces the window width via  $\Delta\nu_{\text{surf}} \times e^{-\tau_{\text{cnt}}}$  and thus also the surface feedback  $\lambda_{\text{surf}}$  (also see Feng et al. 2022). This effect should be most clearly visible at high latitudes, where water vapor concentrations are low and  $\Delta\nu_{\text{surf}}$  is large, while at low latitudes  $\Delta\nu_{\text{surf}} \times e^{-\tau_{\text{cnt}}}$  is already small due to the water vapor continuum, leaving less room for other greenhouse gases to affect  $\lambda_{\text{surf}}$ . Nevertheless, in line with the results from Section 5, both kernel and analytic maps show that  $\lambda_{LW}$  is dominated by  $\lambda_{\text{surf}}$  across most of the globe. In contrast, atmospheric feedbacks only start to rival  $\lambda_{\text{surf}}$  in the inner tropics and particularly inside the ITCZ (Fig. 10). Our finding agrees with other published estimates: the simple area-weighted global mean of  $\lambda_{\text{surf}}/\lambda_{LW}$  is 60% in our kernel calculation and 67% in our analytic estimate, well in line with the results of Raghuraman et al. (2019) who deduced 63% using a different methodology. Similarly, Feng et al. (2022) found that  $\lambda_{\text{surf}}/\lambda_{LW}$  varies between 88% at the poles to 50% in the tropics, in good agreement with

Figure 11. We conclude that our analytic model of  $\lambda_{LW}$  has notable biases at regional scales but it is sufficient to understand the factors that underlie the large-scale pattern of  $\lambda_{LW}$ , which we turn to next.

c. What controls the large-scale pattern of  $\lambda_{LW}$ ?

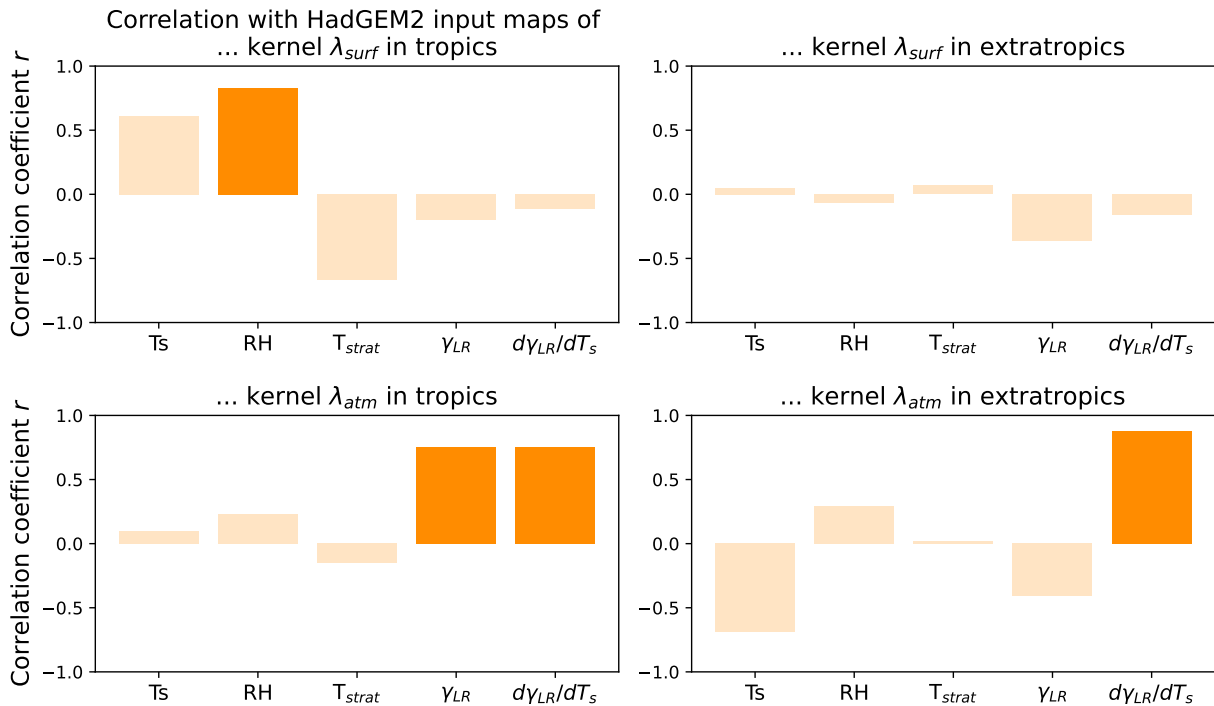


FIG. 12. Spatial correlation between the kernel-derived feedback maps of  $\lambda_{surf}$  and  $\lambda_{atm}$  (Figure 10, left column), and the inputs to our analytic model (Figure 9). Top row shows correlations between inputs and  $\lambda_{surf}$ , bottom row shows correlations between inputs and  $\lambda_{atm}$ . Left column shows correlations inside the tropics, right column shows correlations in the extratropics. Dark colors highlight particularly strong correlations ( $|r| \geq 0.75$ ), while the tropics/extratropics are defined as all points equatorward/poleward of  $30^\circ$  latitude.

The match between our analytic model and the kernel calculation implies that one can explain much of the spatial structure of  $\lambda_{LW}$  in terms of the analytic model's input parameters. We do this by calculating correlations between  $\lambda_{surf}$  and  $\lambda_{atm}$  from the kernel-derived feedback maps against the analytic model's five main inputs: surface temperature  $T_s$ , column relative humidity  $RH$ , stratospheric temperature  $T_{strat}$ , bulk lapse rate  $\gamma_{lr}$ , and the change in bulk lapse rate under

warming  $d\gamma_{lr}/dT_s$ . Spatial CO<sub>2</sub> contrasts are small (e.g., Fraser et al. 1983), and so do not need to be considered here.

Figure 12 shows the resulting spatial correlations between the kernel-derived feedback maps (left column of Figure 10) and the five inputs from HadGEM2 (Figure 9). Because the feedback maps differ strongly between tropics and extratropics in terms of zonal variation and magnitude, we compute correlations separately in these two regions (data are split based on being equatorward or poleward of 30° latitude). Based on the inherent correlations between the five input maps, we consider a correlation significant if its coefficient exceeds  $|r| \geq 0.75$  (the largest intra-input correlations are  $r = -0.71$  between  $T_s$  and  $T_{\text{strat}}$  in the tropics, and  $r = -0.76$  between  $T_s$  and  $d\gamma_{lr}/dT_s$  in the extratropics; not shown).

In line with our analytic model, we find that the kernel-derived  $\lambda_{\text{surf}}$  is strongly correlated with column RH in the tropics ( $r = 0.83$ ), while it does not show strong correlation with any inputs in the extratropics ( $|r| < 0.4$ ). This underlines the importance of the subtropical dry radiator fin regions for  $\lambda_{\text{surf}}$ , which are clearly visible as the dark blue regions in Figure 9 (top right) and the yellow regions in Figure 10 (center left). As expected, the sign of the correlation is positive which means  $\lambda_{\text{surf}}$  becomes less negative, or less stabilizing, as column RH increases.

Next, we find  $\lambda_{\text{atm}}$  is most strongly correlated with  $\gamma_{lr}$  and  $d\gamma_{lr}/dT_s$  in the tropics ( $r = 0.75$  for both), and with  $d\gamma_{lr}/dT_s$  in the extratropics ( $r = 0.88$ ). Of the two parameters that show strong correlations with  $\lambda_{\text{atm}}$  in the tropics,  $\gamma_{lr}$  and  $d\gamma_{lr}/dT_s$ , which one is more important? We performed a test with the analytical model in which we set  $d\gamma_{lr}/dT_s = 0$  (not shown). Doing so eliminates most tropical structure in the map of  $\lambda_{\text{atm}}$ , which indicates that  $\lambda_{\text{atm}}$  is largely determined by  $d\gamma_{lr}/dT_s$ , not  $\gamma_{lr}$ . The correlation between  $\lambda_{\text{atm}}$  and  $d\gamma_{lr}/dT_s$  is positive, which is intuitive:  $\lambda_{\text{atm}}$  becomes more negative if the upper atmosphere warms more relative to the surface, i.e. if  $\gamma_{lr}$  decreases. The spatial variability of  $\lambda_{\text{atm}}$  is largest in the tropics, and can be understood in terms of the map of  $d\gamma_{lr}/dT_s$  already discussed in Section 6a: tropical  $\lambda_{\text{atm}}$  is large over subtropical eastern ocean basins due to suppressed surface warming, and small over land due to enhanced surface warming, where these warming patterns are relative to the approximately uniform warming of the tropical free troposphere (Byrne and O’Gorman 2013).

The correlations shown in Figure 12 are between fields derived from two independent methods, and so are non-trivial. Appendix C shows that the same analysis performed with  $\lambda_{\text{surf}}$  and  $\lambda_{\text{atm}}$

from our analytic feedback maps identifies the same dominant relations (e.g.,  $\lambda_{\text{surf}}$  is most strongly correlated with column RH in the tropics), though most correlation coefficients are unsurprisingly even larger (e.g.,  $r = 0.93$  for the analytic  $\lambda_{\text{surf}}$  and tropical column RH). Our results thus underline that the spatial pattern of  $\lambda_{LW}$  can be understood, at least in rough terms and on large spatial scales, by Earth's spatial pattern of relative humidity and lapse rate changes. Relative humidity and lapse rate changes dominate the pattern of  $\lambda_{LW}$  in the tropics, where they control  $\lambda_{\text{surf}}$  and  $\lambda_{\text{atm}}$  respectively, while lapse rate changes dominate the pattern of  $\lambda_{\text{atm}}$  in the extratropics.

## 7. Discussion & Conclusions

In this paper we have presented a novel decomposition of Earth's clear-sky longwave feedback  $\lambda_{LW}$  into four spectral components, namely a surface Planck feedback ( $\lambda_{\text{surf}}$ ) and three atmospheric feedbacks: a CO<sub>2</sub> band feedback ( $\lambda_{\text{CO}_2}$ ), a (non-Simpsonian) water vapor band feedback ( $\lambda_{\text{H}_2\text{O}}$ ), and a destabilizing water vapor continuum feedback ( $\lambda_{\text{cnt}}$ ). We have derived simple analytic expressions for each of these spectral feedbacks, which accurately reproduce the results of line-by-line calculations and qualitatively match the feedback map computed from a radiative kernel. In principle one could extend this approach even further to account for additional complicating factors, such as the effect of additional greenhouse gases or a more realistic stratosphere. However, our results already show that from a radiative perspective the factors determining  $\lambda_{LW}$  can be understood fairly easily, adding further support to the close agreement between observations and climate models.

The picture of Earth's clear-sky longwave feedback that emerges from this perspective is relatively simple, consisting of a surface feedback plus atmospheric feedbacks from CO<sub>2</sub> and H<sub>2</sub>O. At present the surface feedback  $\lambda_{\text{surf}}$  is the most important contributor in the global-mean and at most latitudes, with its spatial pattern determined by the distribution of atmospheric water vapor.  $\lambda_{\text{surf}}$  is largest in the dry subtropics, consistent with the view that these are the locus of Earth's stabilizing longwave feedback (Pierrehumbert 1995; McKim et al. 2021), and smallest in the inner tropics, where the surface's emission is blocked by the H<sub>2</sub>O continuum. The atmospheric feedbacks from the CO<sub>2</sub> and H<sub>2</sub>O bands play a supporting role to  $\lambda_{\text{surf}}$  at mid and high latitudes, but they rival the surface feedback in the inner tropics, with the global pattern of  $\lambda_{\text{atm}}$  largely determined by the pattern of the atmospheric lapse rate change  $d\gamma_{\text{lr}}/dT_s$ . The H<sub>2</sub>O continuum provides a negligible feedback

below  $\sim 310$  K (see Section 5), but the continuum itself is still important through its influence on  $\lambda_{\text{surf}}$ .

This spectral picture is arguably a more intuitive starting point for reasoning about different climates than the conventional decomposition of  $\lambda_{LW}$  into Planck, Lapse Rate and Water Vapor feedbacks. As discussed by Cronin and Dutta (in revision at QJRMS), it is non-trivial to accurately estimate the supposedly-simple Planck feedback from first principles. Similarly, one can qualitatively reason that Lapse Rate and Water Vapor feedbacks both increase in magnitude under global warming, but these are large and of opposite sign, so it is difficult to predict their net change and, by extension, the  $T_s$ -dependence of  $\lambda_{LW}$ , in the conventional decomposition without resorting to numerical models. The strong cancellations between Planck, Lapse Rate and Water Vapor feedbacks can be alleviated by considering conventional feedbacks in a fixed relative humidity framework (Ingram 2010; Held and Shell 2012), but this comes at the cost that the state-dependence of the Planck feedback is no longer trivial to understand at fixed RH.

In contrast, the state-dependence of  $\lambda_{LW}$  is fairly straightforward to understand from a spectral perspective, at least in broad brushstrokes. For present-day Earth the  $T_s$ -dependence of  $\lambda_{LW}$  is dominated by the surface in most regions. If relative humidity is fixed,  $\lambda_{\text{surf}}$  increases at very cold temperatures, peaks around 260 – 290 K depending on RH, and then decreases again (see Section 5). The decrease is rapid at high RH due to the H<sub>2</sub>O continuum, but much slower at low RH. Atmospheric feedbacks also have state-dependence. All of them increase in magnitude as the atmosphere warms, and are further amplified by a weakening lapse rate. In the tropics the state-dependence of  $\lambda_{LW}$  is thus set by the interplay between a decreasing surface feedback and increasing atmospheric feedbacks. This can lead to surprising dynamics – at high RH,  $\lambda_{\text{surf}}$  decreases in magnitude more rapidly with warming than the atmospheric feedbacks from  $\lambda_{\text{CO}_2}$  and  $\lambda_{\text{H}_2\text{O}}$  increase. As a result  $\lambda_{LW}$  becomes non-monotonic with warming and develops a local minimum around  $\sim 310$  K, which leads to a local maximum in climate sensitivity (Seeley and Jeevanjee 2021).

The state-dependence of  $\lambda_{LW}$  at temperatures far above  $\sim 310$  K is beyond the scope of this paper, but a spectral perspective points to the importance of stabilizing H<sub>2</sub>O and CO<sub>2</sub> bands versus the destabilizing H<sub>2</sub>O continuum as Earth approaches the runaway greenhouse. The main caveat here is that Earth's net feedback does not necessarily stay dominated by  $\lambda_{LW}$  at very high surface

temperatures, and atmospheric feedbacks are also complicated at high temperatures by effects such as non-dilute thermodynamics and surface pressure changes (Goldblatt et al. 2013; Ramirez et al. 2014).

There are several remaining shortcomings in our analysis of  $\lambda_{LW}$  that are beyond the scope of this paper. A major one is our assumption that the atmosphere can be described by a single bulk lapse rate, such that temperature has to monotonically decrease with altitude. In the real world inversions are common, particularly in polar regions and over subtropical oceans. Comparable to the long-standing discussion about how to interpret the Lapse Rate feedback at high latitudes in the conventional decomposition (e.g., Cai and Lu 2009; Payne et al. 2015; Stuecker et al. 2018; Boeke et al. 2021; Henry et al. 2021), we therefore expect that our approach here only provides a first step towards understanding the processes which shape  $\lambda_{LW}$  in inversion regions.

Another assumption is that we ignore stratospheric changes, even though stratospheric cooling induced by rising CO<sub>2</sub> levels is a major and robust signal of anthropogenic warming (e.g., Vallis et al. 2014). It is notable that the radiative changes due to stratospheric cooling are also hard to intuitively explain using conventional feedbacks. Climate model analyses typically treat the stratosphere's fast radiative adjustment to CO<sub>2</sub> changes as distinct from Planck, Lapse Rate, and Water Vapor feedbacks. Our derivations here sidestep this issue and treat  $T_{\text{strat}}$  as a fixed parameter. Similarly, our derivations ignore the potential feedback from relative humidity changes. In reality there is no guarantee that relative humidity will remain constant under global warming, let alone would have been similar in past climates. In principle our analysis starting from the emission level approximation can be extended to estimate the feedbacks associated with changes in either RH or  $T_{\text{strat}}$ ; RH changes would lead to a feedback term proportional to  $\partial T_{\text{rad}}/\partial \text{RH}$ , while stratospheric changes would lead to a feedback term proportional to  $\partial T_{\text{rad}}/\partial T_{\text{strat}}$ .

*Acknowledgments.* D.D.B.K. thanks Jeevanjee Gardens in Nairobi. N.J.L. was supported by the NOAA Climate Program Office's Modeling, Analysis, Predictions, and Projections program through grant NA20OAR4310387.

*Data availability statement.* HadGEM2 GCM data is publicly available in CMIP data archives. The HadGEM2 radiative kernel is available at <https://archive.researchdata.leeds.ac.uk/382>. Scripts to compute analytic feedbacks will be posted online once the manuscript is accepted for publication.

## APPENDIX A

### CO<sub>2</sub> Forcing

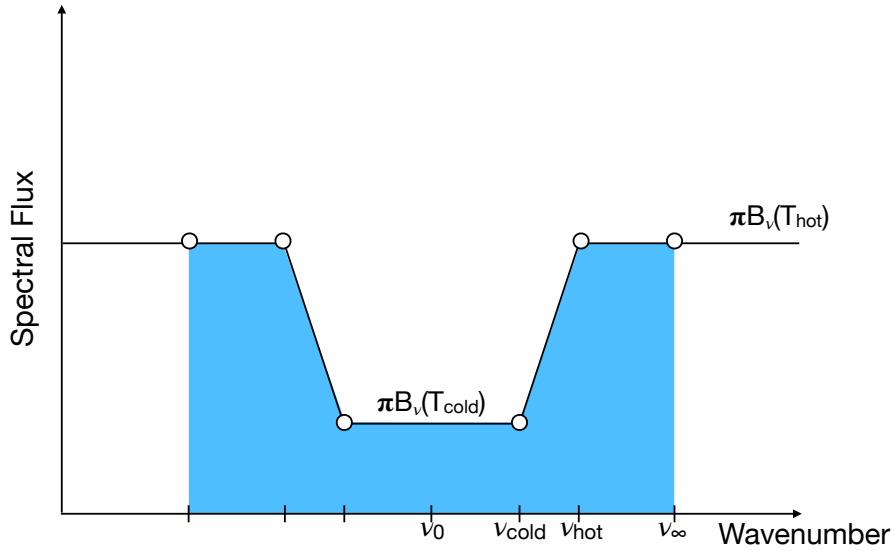


FIG. A1. CO<sub>2</sub> ditch model for the CO<sub>2</sub> forcing. The shaded blue area is the OLR contribution from the CO<sub>2</sub> band as well as neighboring spectral regions. The band edges  $\nu_{\text{hot}}$  and  $\nu_{\text{cold}}$  vary in response to CO<sub>2</sub> concentration  $q_{\text{CO}_2}$ , while  $\nu_{\infty}$  is sufficiently far away from the CO<sub>2</sub> band to be constant with respect to  $q_{\text{CO}_2}$ .

The CO<sub>2</sub> ditch model can be used to explain the CO<sub>2</sub> forcing in addition to the CO<sub>2</sub> band feedback. This section rederives the CO<sub>2</sub> forcing expressions from Wilson and Gea-Banacloche (2012) and Jeevanjee et al. (2021b), which are valid as long as the CO<sub>2</sub> band center radiates from the stratosphere. Note that our CO<sub>2</sub> band feedback model only considers OLR changes inside the CO<sub>2</sub> band (see Figure 6). This is because the effect of CO<sub>2</sub> on  $\lambda_{\text{H}_2\text{O}}$  or  $\lambda_{\text{surf}}$  is separately considered in the derivation of those feedbacks. Forcing is defined as the OLR change integrated across all wavenumbers, however, so here we need to consider the expanded shaded region shown in Figure A1. The OLR integrated across this expanded region, OLR<sub>+</sub>, is

$$\begin{aligned}
 \text{OLR}_+ &= 2 \int_{\nu_0}^{\nu_{\infty}} \pi B_{\nu_0}(T_{\text{rad}}) d\nu \\
 &= [\pi B_{\nu_0}(T_{\text{hot}}) + \pi B_{\nu_0}(T_{\text{cold}})] (\nu_{\text{hot}} - \nu_{\text{cold}}) + 2\pi B_{\nu_0}(T_{\text{cold}}) (\nu_{\text{cold}} - \nu_0) + \\
 &\quad 2\pi B_{\nu_0}(T_{\text{hot}}) (\nu_{\infty} - \nu_{\text{hot}}).
 \end{aligned} \tag{A1}$$

The forcing from a doubling of CO<sub>2</sub> is then

$$\begin{aligned}
F_{\text{CO}_2}^{2x} &= -\frac{d\text{OLR}_+}{d\log_2(q_{\text{CO}_2})} \\
&= -\ln(2)\frac{d\text{OLR}_+}{d\ln q_{\text{CO}_2}} \\
&= -\ln(2)\left(\left[\pi B_{\nu_0}(T_{\text{hot}}) + \pi B_{\nu_0}(T_{\text{cold}})\right]\left(\frac{d\nu_{\text{hot}}}{d\ln q_{\text{CO}_2}} - \frac{d\nu_{\text{cold}}}{d\ln q_{\text{CO}_2}}\right) + 2\pi B_{\nu_0}(T_{\text{cold}})\frac{d\nu_{\text{cold}}}{d\ln q_{\text{CO}_2}} - \right. \\
&\quad \left. 2\pi B_{\nu_0}(T_{\text{hot}})\frac{d\nu_{\text{hot}}}{d\ln q_{\text{CO}_2}}\right) \tag{A2}
\end{aligned}$$

The minus sign in the first line ensures that forcing is positive when OLR decreases, while the base-2 logarithm is necessary because forcing is defined with respect to a CO<sub>2</sub> doubling. In the second step we then change the logarithm's base to the natural logarithm, while in the third step we treat the emission temperatures  $T_{\text{hot}}$  and  $T_{\text{cold}}$  as constant. This is valid because the derivative of OLR with respect to  $q_{\text{CO}_2}$  is taken at fixed  $T_s$  (i.e., at fixed surface temperature, the temperature outside the CO<sub>2</sub> band and in the stratosphere are both independent of CO<sub>2</sub> concentration).

The CO<sub>2</sub> band edges are defined by  $T_{\text{CO}_2}(\nu_{\text{hot}}) = T_{\text{hot}}$  and  $T_{\text{CO}_2}(\nu_{\text{cold}}) = T_{\text{strat}}$ . Solving for  $\nu_{\text{hot}}$  and  $\nu_{\text{cold}}$  we find

$$\nu_{\text{hot}} = \nu_0 + l_\nu \log \left[ q_{\text{CO}_2} \tau_{\text{CO}_2}^*(\nu_0) \left( \frac{T_{\text{hot}}}{T_s} \right)^{2/\gamma_{\text{lr}}} \right] \tag{A3}$$

$$\nu_{\text{cold}} = \nu_0 + l_\nu \log \left[ q_{\text{CO}_2} \tau_{\text{CO}_2}^*(\nu_0) \left( \frac{T_{\text{strat}}}{T_s} \right)^{2/\gamma_{\text{lr}}} \right]. \tag{A4}$$

We can see that the CO<sub>2</sub> band edges shift equally in response to a CO<sub>2</sub> increase:

$$\frac{d\nu_{\text{hot}}}{d\ln q_{\text{CO}_2}} = \frac{d\nu_{\text{cold}}}{d\ln q_{\text{CO}_2}} = l_\nu. \tag{A5}$$

It follows that the first term proportional to  $d\nu_{\text{hot}}/d\ln q_{\text{CO}_2} - d\nu_{\text{cold}}/d\ln q_{\text{CO}_2}$  in Equation A2 is zero.

The CO<sub>2</sub> forcing is thus

$$F_{\text{CO}_2}^{2x} = 2\ln(2)l_\nu (\pi B_{\nu_0}(T_{\text{hot}}) - \pi B_{\nu_0}(T_{\text{cold}})), \tag{A6}$$



which is identical to the analytic CO<sub>2</sub> forcing model in Jeevanjee et al. (2021b) (their Equations 7 and 14).

## APPENDIX B

### Transition from stratospheric to tropospheric CO<sub>2</sub> radiator fin

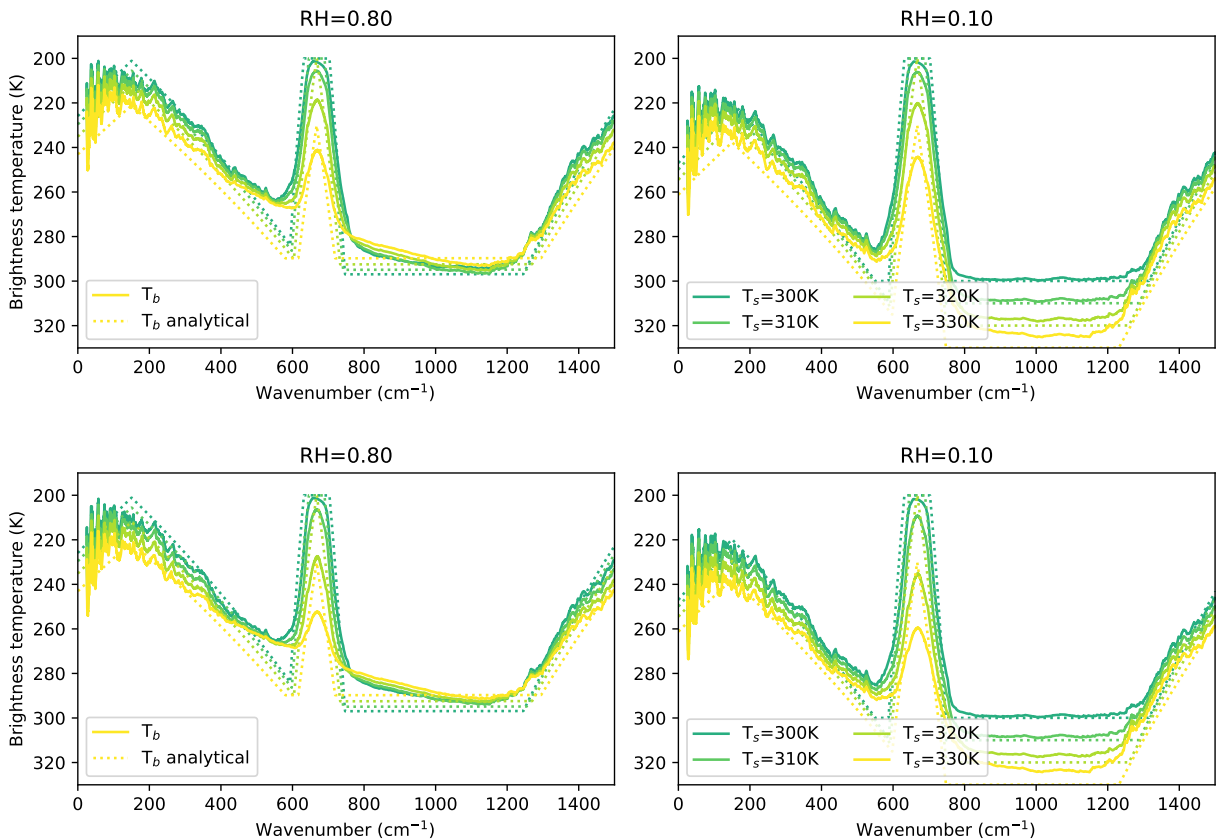


FIG. B1. Brightness temperatures computed from line-by-line calculations and smoothed with a 50 cm<sup>-1</sup> median filter (solid), versus analytic emission temperatures (dashed). Top row: calculations use a bulk lapse-rate profile,  $T(p) = T_s(p/p_s)^{\gamma_r}$ . Bottom row: calculations use a moist adiabat.

At high surface temperatures the CO<sub>2</sub> band center transitions from mainly radiating from the stratosphere to mainly radiating from the troposphere. Figure B1 shows smoothed brightness temperatures  $T_b$  computed from the 1D line-by-line calculations described in Section 5, with a CO<sub>2</sub> volume-mixing ratio of 400 ppm. In the middle of the CO<sub>2</sub> band, at about 667 cm<sup>-1</sup>, CO<sub>2</sub> radiates from the troposphere at surface temperatures above ~ 310 K. In rough agreement with

the line-by-line results, our analytic CO<sub>2</sub> brightness temperatures predict this transition happens at a surface temperature of  $\sim 320$  K (dashed lines in Fig. B1). In practice we therefore use a transition temperature of  $T_{s,0} = 310$  K for 400 ppm of CO<sub>2</sub> to determine when CO<sub>2</sub> changes from a stratospheric to a tropospheric radiator.

## APPENDIX C

### Spatial correlations in analytic feedback maps

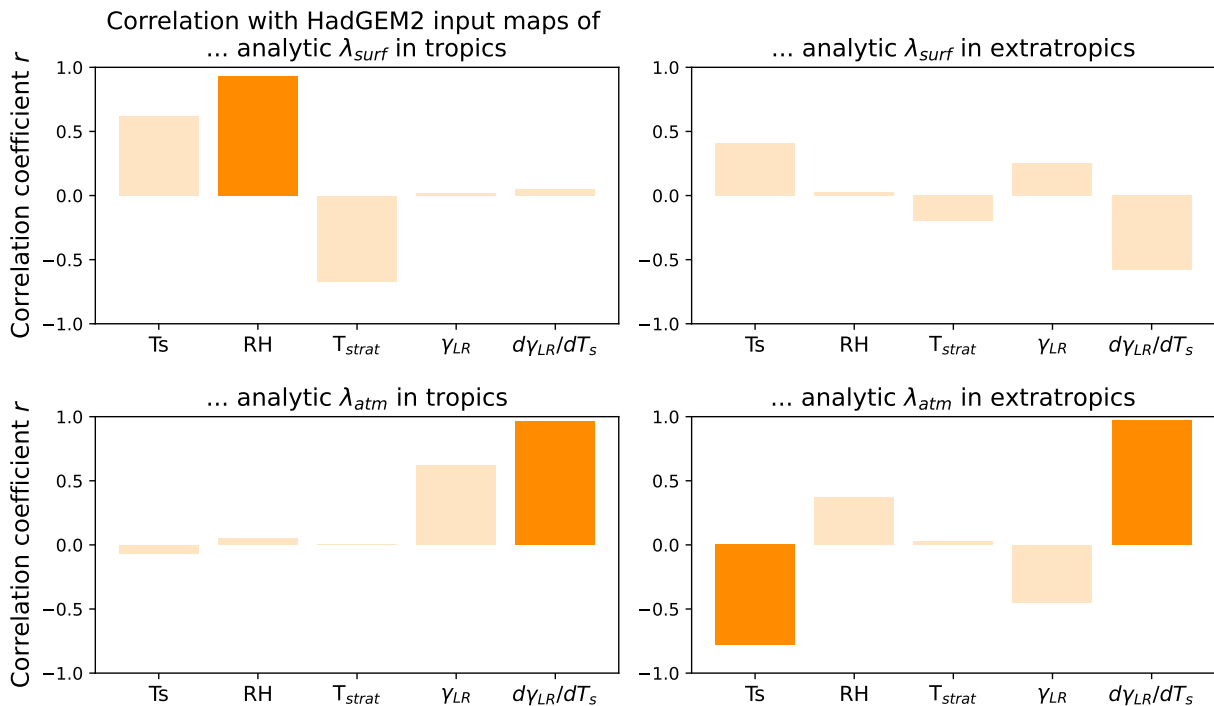


FIG. C1. Spatial correlation between the analytic feedback maps of  $\lambda_{surf}$  and  $\lambda_{atm}$  (Figure 10, right column), and the inputs to our analytic model (Figure 9). Top row shows correlations between inputs and  $\lambda_{surf}$ , bottom row shows correlations between inputs and  $\lambda_{atm}$ . Left column shows correlations inside the tropics, right column shows correlations in the extratropics. Dark colors highlight particularly strong correlations ( $|r| \geq 0.8$ ).

Figure C1 repeats the same analysis as in Figure 12, but using the analytic feedback maps of  $\lambda_{surf}$  and  $\lambda_{atm}$ . Given that the analytic model is computed using the input fields from Figure 9, it is not surprising that most correlations between inputs and feedback maps are even higher than in Fig. 12. With the exception of  $\lambda_{atm}$  in the tropics, for which the correlation between the analytic

$\lambda_{atm}$  and  $\gamma_{lr}$  is slightly lower than between kernel-derived  $\lambda_{atm}$  and  $\gamma_{lr}$ , Figure C1 identifies the same strong correlations as Figure 12.

## References

- Andrews, T., J. M. Gregory, and M. J. Webb, 2015: The Dependence of Radiative Forcing and Feedback on Evolving Patterns of Surface Temperature Change in Climate Models. *Journal of Climate*, **28** (4), 1630–1648, <https://doi.org/10.1175/JCLI-D-14-00545.1>.
- Andrews, T., J. M. Gregory, M. J. Webb, and K. E. Taylor, 2012: Forcing, feedbacks and climate sensitivity in CMIP5 coupled atmosphere-ocean climate models. *Geophysical Research Letters*, **39** (9), <https://doi.org/10.1029/2012GL051607>.
- Andrews, T., and Coauthors, 2018: Accounting for Changing Temperature Patterns Increases Historical Estimates of Climate Sensitivity. *Geophysical Research Letters*, **45** (16), 8490–8499, <https://doi.org/10.1029/2018GL078887>.
- Armour, K. C., C. M. Bitz, and G. H. Roe, 2013: Time-Varying Climate Sensitivity from Regional Feedbacks. *Journal of Climate*, **26** (13), 4518–4534, <https://doi.org/10.1175/JCLI-D-12-00544.1>.
- Bloch-Johnson, J., R. T. Pierrehumbert, and D. S. Abbot, 2015: Feedback temperature dependence determines the risk of high warming. *Geophysical Research Letters*, **42** (12), 2015GL064240, <https://doi.org/10.1002/2015GL064240>.
- Bloch-Johnson, J., M. Rugenstein, and D. S. Abbot, 2020: Spatial radiative feedbacks from internal variability using multiple regression. *Journal of Climate*, <https://doi.org/10.1175/JCLI-D-19-0396.1>.
- Boeke, R. C., P. C. Taylor, and S. A. Sejas, 2021: On the Nature of the Arctic's Positive Lapse-Rate Feedback. *Geophysical Research Letters*, **48** (1), e2020GL091109, <https://doi.org/10.1029/2020GL091109>.
- Bretherton, C. S., P. N. Blossey, and M. Khairoutdinov, 2005: An Energy-Balance Analysis of Deep Convective Self-Aggregation above Uniform SST. *Journal of the Atmospheric Sciences*, **62** (12), 4273–4292, <https://doi.org/10.1175/JAS3614.1>.

- Budyko, M. I., 1969: The effect of solar radiation variations on the climate of the Earth. *Tellus*, **21 (5)**, 611–619, <https://doi.org/10.1111/j.2153-3490.1969.tb00466.x>.
- Byrne, M. P., and P. A. O’Gorman, 2013: Land–Ocean Warming Contrast over a Wide Range of Climates: Convective Quasi-Equilibrium Theory and Idealized Simulations. *Journal of Climate*, **26 (12)**, 4000–4016, <https://doi.org/10.1175/JCLI-D-12-00262.1>.
- Cai, M., and J. Lu, 2009: A new framework for isolating individual feedback processes in coupled general circulation climate models. Part II: Method demonstrations and comparisons. *Climate Dynamics*, **32 (6)**, 887–900, <https://doi.org/10.1007/s00382-008-0424-4>.
- Chung, E.-S., D. Yeomans, and B. J. Soden, 2010: An assessment of climate feedback processes using satellite observations of clear-sky OLR. *Geophysical Research Letters*, **37 (2)**, <https://doi.org/10.1029/2009GL041889>.
- Crisp, D., S. B. Fels, and M. D. Schwarzkopf, 1986: Approximate methods for finding CO<sub>2</sub> 15-*Mm* band transmission in planetary atmospheres. *Journal of Geophysical Research: Atmospheres*, **91 (D11)**, 11 851–11 866, <https://doi.org/10.1029/JD091iD11p11851>.
- Cronin, T. W., and M. F. Jansen, 2016: Analytic radiative–advective equilibrium as a model for high-latitude climate. *Geophysical Research Letters*, **43 (1)**, 2015GL067 172, <https://doi.org/10.1002/2015GL067172>.
- Ding, F., and R. T. Pierrehumbert, 2016: Convection in Condensable-rich Atmospheres. *The Astrophysical Journal*, **822 (1)**, 24, <https://doi.org/10.3847/0004-637X/822/1/24>.
- Dufresne, J.-L., V. Eymet, C. Crevoisier, and J.-Y. Grandpeix, 2020: Greenhouse Effect: The Relative Contributions of Emission Height and Total Absorption. *Journal of Climate*, **33 (9)**, 3827–3844, <https://doi.org/10.1175/JCLI-D-19-0193.1>.
- Elsasser, W. M., 1942: *Heat Transfer by Infrared Radiation in the Atmosphere*. Harvard university, Blue Hill meteorological observatory, Milton, Mass.
- Feldl, N., and G. H. Roe, 2013: Four perspectives on climate feedbacks. *Geophysical Research Letters*, **40 (15)**, 4007–4011, <https://doi.org/10.1002/grl.50711>.

- Feng, J., and Y. Huang, 2019: Diffusivity-Factor Approximation for Spectral Outgoing Longwave Radiation. *Journal of the Atmospheric Sciences*, **76** (7), 2171–2180, <https://doi.org/10.1175/JAS-D-18-0246.1>.
- Feng, J., D. Paynter, and R. Menzel, 2022: How a stable greenhouse effect on Earth is maintained under global warming. Earth and Space Science Open Archive, <https://doi.org/10.1002/essoar.10512049.1>.
- Fraser, P. J., G. I. Pearman, and P. Hyson, 1983: The global distribution of atmospheric carbon dioxide: 2. A review of provisional background observations, 1978–1980. *Journal of Geophysical Research: Oceans*, **88** (C6), 3591–3598, <https://doi.org/10.1029/JC088iC06p03591>.
- Goldblatt, C., T. D. Robinson, K. J. Zahnle, and D. Crisp, 2013: Low simulated radiation limit for runaway greenhouse climates. *Nature Geoscience*, **6** (8), 661–667, <https://doi.org/10.1038/ngeo1892>.
- Gordon, I. E., and Coauthors, 2017: The HITRAN2016 molecular spectroscopic database. *Journal of Quantitative Spectroscopy and Radiative Transfer*, **203**, 3–69, <https://doi.org/10.1016/j.jqsrt.2017.06.038>.
- Hartmann, D. L., and K. Larson, 2002: An important constraint on tropical cloud - climate feedback. *Geophysical Research Letters*, **29** (20), 12–1–12–4, <https://doi.org/10.1029/2002GL015835>.
- Held, I. M., and K. M. Shell, 2012: Using Relative Humidity as a State Variable in Climate Feedback Analysis. *Journal of Climate*, **25** (8), 2578–2582, <https://doi.org/10.1175/JCLI-D-11-00721.1>.
- Henry, M., T. M. Merlis, N. J. Lutsko, and B. E. J. Rose, 2021: Decomposing the Drivers of Polar Amplification with a Single-Column Model. *Journal of Climate*, **34** (6), 2355–2365, <https://doi.org/10.1175/JCLI-D-20-0178.1>.
- Huang, J., 2018: A Simple Accurate Formula for Calculating Saturation Vapor Pressure of Water and Ice. *Journal of Applied Meteorology and Climatology*, **57** (6), 1265–1272, <https://doi.org/10.1175/JAMC-D-17-0334.1>.
- Huang, X., X. Chen, B. J. Soden, and X. Liu, 2014: The spectral dimension of longwave feedback in the CMIP3 and CMIP5 experiments. *Geophysical Research Letters*, **41** (22), 7830–7837, <https://doi.org/10.1002/2014GL061938>.

- Huang, Y., and M. Bani Shahabadi, 2014: Why logarithmic? A note on the dependence of radiative forcing on gas concentration. *Journal of Geophysical Research: Atmospheres*, **119** (24), 2014JD022466, <https://doi.org/10.1002/2014JD022466>.
- Huang, Y., S. Leroy, P. J. Gero, J. Dykema, and J. Anderson, 2010: Separation of longwave climate feedbacks from spectral observations. *Journal of Geophysical Research: Atmospheres*, **115** (D7), <https://doi.org/10.1029/2009JD012766>.
- Ingram, W., 2010: A very simple model for the water vapour feedback on climate change. *Quarterly Journal of the Royal Meteorological Society*, **136** (646), 30–40, <https://doi.org/10.1002/qj.546>.
- Jeevanjee, N., and S. Fueglistaler, 2020: Simple Spectral Models for Atmospheric Radiative Cooling. *Journal of the Atmospheric Sciences*, **77** (2), 479–497, <https://doi.org/10.1175/JAS-D-18-0347.1>.
- Jeevanjee, N., D. D. B. Koll, and N. Lutsko, 2021a: “Simpson’s Law” and the Spectral Cancellation of Climate Feedbacks. *Geophysical Research Letters*, **48** (14), e2021GL093699, <https://doi.org/10.1029/2021GL093699>.
- Jeevanjee, N., J. T. Seeley, D. Paynter, and S. Fueglistaler, 2021b: An Analytical Model for Spatially Varying Clear-Sky CO<sub>2</sub> Forcing. *Journal of Climate*, **34** (23), 9463–9480, <https://doi.org/10.1175/JCLI-D-19-0756.1>.
- Kluft, L., S. Dacie, M. Brath, S. A. Buehler, and B. Stevens, 2021: Temperature-Dependence of the Clear-Sky Feedback in Radiative-Convective Equilibrium. *Geophysical Research Letters*, **48** (22), e2021GL094649, <https://doi.org/10.1029/2021GL094649>.
- Kluft, L., S. Dacie, S. A. Buehler, H. Schmidt, and B. Stevens, 2019: Re-Examining the First Climate Models: Climate Sensitivity of a Modern Radiative–Convective Equilibrium Model. *Journal of Climate*, **32** (23), 8111–8125, <https://doi.org/10.1175/JCLI-D-18-0774.1>.
- Koll, D. D. B., and T. W. Cronin, 2018: Earth’s outgoing longwave radiation linear due to H<sub>2</sub>O greenhouse effect. *Proceedings of the National Academy of Sciences*, **115** (41), 10293–10298, <https://doi.org/10.1073/pnas.1809868115>, <https://www.pnas.org/content/115/41/10293.full.pdf>.

- Koll, D. D. B., and T. W. Cronin, 2019: Hot Hydrogen Climates Near the Inner Edge of the Habitable Zone. *The Astrophysical Journal*, **881** (2), 120, <https://doi.org/10.3847/1538-4357/ab30c4>, 1907.13169.
- Li, J., 2000: Gaussian Quadrature and Its Application to Infrared Radiation. *Journal of the Atmospheric Sciences*, **57** (5), 753–765, [https://doi.org/10.1175/1520-0469\(2000\)057<0753:GQAIAT>2.0.CO;2](https://doi.org/10.1175/1520-0469(2000)057<0753:GQAIAT>2.0.CO;2).
- Manabe, S., and R. T. Wetherald, 1967: Thermal Equilibrium of the Atmosphere with a Given Distribution of Relative Humidity. *Journal of the Atmospheric Sciences*, **24**, 241–259, [https://doi.org/10.1175/1520-0469\(1967\)024<0241:TEOTAW>2.0.CO;2](https://doi.org/10.1175/1520-0469(1967)024<0241:TEOTAW>2.0.CO;2).
- McKim, B. A., N. Jeevanjee, and G. K. Vallis, 2021: Joint Dependence of Longwave Feedback on Surface Temperature and Relative Humidity. *Geophysical Research Letters*, **48** (18), e2021GL094074, <https://doi.org/10.1029/2021GL094074>.
- Meraner, K., T. Mauritsen, and A. Voigt, 2013: Robust increase in equilibrium climate sensitivity under global warming. *Geophysical Research Letters*, **40** (22), 5944–5948, <https://doi.org/10.1002/2013GL058118>.
- Mlawer, E. J., V. H. Payne, J.-L. Moncet, J. S. Delamere, M. J. Alvarado, and D. C. Tobin, 2012: Development and recent evaluation of the MT\_CKD model of continuum absorption. *Phil. Trans. R. Soc. A*, **370** (1968), 2520–2556, <https://doi.org/10.1098/rsta.2011.0295>.
- Pan, F., and X. Huang, 2018: The Spectral Dimension of Modeled Relative Humidity Feedbacks in the CMIP5 Experiments. *Journal of Climate*, **31** (24), 10 021–10 038, <https://doi.org/10.1175/JCLI-D-17-0491.1>.
- Payne, A. E., M. F. Jansen, and T. W. Cronin, 2015: Conceptual model analysis of the influence of temperature feedbacks on polar amplification. *Geophysical Research Letters*, **42** (21), 2015GL065 889, <https://doi.org/10.1002/2015GL065889>.
- Pierrehumbert, R., 1995: Thermostats, radiator fins and the local runaway greenhouse. *Journal of the Atmospheric Sciences*, **52**, 1784–1806.
- Pierrehumbert, R. T., 2010: *Principles of Planetary Climate*. Cambridge University Press, Cambridge, UK.

- Raghuraman, S. P., D. Paynter, and V. Ramaswamy, 2019: Quantifying the Drivers of the Clear Sky Greenhouse Effect, 2000–2016. *Journal of Geophysical Research: Atmospheres*, **n/a (n/a)**, <https://doi.org/10.1029/2019JD031017>.
- Ramirez, R. M., R. K. Kopparapu, V. Lindner, and J. F. Kasting, 2014: Can Increased Atmospheric CO<sub>2</sub> Levels Trigger a Runaway Greenhouse? *Astrobiology*, **14 (8)**, 714–731, <https://doi.org/10.1089/ast.2014.1153>.
- Romps, D. M., 2016: Clausius–Clapeyron Scaling of CAPE from Analytical Solutions to RCE. *Journal of the Atmospheric Sciences*, **73 (9)**, 3719–3737, <https://doi.org/10.1175/JAS-D-15-0327.1>.
- Romps, D. M., J. T. Seeley, and J. P. Edman, 2022: Why the forcing from carbon dioxide scales as the logarithm of its concentration. *Journal of Climate*, **35 (13)**, 4027–4047, <https://doi.org/10.1175/JCLI-D-21-0275.1>.
- Seeley, J. T., 2018: Convection, Radiation, and Climate: Fundamental Mechanisms and Impacts of a Changing Atmosphere. Ph.D. thesis, UC Berkeley.
- Seeley, J. T., and N. Jeevanjee, 2021: H<sub>2</sub>O Windows and CO<sub>2</sub> Radiator Fins: A Clear-Sky Explanation for the Peak in Equilibrium Climate Sensitivity. *Geophysical Research Letters*, **48 (4)**, e2020GL089609, <https://doi.org/10.1029/2020GL089609>.
- Seeley, J. T., N. Jeevanjee, W. Langhans, and D. M. Romps, 2019: Formation of Tropical Anvil Clouds by Slow Evaporation. *Geophysical Research Letters*, **46 (1)**, 492–501, <https://doi.org/10.1029/2018GL080747>.
- Sherwood, S., and Coauthors, 2020: An assessment of Earth’s climate sensitivity using multiple lines of evidence. *Reviews of Geophysics*, **n/a (n/a)**, e2019RG000678, <https://doi.org/10.1029/2019RG000678>.
- Simpson, G., 1928a: Some studies in terrestrial radiation. *Memoirs of the Royal Meteorological Society*, **2 (16)**, 69–95.
- Simpson, G. C., 1928b: Further studies in terrestrial radiation. *Memoirs of the Royal Meteorological Society*, **3 (21)**.



- Soden, B. J., I. M. Held, R. Colman, K. M. Shell, J. T. Kiehl, and C. A. Shields, 2008: Quantifying Climate Feedbacks Using Radiative Kernels. *Journal of Climate*, **21** (14), 3504–3520, <https://doi.org/10.1175/2007JCLI2110.1>.
- Stuecker, M. F., and Coauthors, 2018: Polar amplification dominated by local forcing and feedbacks. *Nature Climate Change*, **8** (12), 1076, <https://doi.org/10.1038/s41558-018-0339-y>.
- Tierney, J. E., J. Zhu, J. King, S. B. Malevich, G. J. Hakim, and C. J. Poulsen, 2020: Glacial cooling and climate sensitivity revisited. *Nature*, **584** (7822), 569–573, <https://doi.org/10.1038/s41586-020-2617-x>.
- Vallis, G. K., P. Zurita-Gotor, C. Cairns, and J. Kidston, 2014: Response of the large-scale structure of the atmosphere to global warming. *Quarterly Journal of the Royal Meteorological Society*, n/a–n/a, <https://doi.org/10.1002/qj.2456>.
- Wilson, D. J., and J. Gea-Banacloche, 2012: Simple model to estimate the contribution of atmospheric CO<sub>2</sub> to the Earth’s greenhouse effect. *American Journal of Physics*, **80** (4), 306–315, <https://doi.org/10.1119/1.3681188>.
- Zelinka, M. D., T. A. Myers, D. T. McCoy, S. Po-Chedley, P. M. Caldwell, P. Ceppi, S. A. Klein, and K. E. Taylor, 2020: Causes of Higher Climate Sensitivity in CMIP6 Models. *Geophysical Research Letters*, **47** (1), e2019GL085782, <https://doi.org/10.1029/2019GL085782>.
- Zhang, R., H. Wang, Q. Fu, and P. J. Rasch, 2020: Assessing Global and Local Radiative Feedbacks Based on AGCM Simulations for 1980–2014/2017. *Geophysical Research Letters*, **47** (12), e2020GL088063, <https://doi.org/10.1029/2020GL088063>.